

ANALYSIS OF AN OPTICAL COHERENCE
IMAGING MODALITY ON THE DETECTION OF AN
ABNORMALITY IN BIOLOGICAL TISSUE WITH A
NANOPARTICLE CONTRAST AGENT

by
Kit-Iu Cheong

A Dissertation Submitted to the Faculty of the
COLLEGE OF OPTICAL SCIENCES
In Partial Fulfillment of the Requirements
For the Degree of
DOCTOR OF PHILOSOPHY
In the Graduate College
THE UNIVERSITY OF ARIZONA

2007

THE UNIVERSITY OF ARIZONA
GRADUATE COLLEGE

As members of the Dissertation Committee, we certify that we have read the dissertation prepared by Kit-Iu Cheong

entitled Analysis of an Optical Coherence Imaging Modality on the Detection of an Abnormality in Biological Tissue with a Nanoparticle Contrast Agent

and recommend that it be accepted as fulfilling the dissertation requirement for the Degree of Doctor of Philosophy

_____ Date: 11/9/07
Eric Clarkson

_____ Date: 11/9/07
Arthur Gmitro

_____ Date: 11/9/07
Jannick Rolland

Final approval and acceptance of this dissertation is contingent upon the candidate's submission of the final copies of the dissertation to the Graduate College. I hereby certify that I have read this dissertation prepared under my direction and recommend that it be accepted as fulfilling the dissertation requirement.

_____ Date: 11/9/07
Dissertation Director: Eric Clarkson

STATEMENT BY AUTHOR

This dissertation has been submitted in partial fulfillment of requirements for an advanced degree at the University of Arizona and is deposited in the University Library to be made available to borrowers under rules of the Library.

Brief quotations from this dissertation are allowable without special permission, provided that accurate acknowledgment of source is made. Requests for permission for extended quotation from or reproduction of this manuscript in whole or in part may be granted by the head of the major department or the Dean of the Graduate College when in his or her judgment the proposed use of the material is in the interests of scholarship. In all other instances, however, permission must be obtained from the author.

Kit-Iu Cheong

ACKNOWLEDGEMENTS

I am grateful to my family, for their unconditional support.

I am grateful to Dr. Eric Clarkson and Dr. Jannick Rolland, for their help and kind words during this process. Thanks to Dr. Arthur Gmitro, for his advices in the dissertation writing. Thanks to Dr. Jennifer Barton and her OCT team at the University of Arizona, for the helpful discussions on the OCT data acquisition process. Also, thanks to Mohammed Salem, Kye Sung Lee, and Panomsak Meemon for stimulating and constructive discussions and information about OCT systems developed in the Optical Diagnostic and Applications Laboratory at University of Central Florida.

Finally, I am grateful to my friends and anyone whose path that I have crossed, for sharing the common human experiences and smiles.

*To my late husband,
Dana S. Clarke, Jr., a gentle soul and a kind spirit,
for his love and inspirations.*

TABLE OF CONTENTS

LIST OF FIGURES	9
ABSTRACT	11
CHAPTER 1. INTRODUCTION	13
CHAPTER 2. OBSERVER AND IMAGE QUALITY	18
2.1. Stochastic Decision theory	18
2.2. Binary Classification	20
2.2.1. True Positive Fraction (TPF) and False Positive Fraction (FPF)	22
2.2.2. ROC Curve	23
2.2.3. Performance of Classifiers	24
2.2.4. Likelihood Ratio and Quadratic Observer	29
CHAPTER 3. STOCHASTIC WAVES	34
3.1. Early Studies in Scattering	35
3.2. Stochastic Wave Propagation in Continuum	37
3.2.1. Weak Fluctuation Approximation	38
3.2.2. Born Approximation	39
3.3. Wave in Discrete Stochastic Media	41
3.3.1. Single Particle Analysis	42
3.3.2. Ensemble of Random Scatterers	45
3.4. Related Problems: Relation to Radiative Transport Theory	49
3.5. Some Other Interesting Topics	50
3.5.1. Scattering vs. Line-of-sight Propagation	50
3.5.2. Media of Multiscale Fluctuations–Hybrid Model	52
CHAPTER 4. OPTICAL COHERENCE TOMOGRAPHY	54
4.1. Introduction	54
4.1.1. Dynamic Focusing	56
4.2. Mathematical Modeling of an OCT System	58
4.2.1. Optical Coherence and Interference	58
4.2.2. Source, Reference, and Sample Fields in OCT	63
4.2.3. Heterodyne Detection and Optical Power	75
4.2.4. Data Acquisition	77

TABLE OF CONTENTS—*Continued*

CHAPTER 5. STATISTICAL ANALYSIS OF OCT DATA	87
5.1. Sources of Randomness in OCT	87
5.1.1. Phase Fluctuation of a Broadband Source	88
5.1.2. Scattering Noise	89
5.1.3. Photodetector Noise	91
5.2. Stochastic Object Model	94
5.2.1. Permittivity Field, Refractive Index, and Scattering Potential	95
5.2.2. Stochastic Model of the Permittivity Field	97
5.2.3. Scattering Cross Section and Attenuation Coefficient	103
5.3. Covariance Function of a Random Field Driven by Multiple Sources of Randomness	105
5.4. Covariance Function of OCT Data	107
CHAPTER 6. TISSUE OPTICS AND NANOPARTICLE AIDED OCT IMAGING	118
6.1. Optical Properties of Biological Tissues	118
6.1.1. Absorption	119
6.1.2. Scattering	120
6.1.3. Anisotropy and Reduced Scattering Coefficient	121
6.2. Optical Molecular Imaging and Contrast Agents	123
6.2.1. Contrast Agents for OCT	124
6.3. Detection of an Abnormality in Biological Tissue Using Contrast Agent	125
6.3.1. Detection Task: Statement of the Hypothesis	125
6.3.2. Scattering Potential Description of the Nanoparticle Contrast Agents	126
6.3.3. Covariance Function of the OCT Data for the Detection Task	128
6.4. Simulation	141
6.4.1. Summary of Equations	141
6.4.2. List of Parameters Used in the Simulation	145
6.4.3. Optical Properties of the Host Tissue and the Nanoparticle Contrast Agents	146
6.4.4. Imaging Area and Number of Data Point	148
6.5. Results and Discussion	149
CHAPTER 7. SUMMARY AND FUTURE WORK	156
7.1. Summary	156
7.2. Areas for Future Work	158
7.2.1. Mathematical Model for Biological Tissue	158
7.2.2. Stochastic Wave Propagation in Random Media	159
7.2.3. Information Content and Demodulation Schemes	160
7.2.4. Different OCT Configurations	161

TABLE OF CONTENTS—*Continued*

APPENDIX A. MEAN OF DEMODULATED OCT DATA	162
APPENDIX B. INTEGRAL IN THE Z-DIRECTION	164
APPENDIX C. INTEGRAL IN THE TRANSVERSE DIRECTION	166
REFERENCES	168

LIST OF FIGURES

FIGURE 2.1. Components of a decision problem. 19

FIGURE 2.2. Illustration for chain of events for image analysis based on statistical inference. 20

FIGURE 2.3. Partition of the decision space by a simple hypersurface in a binary classification task. 21

FIGURE 2.4. An ROC graph. 24

FIGURE 2.5. Probability distribution functions for the measurements under hypothesis H_0 and H_1 25

FIGURE 2.6. (a) A greater separation between the means of the two hypotheses. (b) A small spread results in less overlap between the two PDFs. . . 26

FIGURE 2.7. (a) The hit rate (TPF) corresponds to the area under the PDF $pr(V|H_1)$ to the right of the threshold, while the false alarm (FP) corresponds to the area under the PDF $pr(V|H_0)$ to the right of the threshold. (b) Changes in TPF and FPF in response to change in the threshold level. (c) Change of location of observer in the ROC graph. 27

FIGURE 2.8. Schematic illustration of the generic relationship between AUC and the index of detectability (d_a). 28

FIGURE 3.1. Geometry for a scattering problem. 42

FIGURE 3.2. Illustration of single scattering, first order multiple scattering, and multiple scattering. 46

FIGURE 3.3. Illustration of (a) scattering and (b) line-of-sight problems. . . . 51

FIGURE 4.1. Free space Optical Coherence Tomography modality with dynamic focusing. 55

FIGURE 4.2. Relationship between beam width and depth of focus (DOF). (a) Wider beam width, longer DOF. (b) Narrower beam width, shorter DOF. (c) In dynamic focusing, the location of the focal plane inside the sample is moving in accordance with the scanning depth, which is defined by the reference mirror. 57

FIGURE 4.3. (a) Interferogram of a coherent source. (b) Interferogram of a partially coherent source. The visibility of the fringes decays as the delay time increases, and vanishes when the delay time is larger than the source coherent time. 62

FIGURE 4.4. Illustration of \mathbf{r}_d and the reference plane for the mixing of the sample and reference beams. 67

LIST OF FIGURES—*Continued*

FIGURE 4.5. Illustration of the band-pass (shaded rectangles) and the low-pass filters. (a) The band-pass filter has its spectrums centered around f_m and $-f_m$. (b) The band-pass filter is shifted by an amount of $-f_m$. (c) The band-pass filter is shifted by an amount of f_m	82
FIGURE 4.6. Comparison between the scaling function of a Shannon wavelet (dashed line) and a Meyer wavelet (solid line). The ripples in the scaling function of the Meyer wavelet die out more quickly than that of the Shannon wavelet.	85
FIGURE 5.1. Illustration of shot noise. Photons arrive at a random time and are converted into photoelectrons randomly. The random current pulses cause fluctuations in the current output.	92
FIGURE 5.2. (a) The point particles distribute randomly but uniformly over the plane of area A. (b) There is a higher concentration of points within the central circle, but the location of the point particles are still random in a way that they are not laid out according to any pattern. If the width of the central circle varies, then the corresponding probability density function describing the spatial distribution of the particles is a random function.	99
FIGURE 6.1. Geometry of the incident and scattered directions.	121
FIGURE 6.2. Illustration of axial and transverse intervals.	148
FIGURE 6.3. Baseline study of detectability for abnormalities of different sizes. 151	
FIGURE 6.4. Detectability study for an abnormality with half-width of 0.01mm. 152	
FIGURE 6.5. Detectability study for an abnormality with half-width of 0.02mm. 153	
FIGURE 6.6. Detectability study of an abnormality with half-width of 0.04mm. 154	

ABSTRACT

There is great interest in promoting the use of contrast agents in optical imaging for better diagnosis of diseases. However, until recently, there was still no quantitative method existing to assess the ability of contrast agents in improving clinical diagnosis. In this study, we used the method of task-based medical image analysis as a quantitative tool to evaluate the effectiveness of nanoparticles as contrast agents in an OCT imaging modality for clinical diagnosis.

The task was formulated as the detection of abnormalities in a biological tissue using a quadratic observer. We derived the test statistics of the quadratic observer, and an analytical expression for the index of detectability for such a quadratic observer. The statistical properties of the OCT data are determined by the stochastic mechanisms in the imaging system as well as the demodulation method in the data acquisition process. In this analysis, we have considered the effect of phase fluctuations from the broadband source, the shot noise fluctuations of the imaging system, and the scattering noise due to refractive index fluctuation in the biological tissue. Our analysis was performed at the system level by integrating to the analysis the data demodulation process based on a mixer scheme. Also, we implemented the dynamic focusing in the scanning process.

Optical propagation in biological samples is dominated by scattering due to fluctuations in refractive index. For OCT imaging, it is assumed that only the singly scattered field from the sample will contribute significantly to the interferometric optical power. We modeled the normal biological tissue (the background) as a spatial Poisson field of randomly distributed scattering centers, and the abnormality (the target) as a region with a different concentration of scattering centers embedded in the background.

We presented the results on the detectability of abnormalities of different sizes,

with or without the presence of contrast agents. We have shown that the application of nanoparticle contrast agents improved the detectability of small abnormalities which are usually difficult to detect. We have thus shown the efficacy of the task-based analysis framework in delivering quantitative assessments of the efficiency of contrast agents.

Chapter 1

INTRODUCTION

In this study, we analyze the performance of an Optical Coherence Tomography (OCT) imaging modality in detecting abnormalities in biological tissue using nanoparticles as contrast agents. The purpose of this study is to provide a tool to quantitatively evaluate the advantage of using contrast agents in OCT imaging. Early applications of OCT were focused on obtaining morphological information of the biological sample. Then its application was extended to functional biological imaging based on detecting changes in optical properties of biological systems corresponding to physiological processes. For example, Lazebnik et al. [1] used an OCT system to detect neural activity through scattering changes. Recently, there is a new thrust to expand the imaging capability of OCT into molecular and cellular optical imaging by using contrast agents such as microspheres or nanoparticles [2]. Molecular optical imaging brings promises of early detection and treatment of diseases, and facilitating better delivery of pharmaceutical products to biological systems [2]. However, these promises are met with multiple challenges and limitations. For example, before any material can be clinically approved as a contrast agent, it is necessary to have a better understanding of the effects of the material on the biological systems under normal and pathological conditions, especially its toxicity. As one would expect, higher concentration of the contrast agent would generate stronger signals. Yet, what will be the optimal or reasonable concentration of the contrast agents so that a diagnostic conclusion can be made without jeopardizing patients with undue exposure to exogenous material? Therefore, it is important that quantitative studies are performed, using normal and diseased biological tissue models, to demonstrate the improvement provided by the use of contrast agents to clinical diagnostic ability.

For clinical diagnostic purposes, the performance of an imaging modality should not be evaluated solely on the aesthetic appearance of the images it produces, but rather, on its ability to convey the salient information of the object being imaged relevant to the tasks that the users (the physicians or researchers) have in mind [3]. Therefore, in this study, we will adopt the task-based image assessment approach developed from statistical decision theory. We will first give a brief overview of statistical decision theory and its application to medical image analysis in chapter 2. In statistical decision theory, an observer is used to analyze the input data, that are usually contaminated by noise, in order to determine the underlying truth state that generates the data. For a simple binary classification task, a graphical tool, the Receiver Operative Characteristic (ROC) graph, is often used to summarize the performance of the observer (or classifier). Different figures of merits, such as the index of detectability and the Area Under Curve (AUC) value, are developed to quantitatively evaluate observer performance. In §2.2.1, we will introduce the mathematical formulation of a quadratic observer, and an expression for the index of detectability of such a quadratic observer for a detection task will be presented.

OCT was developed in the early 90's. As an optical technique, it operates on the same principle as of the white-light interferometry: using interferograms of broadband light fields to study the properties of the samples. The predecessor of OCT is the one-dimensional optical ranging technique known as Optical Coherence-Domain Reflectometry (OCDR) developed in the eighties. OCDR uses a low coherence light source and interferometric detection techniques to obtain high sensitivity and high resolution range information, and is used to locate faults in fiber-optic cables and other network components [4]. Later on, the application of this ranging technique was expanded to eye imaging ([5] and [6]). In the early nineties, Huang et al. [7] combined the OCDR technique with tomographic imaging and developed the first OCT system.

Tomographic imaging is an important diagnostic tool in medical imaging. Optical

tomography is different from the X-ray and magnetic resonance techniques in a fundamental way. Most optical techniques are dominated by diffraction and, therefore, the Fourier slice theorem is not applicable. There are two major categories in optical tomography: Diffuse Optical Tomography (DOT) and Optical Diffraction Tomography (ODT). In DOT, multiply scattered photons diffused through the sample are collected, and different algorithms stemmed from back-projection methods, perturbation methods, and nonlinear optimization methods are used to derive tomographic images [8]. In ODT, singly scattered photons contribute to the image, and the Fourier diffraction projection theorem [9] is the principle on which the tomographic images are derived.

Light propagation in biological tissue is dominated by scattering due to fluctuations in the index of refraction of the tissue. Therefore, a study of OCT imaging of biological tissue will not be adequate without a description of stochastic wave properties, which will be covered in Chapter 3. Chapter 3 is not intended to be a comprehensive review on the topic of stochastic waves, but rather, a brief on the important concepts that are essential to the current analysis of OCT. When a light field propagates through a random medium, the deeper it propagates, the higher the probability that it is scattered multiple times. In order to minimize the effect of multiple scattering events to the measurement, a broadband source is used in OCT so that the coherence-gate established by the broadband source can serve as a safeguard against multiple scatterings. Thus the multiply scattered photons will not contribute significantly to the interferometric term, in which the information of the sample being studied by OCT can be extracted more easily, but will manifest as a disturbing background which deteriorates the system resolution, image contrast, and penetration depth [10].

With the coherence-gating effect, OCT is considered to belong to the ODT category since its signal consists mainly of the single scattered photons. Therefore, in this study, the sample field is modeled by using the first order multiple scattering ap-

proximation, which is described in Chapter 3. For an analysis of multiple scattering effects in OCT systems using extended Huygens-Fresnel theory, which was developed to study multiple scattering effects for beam propagation in the turbulent atmosphere by Yura [11], interested readers can consult the publications by Schmitt et al. [12] and Thrane et al. [13].

The other complication in imaging biological samples is that the scattering properties of the EM field vary widely depending on the sizes of the inhomogeneities. For example, structures with dimensions larger than the incident wavelengths tend to scatter in the forward direction, while smaller scale fluctuations (smaller than a wavelength) will scatter more isotropically (such Rayleigh scattering is described in §3.3.1). The complexity of biological tissues exhibit structures of different scales in a single sample. A complete description of the scattering effects stemming from different scales will be extremely involved, if it is possible. A two-scale approximation was developed as a manageable alternative to this problem ([14], [15], [16], [17], [18], [19], [20], [21], and [22]). This technique yields formulae that are convenient for numerical analysis and demonstrates a good agreement with experimental evidence and the results of other methods. A brief introduction to this model is given in §3.5.2 since we see it as a reasonable model for refining the current analysis in the future.

The basic optical aspect of OCT can be considered as simple as a free-space Michelson interferometer, though other varieties exist. The source field is split into a reference and a sample beam. As the sample beam passes through the biological tissue being imaged, the back-scattered or reflected field is collected and combined with the reference field, and an interferogram is formed. In Chapter 4, we will derive expressions of the optical power of the reference beam, sample beam, and the interferometric term in an OCT imaging modality based on such a simple Michelson interferometer configuration. We then give a brief discussion on the data acquisition process of OCT data, and derive an expression relating the demodulated OCT data to the detected optical power.

In order to study the performance of the OCT imaging modality in a detection task, the covariance property of the demodulated OCT data is needed for the quadratic observer to form a decision regarding the truth state underlying the biological tissue (whether an abnormality presents or not). In Chapter 5, we will focus on the discussion of the covariance property of the demodulated OCT data. We assume three major sources of randomness in the OCT imaging modality: (1) Fluctuations in the light field from the broadband source, (2) Fluctuations relating to the photo-detection process, and (3) Fluctuations due to scattering of light field by the random medium. To complete the discussion on scattering noise, we will introduce a stochastic model developed on the concept of spatial Poisson random field to describe the permittivity field, and thus the corresponding scattering potential, of the random medium.

In Chapter 6, we will use the statistical tools developed in the previous chapters to analyze the effect of nanoparticle contrast agents in the detection of abnormality in biological tissues using OCT imaging. The hypothesis being tested is described as: (1) Signal absent: no abnormality, and the contrast agents injected into the biological tissue distributed uniformly. (2) Signal present: abnormality exists. The contrast agents injected will have a denser concentration around the physical site of the abnormality in the tissue. We will describe how a numerical study is set up to evaluate the detectability index as well as the AUC value for this detection task using a quadratic observer. We will evaluate the detectability of an OCT system with different concentrations and different target specificity of the contrast agents, as well as different sizes for the abnormality.

Finally, we will conclude this dissertation by a discussion on the possible directions for future work in Chapter 7.

Chapter 2

OBSERVER AND IMAGE QUALITY

2.1 Stochastic Decision theory

Stochastic decision theory is the application of the techniques of statistical inference to random processes encountered in communication, radar, sonar, and other modern data processing systems. The two major types of decision are classification and estimation. In classification, the observer intends to infer the possible causes producing the resulting data. The observer usually has some information about the possible objects being imaged, the way in which objects are distorted by the mapping process, and the sources of randomness in the data. A radiologist trying to determine whether an image does or does not contain a tumor is an example of a classification task. The study of classification theory started in the mid-eighteenth century, pioneered by Thomas Bayes [23]. In estimation theory, the observer desires to infer the value of some parameter of interest from the observed data, for example, parameters of the probability law governing the mapping mechanism or other random processes involved. A radiologist trying to estimate the size of a tumor, given an image of the tumor, is an example of an estimation task. Early work in this area was led by Legendre [24] and Gauss [25] in the early nineteenth century. Research from Fisher [26], Neyman and Pearson [27] in the early twentieth century set the foundation of modern decision theory. Around 1940s, Kolmogoroff [28] and Wiener [29] applied statistical techniques to the solution of the optimum linear filtering problem. Since then the application of statistical techniques to the analysis of all types of systems has grown rapidly.

As shown in figure 2.1, a generic stochastic decision problem can be broken down into four components. The first component is the source of the observation. In

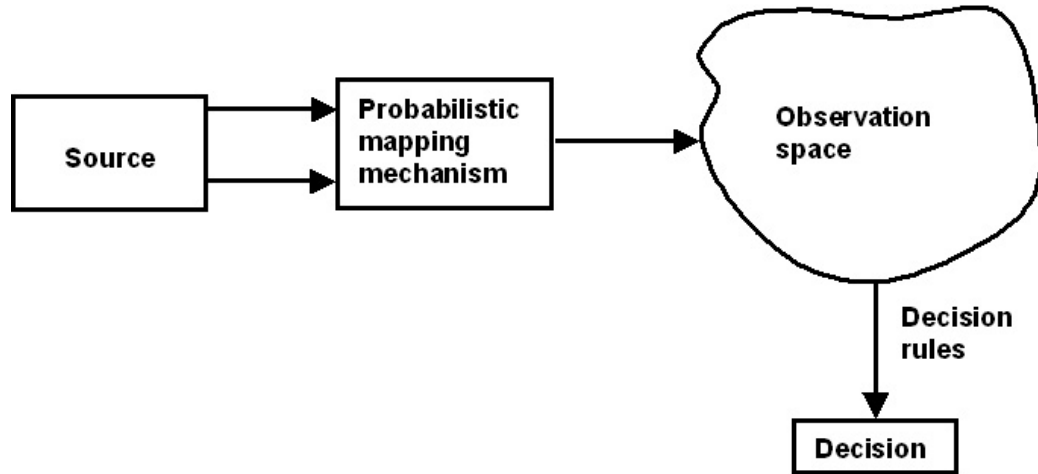


FIGURE 2.1. Components of a decision problem.

the simplest binary classification case, there are two choices for the source of the observation, which will be referred to as hypotheses H_0 and H_1 . More generally, the source of the observation can be one of the M hypotheses $H_0, H_1, H_2, \dots, H_{M-1}$. The second component in the decision theory framework is a probabilistic mapping mechanism which maps a hypothesis (represented as the source in figure 2.1) to points in the observation space according to the probability law governing the mapping. The third component is the observation space, which is an abstract mathematical space. It can be discrete or continuous, finite or infinite dimensional, depending on the nature of the mapping mechanism. The fourth component is a set of decision rules, which is the "brain" to the decision process. After observing the outcome in the observation space, the observer will make a decision regarding the hypotheses based on a set of decision rules.

Similarly, decision problems in medical or biological image diagnosis can be broken down into a chain of events as shown in figure 2.2. The object in figure 2.2 corresponds to the source in figure 2.1. In the scenario of cancer screening, for example, we have a simple binary decision task to determine which hypothesis (normal or diseased with cancer) is true regarding the person being diagnosed. The noisy imaging hardware

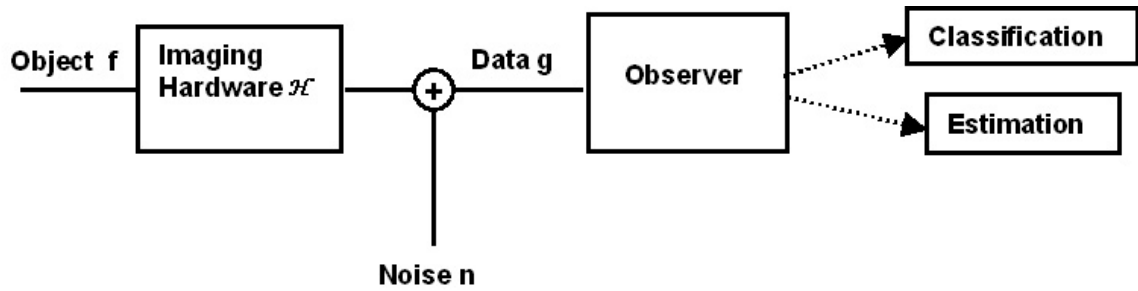


FIGURE 2.2. Illustration for chain of events for image analysis based on statistical inference.

corresponds to the probabilistic mapping mechanism. The data g resides in the observation space, which is the third component in figure 2.1. Finally, the observer is implemented with a set of decision rules (the fourth component in figure 2.1) developed for the task at hand.

2.2 Binary Classification

Two restrictions are imposed on the decision rules on which an observer draws its decision:

1. No randomness in the decision rule: Repeated observations of the same data should deliver the same decision.
2. Every observation will result in a decision.

With these two restrictions, classification is equivalent to partitioning the observation space into distinct (non-overlapping) regions, each of which will correspond to a certain underlying hypothesis. The combination of all these regions will contain all possible observation events.

Binary classification is the simplest task in which only two hypotheses about the sources are tested against each other. Usually, a test statistic (t) relating to the data

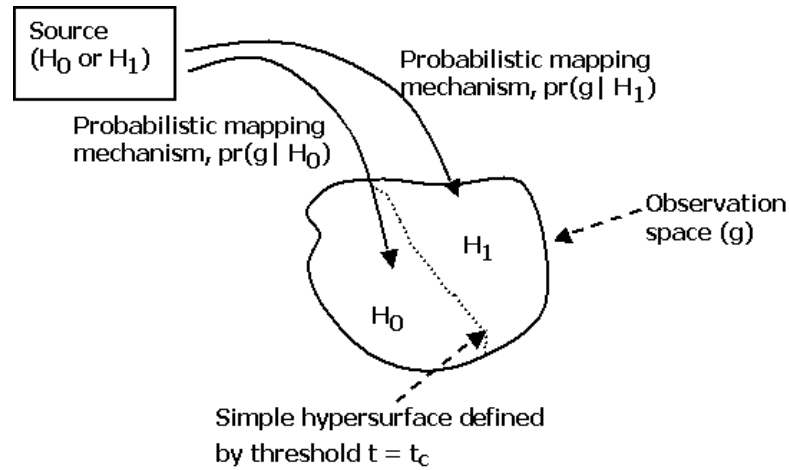


FIGURE 2.3. Partition of the decision space by a simple hypersurface in a binary classification task.

will be calculated through the discriminant function

$$T(g) = t, \quad (2.1)$$

which can be either a linear or nonlinear functional of the random data g . The observer chooses a decision threshold t_c as the criteria for its decision. For a particular observed data g , if the value of the corresponding test statistic calculated according to eq. (2.1) is greater than the threshold, then the observer will infer that the data g belongs to a particular class described by one of the two hypotheses being tested. At the same time, the observer assigns this given data point to the decision region in the observation space corresponding to the particular hypothesis. Therefore, the decision boundary is determined by the threshold chosen and the functional form of the discriminant function as

$$T(g) = t_c, \quad (2.2)$$

which maps a hypersurface in the observation space. For a binary classification problem, the observation space can be partitioned with a single such hypersurface as shown in figure 2.3.

2.2.1 True Positive Fraction (TPF) and False Positive Fraction (FPF)

In a binary classification problem, there are two underlying truth states regarding the source: the source belong to the class labeled as H_0 or H_1 . The observer, based on the observations (\mathbf{g}) and the decision rules adopted (the decision threshold and the discriminant function, see eq. (2.1)), will come to two possible decisions: D_0 or D_1 . The decision D_0 states that the observer infers that the observation presented is caused by a source belonging to the class H_0 , and similarly for D_1 . Since the observer does not have complete information about the underlying source, or information is lost during the mapping process, the decisions made by the observer will not be always correct. The possible scenarios of the decision outcome can be summarized as:

	H_1 : Signal present	H_0 : Signal absent
Decide D_1	True positive “Hit”	False positive “False alarm”
Decide D_0	False negative “Miss”	True negative “Correct rejection”

According to these possible outcomes in a binary classification problem, the following quantities can be defined to quantify an observer’s performance:

$$\begin{aligned}
 TPF &= \text{True Positive Fraction} \\
 &= \lim_{N \rightarrow \infty} \left[\frac{\text{Number of true positive decisions}}{\text{Number of actually positive cases}} \right], \tag{2.3}
 \end{aligned}$$

$$\begin{aligned}
 TNF &= \text{True Negative Fraction} \\
 &= \lim_{N \rightarrow \infty} \left[\frac{\text{Number of true negative decisions}}{\text{Number of actually negative cases}} \right], \tag{2.4}
 \end{aligned}$$

$$\begin{aligned}
 FPF &= \text{False Positive Fraction} \\
 &= 1 - TNF, \tag{2.5}
 \end{aligned}$$

and

$$\begin{aligned} FNF &= \text{False Negative Fraction} \\ &= 1 - TPF. \end{aligned} \tag{2.6}$$

In the medical literature, the TPF (True Positive Fraction) of an observer is also referred to as the sensitivity of the observer, which describes how sensitive an observer is with respect to the presence of the signal. The quantity TNF is commonly referred to as the specificity since it indicates the ability of the observer in correctly specifying the alternative hypothesis (H_0 , or signal absent). The performance of an observer can be fully quantified by the TPF (hit rate) and FPF (false alarm rate), and usually is presented via a graphical tool, the ROC (Receiver Operating Characteristic) curve as described in the next section.

2.2.2 ROC Curve

A receiver operating characteristic (ROC) graph is a technique for visualizing, organizing and selecting classifiers based on their performance. It was first used for radar signal analysis during World War II. In the 1950s, it was introduced into the psychophysics community for human detection of weak signals [30]. ROC analysis is used widely in medicine to evaluate the effectiveness of a new drug or diagnostic technique against the already established one ([31], [32], and [33]). ROC graphs are also used in machine learning to evaluate and compare algorithms [34].

In an ROC graph, the TPF (True Positive Fraction) is plotted against the FPF (False Positive Fraction) as shown in figure 2.4. It depicts the trade-off between true positives (hit rates or benefits) and false positives (false alarm rates or costs) of classifiers ([35] and [36]). The lower left corner (0, 0) represents an observer with a decision strategy of never issuing a positive call. Such a classifier commits no false alarm but also achieves no positive hit. The point (1, 1) at the upper right

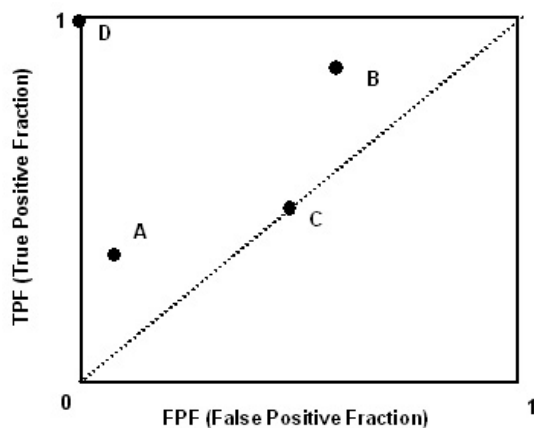


FIGURE 2.4. An ROC graph.

corner, represents an observer adopting the opposite decision strategy. The point D (0,1) in the figure corresponds to a perfect classifier. The performance of random classifiers that make their decision solely on guessing will fall along the diagonal line (for example, point C in figure 2.4) – the chance line. A classifier that makes its decision intelligently by employing information in the data will always appear in the upper triangular region above the chance line. A classifier appearing at the lower left part of the upper triangle may be thought of as "conservative". They make positive classifications only with strong evidence so the FPF is low. However, the TPF is low as well. On the other hand, classifiers on the upper right-hand side of the graph may be considered as "liberal". They make positive calls with weak evidence so they classify nearly all positives correctly, but high FPF also. For example, classifier A in figure 2.4 is more conservative than B.

2.2.3 Performance of Classifiers

In order to compare the effectiveness of an observer with respect to a certain task, figures of merits are developed to quantify the performance of observers. In the following sections, we will introduce two commonly used figure of merits and show

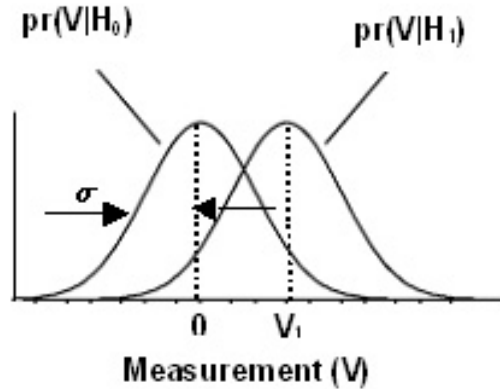


FIGURE 2.5. Probability distribution functions for the measurements under hypothesis H_0 and H_1 .

the relationship between them.

Index of Detectability

We will use a simple example of voltage measurement to illustrate the concept of a binary classification task and the index of detectability. In a simple voltage measurement experiment, a source can generate an voltage output of $V_s = 0$ or $V_s = V_1$ randomly. Due to measurement noise, the measurements (V) will be fluctuating around these two numbers according to the probability density functions (PDF) $pr(V|H_0)$ and $pr(V|H_1)$. Therefore, mathematically, the measurements corresponding to the underlying hypotheses can be described as:

$$H_0 : V = 0 + n, \quad (2.7)$$

and

$$H_1 : V = V_1 + n, \quad (2.8)$$

where n is the measurement noise. If n is a zero mean Gaussian with variance σ , then the two PDFs $pr(V|H_0)$ and $pr(V|H_1)$ are both Gaussians with the same variance (σ) but different means: 0 for H_0 and V_1 for H_1 (see figure 2.5). The overlap between the

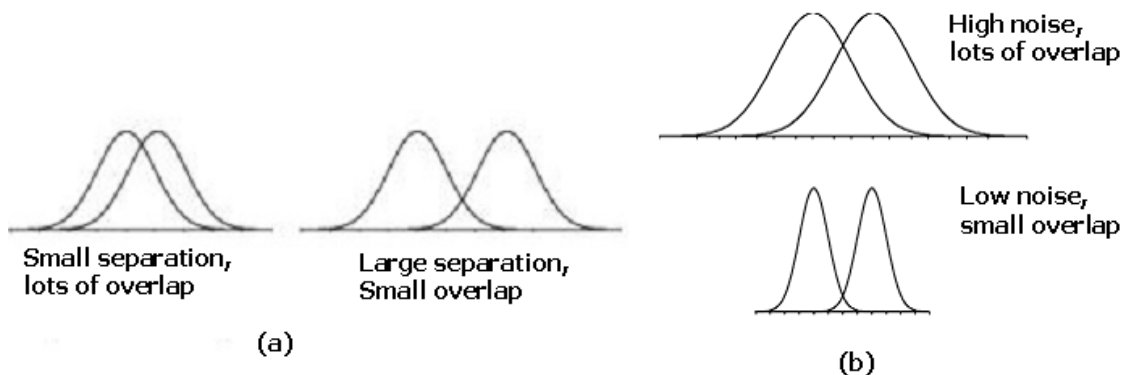


FIGURE 2.6. (a) A greater separation between the means of the two hypotheses. (b) A small spread results in less overlap between the two PDFs.

PDFs corresponds to an ambiguity region: measurements falling into this region may have originated from H_0 or H_1 . The larger the overlap, the less certain an observer can be in correctly detecting the underlying hypotheses. To decrease the overlap, thus to increase the detectability of the two hypotheses, one can either move the two curves further apart (larger separation between the two means, stronger signal, see figure 2.6(a)) or decrease the spread of the PDFs (smaller variance of the PDF, less noise, see figure 2.6(b)). Therefore, intuitively, a measure of detectability regarding the two hypotheses with respect to the noise can be described by the ratio between the separation and the spread. Mathematically, the index of detectability (d_a) for the two hypotheses based on the observations of a random quantity (λ) can be defined as [37]

$$d_a^2 = \frac{[E(\lambda|H_1) - E(\lambda|H_0)]^2}{P_1 \text{var}(\lambda|H_1) + P_0 \text{var}(\lambda|H_0)}, \quad (2.9)$$

where $E(\lambda|H_i)$ is ensemble average of the random quantity λ over hypothesis H_i , and $\text{var}(\lambda|H_i)$ the corresponding variance. The quantities P_0 and P_1 are the a priori probabilities of occurrence of hypothesis H_0 and H_1 , respectively, satisfying $P_0 + P_1 = 1$. The primary virtue of the index of detectability is that its value does not depend upon the decision threshold the observer adopts.

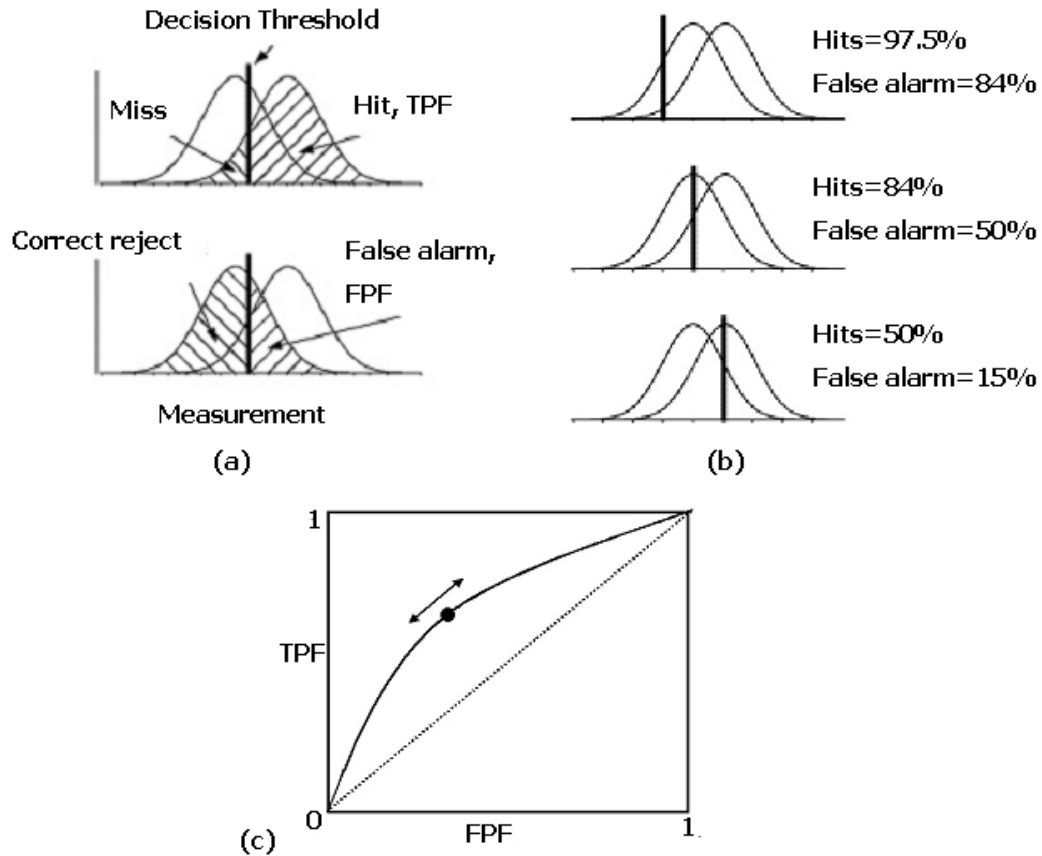


FIGURE 2.7. (a) The hit rate (TPF) corresponds to the area under the PDF $pr(V|H_1)$ to the right of the threshold, while the false alarm (FP) corresponds to the area under the PDF $pr(V|H_0)$ to the right of the threshold. (b) Changes in TPF and FPF in response to change in the threshold level. (c) Change of location of observer in the ROC graph.

Area Under Curve (AUC)

Figure 2.7 illustrates how the threshold level affects the location of a classifier in an ROC graph. The TPF of a classifier is the area under the probability density function $pr(V|H_1)$ and to the right of the threshold level. Similarly, the FPF is the area under $pr(V|H_0)$ and to the right of the the threshold. As the decision threshold changes, the resulting TPF and FPF will change accordingly. Therefore, the position

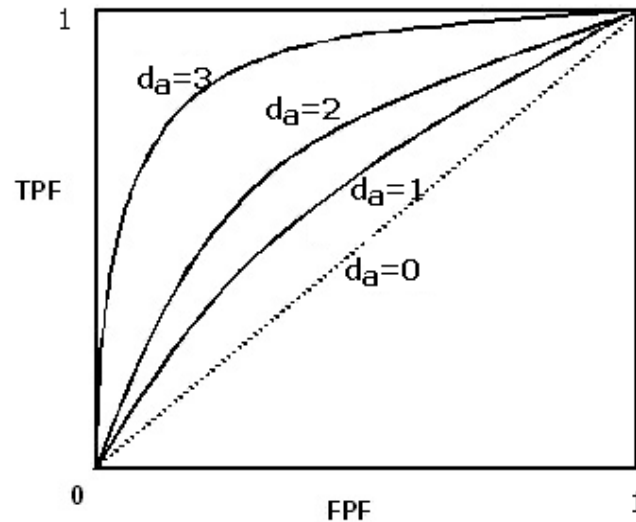


FIGURE 2.8. Schematic illustration of the generic relationship between AUC and the index of detectability (d_a).

of the classifier on the ROC graph will trace out a curve in response to changes in the threshold level (see figure 2.7(c)).

The area under this curve (area under curve, AUC) is another figure of merit used for evaluating the performance of classifiers ([38], and [39]). Since the ROC graph is bounded by a square of unit area, the values of AUC are bounded between (0, 1). However, as mentioned in §2.2.2 (ROC curve), a well designed classifier should always reside above the diagonal chance line. Therefore, a realistic classifier should have an AUC equal or larger than 0.5. In clinical diagnosis, physicians usually seek classifiers with an AUC greater than 0.85. There is a direct relationship between the index of detectability and the AUC. As the index of detectability increases, the ROC curve of an observer will curve upward toward the upper right corner (see figure 2.8), and therefore, result in a greater AUC. It can be shown that, when the test statistic is normally distributed with the same variance under the two hypotheses, the area under the ROC curve can be derived from the index of detectability through the

following relationship:

$$AUC = \frac{1}{2} + \frac{1}{2} \operatorname{erf}\left[\frac{d_a}{2}\right], \quad (2.10)$$

where $\operatorname{erf}[x]$ is the error function relating to the Gaussian distribution:

$$\operatorname{erf}(x) = \frac{2}{\sqrt{\pi}} \int_0^x \exp(-t^2) dt.$$

On the other hand, if the AUC of a classifier is known, the index of detectability of the classifier can be obtained by inverting eq. (2.10).

2.2.4 Likelihood Ratio and Quadratic Observer

The ideal Bayesian observer is a mathematical observer which bases its decision on the likelihood ratio. The likelihood ratio is defined as the ratio of the probability of the data given hypothesis H_1 to the probability of the data given under the alternative hypothesis H_0 ,

$$L = \frac{p(\mathbf{g}|H_1)}{p(\mathbf{g}|H_0)}. \quad (2.11)$$

If the probability density function of \mathbf{g} given hypothesis H_i , $p(\mathbf{g}|H_i)$, is a multivariate Gaussian:

$$p(\mathbf{g}|H_i) = (2\pi)^N (|\mathbf{K}_i|)^{-1/2} \exp\left[-\frac{1}{2}(\mathbf{g}-\bar{\mathbf{g}}_i)^t \mathbf{K}_i^{-1}(\mathbf{g}-\bar{\mathbf{g}}_i)\right],$$

where

$$\bar{\mathbf{g}}_i = \langle \mathbf{g}|H_i \rangle,$$

and \mathbf{K}_i is the $N \times N$ covariance matrix under hypothesis H_i , then the likelihood ratio in eq. (2.11) can be written as [3]

$$\Lambda = \frac{\operatorname{Exp}\left[-\frac{1}{2}(\mathbf{g}-\bar{\mathbf{g}}_1)^t \mathbf{K}_1^{-1}(\mathbf{g}-\bar{\mathbf{g}}_1)\right]}{\operatorname{Exp}\left[-\frac{1}{2}(\mathbf{g}-\bar{\mathbf{g}}_0)^t \mathbf{K}_0^{-1}(\mathbf{g}-\bar{\mathbf{g}}_0)\right]} \underset{H_0}{\overset{H_1}{\gtrless}} \Lambda_c. \quad (2.12)$$

As shown in the Appendix A, in this analysis, the mean of the demodulated OCT data is zero. Therefore, we will let $\bar{\mathbf{g}}_0 = \bar{\mathbf{g}}_1 = 0$ in eq. (2.12). By taking logarithm to both sides of eq. (2.12), the corresponding log-likelihood ratio can be written as

$$\lambda(\mathbf{g}) = -\frac{1}{2} \mathbf{g}^t (\mathbf{K}_1^{-1} - \mathbf{K}_0^{-1}) \mathbf{g} \underset{H_0}{\overset{H_1}{\gtrless}} \lambda_c. \quad (2.13)$$

In eq. (2.13), the test statistic $\lambda(\mathbf{g})$ is quadratic in the data set \mathbf{g} . Therefore, any observer adopting such a test statistic for its decision strategy is termed a quadratic observer. Let

$$\lambda'(\mathbf{g}) = \mathbf{g}^t \mathbf{A} \mathbf{g} = \sum g_m a_{mn} g_n, \quad (2.14)$$

with

$$\mathbf{A} = (\mathbf{K}_1^{-1} - \mathbf{K}_0^{-1}). \quad (2.15)$$

Using $\lambda'(\mathbf{g})$ as the test statistic, for the case that the two hypothesis have equal prevalences (ie., $P_1 = P_0$ in eq. (2.9)), then the index of detectability of $\lambda'(\mathbf{g})$ can be written as (see eq. (2.9)):

$$d_a^2 = \frac{2[E(\lambda'|H_1) - E(\lambda'|H_0)]^2}{\text{var}(\lambda'|H_0) + \text{var}(\lambda'|H_1)}. \quad (2.16)$$

In the next few sections, we will demonstrate the evaluation of the means and variances of λ' with respect to the two hypotheses.

Ensemble average of Test Statistic

Using eq. (2.14), the ensemble average of λ' can be written as

$$E(\lambda'|H_i) = \langle \mathbf{g}^t \mathbf{A} \mathbf{g} \rangle_i = \langle \sum_{m,n} a_{mn} g_m g_n \rangle_i = \sum_{m,n} a_{mn} \langle g_m g_n \rangle_i. \quad (2.17)$$

Since

$$\langle g_m g_n \rangle_i = (\mathbf{K}_i)_{mn} = (\mathbf{K}_i)_{nm},$$

with \mathbf{K}_i a symmetric matrix, then $E(\lambda'|H_i)$ can be written as

$$\begin{aligned} E(\lambda'|H_i) &= \sum_{m,n} a_{mn} (\mathbf{K}_i)_{nm} \\ &= \sum_n \left(\sum_m (\mathbf{K}_i)_{nm} a_{mn} \right) \\ &= \text{tr}\{\mathbf{K}_i \mathbf{A}\}. \end{aligned} \quad (2.18)$$

Therefore, for the signal absent state, the ensemble average of λ' can be written as

$$\begin{aligned} E(\lambda'|H_0) &= \text{tr}\{\mathbf{K}_0\mathbf{A}\} \\ &= \text{tr}\{\mathbf{K}_0\mathbf{K}_1^{-1} - \mathbf{I}\}, \end{aligned} \quad (2.19)$$

and similarly, for the signal present state,

$$\begin{aligned} E(\lambda'|H_1) &= \text{tr}\{\mathbf{K}_1\mathbf{A}\} \\ &= \text{tr}\{\mathbf{I} - \mathbf{K}_1\mathbf{K}_0^{-1}\}. \end{aligned} \quad (2.20)$$

Variance of Test Statistic

The variance of λ' is defined as

$$\text{var}(\lambda'|H_i) = E(\lambda'^2|H_i) - (E(\lambda'|H_i))^2. \quad (2.21)$$

Using eq. (2.14), $E(\lambda'^2|H_i)$ can be written as

$$\begin{aligned} E(\lambda'^2|H_i) &= \left\langle \sum_{m,n} a_{mn} g_m g_n \sum_{j,k} a_{jk} g_j g_k \right\rangle_i \\ &= \sum_{m,n} \sum_{j,k} a_{mn} a_{jk} \left\langle g_m g_n g_j g_k \right\rangle_i. \end{aligned} \quad (2.22)$$

Since it is assumed that g_m are Gaussian random variables, then the fourth moment $\left\langle g_m g_n g_j g_k \right\rangle_i$ can be broken down as [40]:

$$\begin{aligned} &\left\langle g_m g_n g_j g_k \right\rangle_i = \left\langle g_m g_n \right\rangle_i \left\langle g_j g_k \right\rangle_i \\ &+ \left\langle g_m g_j \right\rangle_i \left\langle g_n g_k \right\rangle_i + \left\langle g_m g_k \right\rangle_i \left\langle g_n g_j \right\rangle_i. \end{aligned} \quad (2.23)$$

Then eq. (2.22) can be written as,

$$\begin{aligned} E(\lambda'^2|H_i) &= \sum_{m,n} \sum_{j,k} a_{mn} a_{jk} (\mathbf{K}_i)_{mn} (\mathbf{K}_i)_{jk} + \sum_{m,n} \sum_{j,k} a_{mn} a_{jk} (\mathbf{K}_i)_{mj} (\mathbf{K}_i)_{nk} \\ &+ \sum_{m,n} \sum_{j,k} a_{mn} a_{jk} (\mathbf{K}_i)_{mk} (\mathbf{K}_i)_{nj} \end{aligned} \quad (2.24)$$

The first term in eq. (2.24) can be evaluated as

$$\begin{aligned}
& \sum_{m,n} \sum_{j,k} a_{mn} a_{jk} (\mathbf{K}_i)_{mn} (\mathbf{K}_i)_{jk} \\
&= \sum_{m,n} a_{mn} (\mathbf{K}_i)_{mn} \sum_{j,k} a_{jk} (\mathbf{K}_i)_{jk} \\
&= (E(\lambda' | H_i))^2.
\end{aligned} \tag{2.25}$$

The second term is

$$\begin{aligned}
& \sum_{m,n} \sum_{j,k} a_{mn} a_{jk} (\mathbf{K}_i)_{mj} (\mathbf{K}_i)_{nk} \\
&= \sum_{m,n} \sum_{j,k} (\mathbf{K}_i)_{mj} a_{mn} a_{jk} (\mathbf{K}_i)_{kn} \\
&= \sum_{j,n} \left(\sum_m (\mathbf{K}_i)_{jm} a_{mn} \sum_k a_{jk} (\mathbf{K}_i)_{kn} \right) \\
&= \text{tr}\{(\mathbf{K}_i \mathbf{A})^t (\mathbf{A} \mathbf{K}_i)\},
\end{aligned} \tag{2.26}$$

and, similarly, the third term is

$$\begin{aligned}
& \sum_{m,n} \sum_{j,k} a_{mn} a_{jk} (\mathbf{K}_i)_{mk} (\mathbf{K}_i)_{nj} \\
&= \sum_{j,m} \left(\sum_k a_{jk} (\mathbf{K}_i)_{km} \sum_n a_{mn} (\mathbf{K}_i)_{nj} \right) \\
&= \text{tr}\{(\mathbf{A} \mathbf{K}_i) (\mathbf{A} \mathbf{K}_i)\}.
\end{aligned} \tag{2.27}$$

Then eq. (2.24) can be written as

$$E(\lambda'^2 | H_i) = (E(\lambda' | H_i))^2 + \text{tr}\{(\mathbf{K}_i \mathbf{A})^t (\mathbf{A} \mathbf{K}_i)\} + \text{tr}\{(\mathbf{A} \mathbf{K}_i)^2\}. \tag{2.28}$$

Since both \mathbf{K}_i and \mathbf{A} are symmetric matrices,

$$(\mathbf{K}_i \mathbf{A})^t = \mathbf{A} \mathbf{K}_i,$$

then, using eq. (2.18), the variance of λ' can be written as

$$E(\lambda'^2 | H_i) = (E(\lambda' | H_i))^2 + 2\text{tr}\{(\mathbf{A} \mathbf{K}_i)^2\}. \tag{2.29}$$

Therefore, using eqs. (2.21 and 2.29), for the signal absent state, the variance for the test statistic can be written as

$$\begin{aligned} \text{var}(\lambda'|H_0) &= 2\text{tr}\{(\mathbf{A}\mathbf{K}_0)^2\} \\ &= 2\text{tr}\{(\mathbf{K}_1^{-1}\mathbf{K}_0 - \mathbf{I})^2\}. \end{aligned} \quad (2.30)$$

Similarly, for the signal present state,

$$\begin{aligned} \text{var}(\lambda'|H_1) &= 2\text{tr}\{(\mathbf{A}\mathbf{K}_1)^2\} \\ &= 2\text{tr}\{(\mathbf{I} - \mathbf{K}_0^{-1}\mathbf{K}_1)^2\}. \end{aligned} \quad (2.31)$$

Then we can use eqs. (2.16, 2.19, 2.20, 2.30, and 2.31) to evaluate the detectability for a detection task.

Chapter 3

STOCHASTIC WAVES

Wave phenomena are ubiquitous in our life. Our vision, hearing, the tides of the ocean, wireless communications channels, TV and radio broadcasting, earthquakes, etc., are all related to waves – the most frequent form of energy transmission. Literature on wave phenomena abounds, and diverse sub-fields have grown out from different aspects of the same phenomena. For example, according to its physical nature, wave phenomena can be categorized as a subject in acoustics, optics, radiophysics, geophysics, mechanics and other related disciplines. A great number of investigations in classical wave analysis have been made on deterministic problems such as antenna design, diffraction and scattering of light, guided waves, etc.. Depending on the nature of the investigation and the required accuracies, the deterministic approach works fine for a particular set of problems such as those just mentioned. However, a lot of wave phenomena involve many uncontrollable factors such as fluctuations in the refractive index of the media in which the waves propagate. For such phenomenon, deterministic modelling is not an adequate presentation of the problem at hand, and a stochastic description based on probability theory is necessary.

Stochastic wave phenomena by nature are complex and intractable. Therefore, there is still not one unified analytical theory that can encompass the many facets of this phenomenon. Diverse tools and approximations are thus developed to study specific aspects of stochastic wave phenomena, depending on the physical nature of the waves in question (electromagnetic waves, mechanical waves, etc.), or depending on the properties of the inhomogeneity of the medium and the surface involved (size of inhomogeneity in relation to wavelength, inhomogeneities distributed in a continuous manner, inhomogeneities in the form of randomly distributed discrete scattering

elements, etc.). Moreover, distinctions can be made between stochastic wave phenomena relating to the volume factors or the surface factors of the media. The volume factors relate to the inhomogeneity and uncertainty of the structure of the wave-transmitting media (e.g., turbulent atmosphere, irregular composite materials, soils—the subject of mechanics and geophysics, biological tissue) and lead to the problems of wave propagation in stochastic media. The surface factors relate to the random irregularities of surfaces separating media with different properties (e.g., the surface of the sea, the roughness of metal surfaces, and the like) and lead in turn to the analysis of the scattering of waves at stochastic surfaces.

It should be emphasized, however, that apart from the differences of the above mentioned particular problems, scattering is the one basic physical principle underlying all these diverse phenomena. The effect of the scattered wave on the primary (incident) wave and the other scattered waves cause fluctuations in amplitudes, phases, propagation velocities, and polarizations of the observed total field.

3.1 Early Studies in Scattering

The Irish scientist, John Tyndall (1820-1893), was the first to observe the scattering of natural light by particles and the bluish hue in the scattered radiation, which is termed ‘Tyndall blue’ for the sky color. Lord Rayleigh later provided a theoretical explanation for this effect, showing that the intensity of light scattered by a set of independent particles with dimension smaller than the incident wavelength is inversely proportional to the fourth power of the wavelength. Such scattering of light by particles smaller than the wavelength is therefore termed Rayleigh scattering, while the scattering from larger particles is Mie scattering.

In classical mechanics, scattering refers to the deflection of the trajectory of a particle due to a collision, or an interaction with some other entity. The analogy in optics will be the deflection of the light quanta—photon, though scattering of light

in general involves the absorption and re-emission of a photon. On the other hand, considering light as a wave phenomena, a microscopic description of light scattering can be formulated using Maxwell's equations of electromagnetic field, with the appropriate distribution of charges and currents representing the medium. When the external electric field impinges on the medium, electric moments are induced in the matter and act as secondary sources of radiation. Therefore, the frequency shift, polarization, angular distribution, and the intensity of the scattered field are determined by the characteristics of the medium as well as the incident field.

Consider a subregion inside the illuminated volume. If the dimension of the subregion is small compared to the incident wavelength, it can be assumed that all the atoms (or molecules) in this subregion are driven by the same field. The total scattered field from the volumetric medium will be the superposition of all the secondary fields radiated by these subregions. If all the subregions are optically identical, ignoring surface effects and assuming the medium is reasonably large, then the superposition will result in a forward propagating scattered field. The reason is that all the secondary fields are identical except for a phase factor depending on the relative position of the subregions. For a large enough medium, each subregion can be paired with another one whose scattered field is identical in amplitude but opposite in phase and thus will cancel. However, if the subregions are optically different (e.g., different dielectric constants), the superposition of all the secondary wavelets will result in a scattered field in directions other than the forward direction. Thus in this semi-macroscopic view, originally introduced by Einstein, light scattering results from local fluctuations in the dielectric constant of the medium [41].

The microscopic theory of light scattering based on its interaction with charged particles, though exact in principle, is tedious mathematically. Therefore, appropriate approximations such as Born approximation and Rytov approximation have been introduced to simplify the analysis of certain classes of stochastic wave phenomena.

3.2 Stochastic Wave Propagation in Continuum

Stochastic waves can be investigated on the basis of the stochastic Helmholtz equation. We will start the discussion with a description of the permittivity field of the medium

$$\varepsilon(\mathbf{r}, t) = n^2(\mathbf{r}, t) = \varepsilon'(\mathbf{r}, t) + i\varepsilon''(\mathbf{r}, t), \quad (3.1)$$

where n is the refractivity index of the medium. In general, $\varepsilon(\mathbf{r}, t)$ can be a complex number. For a random medium, the permittivity field can be written as

$$\varepsilon(\mathbf{r}, t) = \langle \varepsilon(\mathbf{r}, t) \rangle (1 + \tilde{\varepsilon}(\mathbf{r}, t)), \quad (3.2)$$

where $\langle \varepsilon(\mathbf{r}, t) \rangle$ is the mean permittivity of the medium and $\tilde{\varepsilon}(\vec{r}, t)$ describes the relative fluctuation of the permittivity field. Starting with the wave equation, the propagation of an electromagnetic field inside a medium can be described as [42]:

$$\begin{aligned} & \nabla^2 \mathbf{E} + k^2 \mathbf{E} \\ = & -k^2 \tilde{\varepsilon} \mathbf{E} - \nabla[\mathbf{E} \cdot \nabla(\tilde{\varepsilon})] - \frac{2ik}{c} \frac{\partial}{\partial t} [(1 + \tilde{\varepsilon}) \mathbf{E}] + \frac{\langle \varepsilon \rangle}{c^2} \frac{\partial^2}{\partial t^2} [(1 + \tilde{\varepsilon}) \mathbf{E}], \end{aligned} \quad (3.3)$$

where $k^2 = k_0^2 \langle \varepsilon \rangle$ is the wave number in the medium, while k_0 is the wave number in free space. The two terms in the first line of eq. (3.3) correspond to the Helmholtz operator. The first term in the second line is the source term of the co-polarized scattered field. The second term corresponds to the depolarized term. The third term describes the phase delay of the electromagnetic field due to temporal variations of $\tilde{\varepsilon}(\mathbf{r}, t)$, and the fourth term the temporal variation of the field amplitude. If the temporal variation of $\tilde{\varepsilon}(\mathbf{r}, t)$ is small, eq. (3.3) can be further simplified as

$$\nabla^2 \mathbf{E} + k^2 \mathbf{E} = -k^2 \tilde{\varepsilon} \mathbf{E} - \nabla[\mathbf{E} \cdot \nabla \tilde{\varepsilon}]. \quad (3.4)$$

This equation is referred to as the vector stochastic wave equation. When the wavelength of the EM field λ is larger than the smallest size of the inhomogeneities in the permittivity field (l_0), the depolarized effect described by the second term in

eq. (3.4) is appreciable. When depolarization is not negligible, a complete analysis for the wave propagation will involve the dyadic Green function ([42] and [43]). If one ignores the depolarization term, eq. (3.4) can be written as

$$\nabla^2 E_i + k^2 E_i = -k^2 \tilde{\epsilon} E_i, \quad (3.5)$$

where E_i is the scalar component of the vector field \mathbf{E} . This equation is usually referred to as the scalar stochastic wave equation, or the stochastic Helmholtz equation, and is the starting point of most stochastic wave analysis.

The wave equations described are partial differential equation with random variables. However, a comprehensive theory of stochastic differential equations and the associated boundary value problems is still under development. Therefore, most analytical mathematical methods in stochastic wave analysis are restricted to the simplest models and problems.

3.2.1 Weak Fluctuation Approximation

A vast majority of studies in stochastic wave phenomena are developed upon the assumption that the random medium is weakly inhomogeneous. This means that the fluctuations of the medium properties are sufficiently small. Then one can study the wave processes using perturbation theory by expanding the quantity under investigation into a series expansion with respect to a small parameter. The Born approximation is one of the oldest and most well known procedure for stochastic wave analysis based on the perturbation approach. The Born method is simple but is restricted to a certain type of application. Other methods with their roots in the perturbation approach include the method of geometric optics (eikonal approximation) and the Rytov method [44]. Reference [45] gives an extensive discussion of the physical aspects of geometrical optics in a stochastic medium, including the discussion of the applicability range. The diffusion (parabolic) approximation ([46] and [47]), in

which the Laplacian operator in the wave equation is replaced by a transverse Laplacian operator, is another commonly used approximation in the analysis for medium dominated by large scale inhomogeneities. Another direction for the study of stochastic wave phenomena is the functional approach, which studies the characteristic functionals describing the randomness of the system ([48], [49], and [50]). In this work, we will only describe the Born approximation. For the other methods such as the Rytov and eikonal method, interested readers can inquire excellent books such as [51] and [47].

3.2.2 Born Approximation

Applying perturbation theory to the stochastic Helmholtz equation (eq. (3.5), we will introduce the small parameter μ into the expression of the permittivity field (eq. (3.2))

$$\varepsilon(\mathbf{r}, t) = \langle \varepsilon(\mathbf{r}) \rangle (1 + \mu \tilde{\varepsilon}(\mathbf{r})), \quad (3.6)$$

and assume the solution for (eq. (3.5)) in the form of an expansion in the powers of μ :

$$E = E^{(0)} + \mu E^{(1)} + \mu^2 E^{(2)} + \dots \quad (3.7)$$

The zeroth order approximation $E^{(0)}$ satisfies the homogeneous Helmholtz equation:

$$\nabla^2 E^{(0)} + k^2 E^{(0)} = 0, \quad (3.8)$$

and will be referred to as the incident field E_{inc} . The first order correction $E^{(1)}$ satisfies the following equation

$$\nabla^2 E^{(1)} + k^2 E^{(1)} = -k^2 \tilde{\varepsilon} E^{(0)}, \quad (3.9)$$

and the second order correction $E^{(2)}$ satisfies

$$\nabla^2 E^{(2)} + k^2 E^{(2)} = -k^2 \tilde{\varepsilon} E^{(1)}, \quad (3.10)$$

and so on for the higher order corrections.

Introducing the Green function of the Helmholtz operator

$$G(\mathbf{r}, \mathbf{r}') = -\frac{\exp[ik|\mathbf{r} - \mathbf{r}'|]}{4\pi|\mathbf{r} - \mathbf{r}'|}, \quad (3.11)$$

then the solution for eq. (3.9) can be written as

$$\begin{aligned} E^{(1)}(\mathbf{r}) &= -k^2 \int d\mathbf{r}' \tilde{\varepsilon}(\mathbf{r}') G(\mathbf{r}, \mathbf{r}') E^{(0)}(\mathbf{r}') \\ &\equiv \int d\mathbf{r}' \mathcal{V}(\mathbf{r}') G(\mathbf{r}, \mathbf{r}') E^{(0)}(\mathbf{r}'), \end{aligned} \quad (3.12)$$

where

$$\mathcal{V}(\mathbf{r}') = -k^2 \tilde{\varepsilon}(\mathbf{r}'), \quad (3.13)$$

is the scattering potential corresponding to the random medium. Similarly, the second order correction can be written as

$$\begin{aligned} E^{(2)}(\mathbf{r}) &= \int d\mathbf{r}' \mathcal{V}(\mathbf{r}') G(\mathbf{r}, \mathbf{r}') E^{(1)}(\mathbf{r}') \\ &= \int d\mathbf{r}'_2 \int d\mathbf{r}'_1 G(\mathbf{r}, \mathbf{r}'_2) G(\mathbf{r}, \mathbf{r}'_1) \mathcal{V}(\mathbf{r}'_1) \mathcal{V}(\mathbf{r}'_2) E^{(0)}(\mathbf{r}'_1). \end{aligned} \quad (3.14)$$

The first order correction $E^{(1)}(\mathbf{r})$ corresponds to the effect of single scattering of the incident field E_{inc} , while the higher order corrections $E^{(i)}(\mathbf{r})$ describe the effect of the higher order scatterings (multiple scattering). In the Born approximation, it is assumed that for a medium of weak fluctuation, the higher order term in the expansion can be ignored and the total field can be written as

$$E = E^{(0)} + E^{(1)}. \quad (3.15)$$

In essence, the Born approximation assumes that the effect of scattering is slight and then the field inside the medium can be approximated by the incident field instead of the real field that is modified by the multiple scattering events within the medium. As shown in reference [47], the condition for Born approximation to be valid can be stated as

$$\frac{1}{2} M k^2 D^2 \ll 1, \quad (3.16)$$

where M is the upper bound for the fluctuation

$$M > |\tilde{\varepsilon}|, \quad (3.17)$$

and D is the diameter of the scattering volume, or, the largest distance between two points belonging to the scattering volume V .

3.3 Wave in Discrete Stochastic Media

In the previous section, the Born approximation was derived in the context of a random continuum, as we modeled the random medium by a continuous function, the permittivity field $\varepsilon(\mathbf{r}, t)$. Examples of such random media include: tropospheric and ionospheric turbulence, planetary atmospheres, solar corona, turbulence in water, turbulent wakes and plumes of aircraft and rocket engines, clear air turbulence, and biological media. However, some media are better described as discrete stochastic media, or random scatterers. Examples of such media include aerosols (smog, smoke, haze, clouds, and fog), hydrometeors (water particles in solid or liquid form in the atmosphere), or blood cells in biological samples.

A discrete stochastic medium can be loosely described as an ensemble of randomly distributed discrete scatterers. The study of wave phenomena in such media can be carried out in two steps. First, the scattering and absorption characteristics of a single scatterer such as scattering amplitude, absorption and scattering cross section will be studied based on models such as Rayleigh scattering, Rayleigh-Debye approximation, WKB approximation, and Mie theory [51]. Then the wave characteristics of the wave in a discrete random medium will be derived by combining all the contributions from each individual scatterer inside the medium.

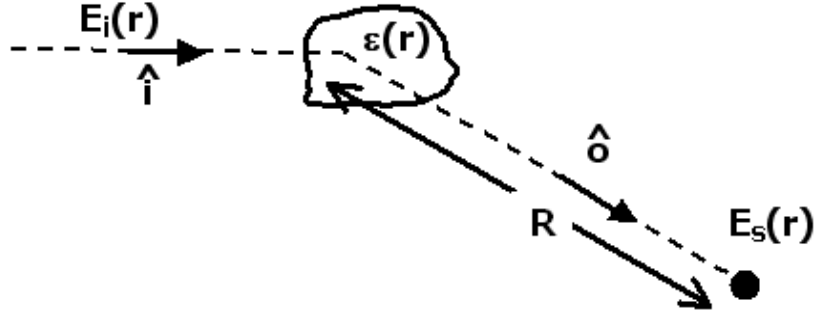


FIGURE 3.1. Geometry for a scattering problem.

3.3.1 Single Particle Analysis

The analysis of wave scattering and absorption by a single particle serves as the foundation for the study of similar phenomena in the presence of an ensemble of randomly distributed particles. Consider a single particle illuminated by an incoming plane wave

$$\mathbf{E}_i(\mathbf{r}) = \hat{\mathbf{e}}_i \exp(i\mathbf{k}\hat{\mathbf{i}} \cdot \mathbf{r}). \quad (3.18)$$

An observer \mathbf{O} is at a distance R away from the scattering particle (see Fig. 3.1). If $R > \frac{D^2}{\lambda}$, with D the dimension of the particle, it can be shown that the scattered wave behaves as a spherical wave, and can be written as [51]:

$$\mathbf{E}_s(\mathbf{r}) = \mathbf{f}(\hat{\mathbf{o}}, \hat{\mathbf{i}}) \frac{\exp(ikR)}{R}, \quad (3.19)$$

where $\mathbf{f}(\hat{\mathbf{o}}, \hat{\mathbf{i}})$ is the scattering amplitude

$$\mathbf{f}(\hat{\mathbf{o}}, \hat{\mathbf{i}}) = \frac{k^2}{4\pi} \int_V dV' \{-\hat{\mathbf{o}} \times [\hat{\mathbf{o}} \times \mathbf{E}(\mathbf{r}')] \} (\epsilon_r(\mathbf{r}') - 1) \exp(-ik\mathbf{r}' \cdot \hat{\mathbf{o}}). \quad (3.20)$$

The integral is performed over the scattering volume V (ie., the volume of the particle). It carries the information on the amplitude, the phase and the polarization of the scattered wave. The above expression is a complete description of the scattered wave. The polarization of the scattered field is determined by the term

$$-\hat{\mathbf{o}} \times [\hat{\mathbf{o}} \times \mathbf{E}] = \mathbf{E} - \hat{\mathbf{o}}[\hat{\mathbf{o}} \cdot \mathbf{E}]. \quad (3.21)$$

In general, the scattered wave is elliptically polarized even though the incident wave is linearly polarized. In the special case of a plane wave where $\hat{\mathbf{o}}$ is chosen to be perpendicular to the polarization of \mathbf{E} , thus $\hat{\mathbf{o}} \cdot \mathbf{E} = \mathbf{0}$, the scattered wave will be co-linear with the incident wave. As shown in eq. (3.20), $\mathbf{f}(\hat{\mathbf{o}}, \hat{\mathbf{i}})$ is a function of the total field $\mathbf{E}(\mathbf{r})$ inside the particle, which in turn is determined by the scattering property of the particle. In many practical situations, $\mathbf{E}(\mathbf{r})$ is approximated by some known quantity and thus a useful approximation expression for $\mathbf{f}(\hat{\mathbf{o}}, \hat{\mathbf{i}})$ can be derived.

Rayleigh Scattering

Rayleigh laid the foundation of theoretical studies in scattering with his original article published in 1871 [52]. In his studies, the scatterers were treated as assemblies of non-interacting particles sufficiently small compared to the incident wavelength and were regarded as point-dipole oscillators. In his subsequent publications, he derived an approximate theory for particles of any shape and size with a relative refractive index close to one. Following we will present the derivation of Rayleigh scattering for a sphere with dimension smaller than the incident wavelength.

For a dielectric sphere with dimension smaller than a wavelength, from basic theory of electrostatic field, the electric field \mathbf{E} inside the sphere is uniform and given by

$$\mathbf{E} = \frac{3}{\varepsilon_r + 2} \mathbf{E}_i, \quad (3.22)$$

where $\mathbf{E}_i = E_i \hat{\mathbf{e}}_i$ is the incident constant field, and ε_r the relative permittivity of the sphere. Substituting eq. (3.22) into eq. (3.20), then the scattering amplitude can be written as

$$\mathbf{f}(\hat{\mathbf{o}}, \hat{\mathbf{i}}) = \frac{k^2}{4\pi} \frac{3(\varepsilon_r - 1)}{\varepsilon_r + 2} V [-\hat{\mathbf{o}} \times (\hat{\mathbf{o}} \times \hat{\mathbf{e}}_i)], \quad (3.23)$$

The differential scattering cross section is defined as

$$\sigma_d(\hat{\mathbf{o}}, \hat{\mathbf{i}}) = \left| \mathbf{f}(\hat{\mathbf{o}}, \hat{\mathbf{i}}) \right|^2. \quad (3.24)$$

Using eq. (3.23), $\sigma_d(\widehat{\mathbf{o}}, \widehat{\mathbf{i}})$ can be written as

$$\sigma_d(\widehat{\mathbf{o}}, \widehat{\mathbf{i}}) = \frac{k^4}{(4\pi)^2} \left| \frac{3(\varepsilon_r - 1)}{\varepsilon_r + 2} \right|^2 V^2 \sin^2 \chi, \quad (3.25)$$

where

$$\sin \chi = |-\widehat{\mathbf{o}} \times (\widehat{\mathbf{o}} \times \widehat{\mathbf{e}}_i)|, \quad (3.26)$$

with χ the angle between $\widehat{\mathbf{o}}$ and $\widehat{\mathbf{e}}_i$. the angular dependence of the scattered wave $\sin \chi$ is identical to that of the dipole radiation pattern. The dependence on the fourth order of the wavelength and the square of the volume of the scatterer is the two characteristics for small scatterers.

Rayleigh-Debye Scattering (Born Approximation)

The Rayleigh-Debye approximation is used to study scattering particle with dimensions larger than the incident wavelength and with relative refractive index close to one (i.e., free space). For large particles with refractive index much different than the surroundings, the scattered field from different regions of the particle will have a complicated dependence on the location of the individual regions as well as on the electric field in the regions. It is a formidable theoretical task to treat the scattering from such particles. Only for the case of spheres does there exist a complete solution derived by Mie [53] and independently by Debye [54]. Recently, researchers have applied Mie scattering in OCT spectroscopy studies for the problem of induced dispersion by the inhomogeneities inside a biological sample [55].

The Rayleigh-Debye approximation is similar to the Born approximation derived for a random continuum in the previous section, since it assumes that the field at the scattering site can be replaced by the incident field. In the case when the relative dielectric constant of the scattering particle (ε_r) is close to the surrounding, which is unity if the particle is in vacuum, and if the condition $(\varepsilon_r - 1)kD \ll 1$ holds, then the field inside the scatterer may be approximated by the incident field

$$\mathbf{E}(\mathbf{r}) \approx \mathbf{E}_i(\mathbf{r}) = \widehat{\mathbf{e}}_i \exp(ik\widehat{\mathbf{i}} \cdot \mathbf{r}). \quad (3.27)$$

Accordingly, the scattering amplitude can be written as

$$\mathbf{f}(\widehat{\mathbf{o}}, \widehat{\mathbf{i}}) = \frac{k^2}{4\pi} \{-\widehat{\mathbf{o}} \times [\widehat{\mathbf{o}} \times \widehat{\mathbf{e}}_i]\} V S(\mathbf{k}_s), \quad (3.28)$$

where

$$S(\mathbf{k}_s) = \frac{1}{V} \int_V dV' (\varepsilon_r(\mathbf{r}') - 1) \exp(i\mathbf{k}_s \cdot \mathbf{r}'), \quad (3.29)$$

with $\mathbf{k}_s = k\widehat{\mathbf{e}}_s = k(\widehat{\mathbf{i}} - \widehat{\mathbf{o}})$, and $|\widehat{\mathbf{e}}_s| = 2 \sin(\frac{\theta}{2})$, where θ is the scattering angle between $\widehat{\mathbf{i}}$ and $\widehat{\mathbf{o}}$. Eqs. (3.28) and (3.29) show that the scattering amplitude relates to the Fourier transform of the relative dielectric constant difference $\varepsilon_r(\mathbf{r}') - 1$ evaluated at the wave number \mathbf{k}_s . Therefore, if $\varepsilon_r(\mathbf{r}') - 1$ is concentrated in an area smaller than a wavelength, one will observe a larger spread in the value of $|\mathbf{k}_s|$ and thus in θ , which results in an almost isotropic scattering. If the particle is large compared to the wavelength, the scattering will concentrate in the forward direction.

3.3.2 Ensemble of Random Scatterers

From the microscopic point of view, any random medium can be considered as a collection of randomly distributed particles. Therefore, theoretically, all the analysis can be built upon the single particle model. The full treatment of multiple scattering in random discrete media will involve first obtaining a solution for a single scatterer. Then the interactions between scatterers will be introduced to the solution. However, for any realistic random medium, the microscopic technique is mathematically tedious, even if tractable. For example, when the number of particles increases, the number of scatterings experienced by a wave increases in a random manner and is difficult to keep track of. Different approximation models were developed for the analysis of such complex random media. The simplest case will be the ‘single scattering approximation’ that applies to a tenuous distribution of particles (figure 3.2 (a)). It assumes that the wave is scattered only once before it is detected and all the multiple scattering events can be ignored. When the number of particle increases, it is

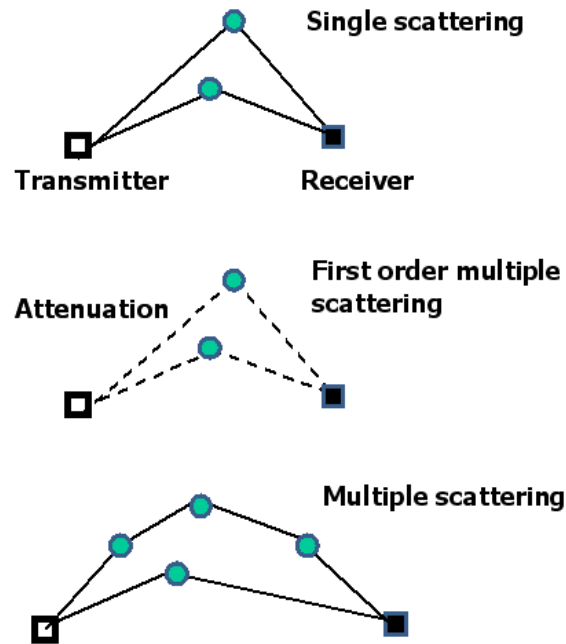


FIGURE 3.2. Illustration of single scattering, first order multiple scattering, and multiple scattering.

no longer possible to assume that the wave at the scattering site is identical to the incident wave as in the single scattering approximation. The first order correction can be made by taking into account the attenuation to the field strength due to scattering and absorption along the propagation. This is termed the ‘first order multiple scattering’ in Ishimaru’s book [51]. In this approximation, the observed wave is assumed to be scattered once by a scatterer in the medium. However, the incident field at the scattering site, as well as the observed scattered field, is attenuated due to other scattering and absorption events along the propagation. The single scattering and the first order multiple scattering approximations are applicable to a large variety of practical applications. When the distribution is dense, the ‘diffusion approximation’ will be the appropriate model. Between the extremes of dense and tenuous media, there is a range of particle densities for which multiple scattering effects are important but the above mentioned approximation models are not applicable.

Single Scattering

Consider an assemble of randomly distributed N scattering particles. When the scattering from each particle is weak, and the effect of interaction between the scattered fields and the incident field can be ignored, then the single scattering approximation can be applied to derive the total scattered field. In essence, the single scattering approximation is just another manifestation of the Born approximation: the field strength at the scattering site is not affected by the presence of the other scatterers and is assumed to be the same as the incident field. Assuming a plane wave for the incident field (see eq. (3.18)), then the total scattered field, under the single scattering approximation, can be written as (see eq. (3.19))

$$\mathbf{E}_s(\mathbf{r}) = \sum_{n=1}^N \mathcal{E}_n(\mathbf{r}) = \sum_{n=1}^N \mathbf{f}_n(\hat{\mathbf{o}}, \hat{\mathbf{i}}) \frac{\exp(ikR_n)}{R_n}, \quad (3.30)$$

where $\mathcal{E}_n(\mathbf{r})$ is the scattered field from the n^{th} scattering center, and R_n is the distance between the n^{th} scattering center and the location of the observer. The general form of the scattering amplitude is given in eq. (3.20). Approximating the field strength in eq. (3.20) by the incident field (i.e., the first Born approximation), and assuming a point scatterer, then the scattering amplitude from the n^{th} scattering center can be written as

$$\mathbf{f}_n(\hat{\mathbf{o}}, \hat{\mathbf{i}}) = \frac{k^2}{4\pi} [-\hat{\mathbf{o}} \times (\hat{\mathbf{o}} \times \hat{\mathbf{e}}_i)] \exp(i(k\hat{\mathbf{i}} - k\hat{\mathbf{o}}) \cdot \mathbf{r}_n) (\varepsilon_{r,n} - 1), \quad (3.31)$$

and eq. (3.30) can be written as

$$\mathbf{E}_s(\mathbf{r}) = \frac{k^2}{4\pi} [-\hat{\mathbf{o}} \times (\hat{\mathbf{o}} \times \hat{\mathbf{e}}_i)] \quad (3.32)$$

$$\sum_{n=1}^N \exp(i\mathbf{k}_s \cdot \mathbf{r}_n) (\varepsilon_{r,n} - 1) \frac{\exp(ikR_n)}{R_n}, \quad (3.33)$$

where $\mathbf{k}_s = k\hat{\mathbf{i}} - k\hat{\mathbf{o}}$ is the wavenumber for the scattered wave, and $\varepsilon_{r,n}$ corresponds to the strength of the permittivity field at the point scatterer. The factors $\exp(i\mathbf{k}_s \cdot \mathbf{r}_n)$ and $\frac{\exp(ikR_n)}{R_n}$ depend explicitly on the location of the point scatterers. In some

situations the spatial distribution of the point scatterers will result in a destructive interference at the observation point and thus a weaker combined field, while some other point scatterer distributions may enhance the combined field strength at the observation point. This is the effect causing the speckle structure in a spatial image or the intensity fluctuation observed in the intensity fluctuation spectroscopy in the time domain [56].

First Order Multiple Scattering Approximation

When the number density of the scattering particles is high, the effect of particles on the incident field can no longer be ignored, and first Born approximation is not applicable. The first order multiple scattering approximation is a heuristic approach to handle the effect of multiple scattering while maintaining mathematical simplicity. Visualize an assemble of coherent photons sent into a sample composed of random scatterers. Some of the photons will interact with the scatterers and be knocked out of phase with respect to the rest due to scattering, or just be absorbed by the media. The first order multiple scattering model states that, as the photons travel deeper into the sample, the number of photons that have not had any interaction with the scatterers will decrease according to an exponential law similar to the Beer's theory. In the first order multiple scattering approximation, only single scattering of such undisturbed photons will contribute to the final result. Therefore, under this approximation, the incident power of the scattered field at the receiver in figure 3.2(b) can be written as

$$P^{(1)} = P^{(0)} \exp(-\gamma), \quad (3.34)$$

where $P^{(1)}$ represents the power of the scattered field under the first order multiple scattering approximation, and $P^{(0)}$ the corresponding power without the multiple scattering event as in figure 3.2(a). The quantity γ is the optical distance that the

field experienced in the random medium, and is given by

$$\gamma = \int_0^d \mu_t(s) ds, \quad (3.35)$$

with $\mu_t(s)$ the total attenuation coefficient of the random medium:

$$\mu_t(s) = \rho(s)\sigma_t(s). \quad (3.36)$$

In eq. (3.36), ρ is the number density of the particles, and σ_t is the total cross section of the random medium due to scattering and absorption:

$$\sigma_t = \sigma_a + \sigma_s, \quad (3.37)$$

where σ_a and σ_s are the absorption cross section and the scattering cross section of the random medium, respectively. The integral in eq. (3.35) is taken along the propagation path. If there is no absorption of the radiation by the medium, σ_t will be replaced by σ_s . If ρ and σ_t are constants, then $\gamma = \rho\sigma d$, and the intensity of the unscattered radiation decay exponentially with the distance that the field traveled inside the sample.

3.4 Related Problems: Relation to Radiative Transport Theory

The theory of radiative transport is widely used in a variety of studies of optical phenomena in biological sample or some other random media. Examples include wave propagation and scattering through aerosols and hydrometeors, optical scattering from bacteria and optical diffusion in blood. Therefore, it is of interest to study the relationship between radiative transport theory and the stochastic analysis method described above.

Basically, radiative transport theory is a phenomenological theory [57] based on the heuristic observations of transport characteristics of intensities. The theory was pioneered by Schuster [58] in 1905 in the study of radiation in foggy atmospheres.

The theory studies the transport of radiation as a form of energy from one region of a random medium to another. The formulation of the radiative transport theory is built on the study of spectral energy density and specific intensity, while the wave nature of the radiation is disregarded. The effects of absorption and scattering on the radiation as it propagates through the random medium is described by a differential-integral function that is equivalent to the Boltzmann's equation used in the kinetic theory of gases and in neutron transport theory. The fact that radiative transport theory does not consider the wave nature of radiation puts a great restriction on its application in the field of coherent wave phenomena in random media.

As in the analytical stochastic wave methods, there are still no exact general solutions to transport theory. Some useful approximations exist for the limiting cases of tenuous and dense distribution (diffusion regime). Studies on deriving the heuristic transport theory from the analytical methods can be found in references [59], [60], and [61].

3.5 Some Other Interesting Topics

As mentioned before, due to the complexity of stochastic wave problems, there is not one unified mathematical model that can encompass the breadth of the diverse phenomena. Different approximations and mathematical models are thus developed for a particular set of problems in different applications. Before we end this chapter, we will give a brief discussion on some other interesting topics in stochastic wave analysis.

3.5.1 Scattering vs. Line-of-sight Propagation

The first topic is about the distinction between the term "scattering" and "line-of-site propagation". As one first starts to look into the literature published in the field

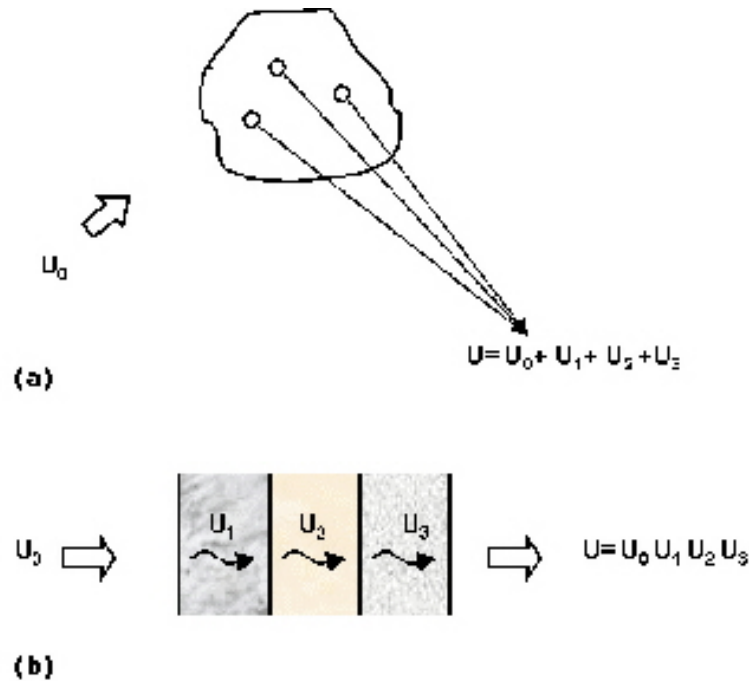


FIGURE 3.3. Illustration of (a) scattering and (b) line-of-sight problems.

of stochastic wave analysis, one will find titles such as "Scattering in..." or "Line-of-sight study of...". Basically, "scattering" and "line-of-sight" problems share the same physical principle: interaction between waves and media. However, usually, when one refers to a scattering problem, one is more concerned with the scattered field, which disappears if the random media is removed. In the line-of-sight problem, one is concerned with the total field. If the random media is removed, then the field will reduce to the incident field (see figure 3.3 [51]). The other distinction between scattering and line-of-sight problems is that, in scattering problems, the field is treated as a sum of contributions from different parts of the medium. In the line-of-sight problems, the field is treated as a product of contributions from each layer as in the Rytov approximation.

Examples of "scattering" problems include observation of small particles such as aerosols and hydrometeors by radar or lidar, and optical and acoustic scattering

in water. Line-of-sight propagation is of interests in the study of communication through the atmosphere or water. It concerns the effects of the random medium on the communication channel such as microwave and optical propagation in the atmosphere.

3.5.2 Media of Multiscale Fluctuations–Hybrid Model

The other topic is on scattering from media with fluctuations of different scales. An important parameter that plays a decisive role in the applicability of certain approximation methods is the scale of the inhomogeneity in the random media. In general, random media consist of fluctuations of different scales (compared to the incident wavelength). For example, in a biological tissue, the size of cells vary greatly from approximately $4\mu m$ for blood platelets to as much as a metre in length for nerve cells. The scattering behavior differs significantly between the large-scale and the small-scale fluctuations [14]. The larger inhomogeneities are responsible for small-angle scattering and for strong fluctuations of the intensity. When the wave propagates through the larger scale inhomogeneities, the fluctuating refractivity will bend the rays associated to the propagating wave in a random manner. The amplitude, hence the intensity, increases when the rays converge, and decreases when the rays diverge. Such random convergence gives rise to random caustics and foci, which correspond to strong fluctuations of the field intensity. This random focusing is even more pronounced in a propagating beam because of its finite dimension. On the other hand, the small inhomogeneities scatter waves at arbitrary angles, including backscattering. For example, suspended particles in the atmosphere contribute to backscattered field that is several orders of magnitude stronger than the backscatter from the purely turbulent media. Because of this distinction between large-scale and small-scale inhomogeneities, a hybrid approach was developed to study scattering of waves due to small-scale inhomogeneities in the background of the large-scale counterparts [62].

In this approach, fluctuations of permittivity $\tilde{\varepsilon}$ are divided into two components – large-scale $\tilde{\varepsilon}_L$ and small-scale $\tilde{\varepsilon}_S$. The effect of the large-scale component is described by one or another perturbation approximation (such as Rytov approximation), and the small-scale component is accounted for by the Born approximation. This approach is an extension of the distorted-wave Born approximation (DWBA) used in the quantum theory of scattering when it is applied to random media [14].

Similar to the "Born approximation", the field in the medium \mathbf{E} decomposed as a series expansion of higher order approximations:

$$\mathbf{E} = \mathbf{E}^{(0)} + \mathbf{E}^{(1)} + \mathbf{E}^{(2)} + \dots \quad (3.38)$$

In the hybrid model, the zeroth approximation $\mathbf{E}^{(0)}$ is distorted by large-scale inhomogeneities $\tilde{\varepsilon}_L$ and will be solved by applying, for example, the Rytov approximation to the following stochastic Helmholtz equation:

$$\nabla^2 \mathbf{E}^{(0)} + k^2 \mathbf{E}^{(0)} = -k^2 \tilde{\varepsilon}_L \mathbf{E}^{(0)}. \quad (3.39)$$

And the first approximation field $\mathbf{E}^{(1)}$ satisfies the following wave equation

$$\nabla^2 \mathbf{E}^{(1)} + k^2 (1 + \tilde{\varepsilon}_L) \mathbf{E}^{(1)} = -k^2 \tilde{\varepsilon}_S \mathbf{E}^{(0)}. \quad (3.40)$$

A solution for $\mathbf{E}^{(1)}$ can be written in an integral form as

$$\mathbf{E}^{(1)}(\mathbf{r}) = -k^2 \int d\mathbf{r}' \tilde{\varepsilon}_S(\mathbf{r}') G(\mathbf{r}, \mathbf{r}') \mathbf{E}^{(0)}(\mathbf{r}'), \quad (3.41)$$

where $G(\mathbf{r}, \mathbf{r}')$ is the Green's function corresponding to eq. (3.39).

Chapter 4

OPTICAL COHERENCE TOMOGRAPHY

4.1 Introduction

Optical coherence tomography (OCT) is a noninvasive optical tomographic imaging technique based on low time-coherence interferometry (LCI). It offers axial and lateral resolution of micrometer scale, and a penetration depth of a few millimeters (approximately 2-3 mm) in biological tissue. It was first devised independently, with different configuration but the same principles, in the early 1990s by Huang et al. [7] and Fercher et al. ([63] and [6]).

Figure 4.1 depicts the standard OCT scheme. A low time-coherence light source is used in a standard Michelson interferometer. Electromagnetic field is split into and recombined from the reference and sample arm. The use of a broadband source with short coherence length imposes a coherence gate to the imaging process so that interference will occur only if the optical path difference between the reference and sample arms is less than the source coherence length, which is usually in the order of micrometers. Thus a resolution of micrometers in the images can be achieved. Axial scans (i.e., the A-scan) of the sample can be done by scanning the mirror in the reference arm. By combing A-scans corresponding to adjacent transverse locations in the sample, one can produce a two dimensional cross-sectional tomography (the B-scan). The transverse (or lateral OCT) scan is typically performed by scanning the probe beam, though occasionally it is accomplished by moving the sample. By repeating the transverse scan in the other orthogonal transverse direction, a three-dimensional data set corresponding to a volumetric image (the full-field OCT) can be generated. OCT, as an imaging modality, has the following outstanding properties:

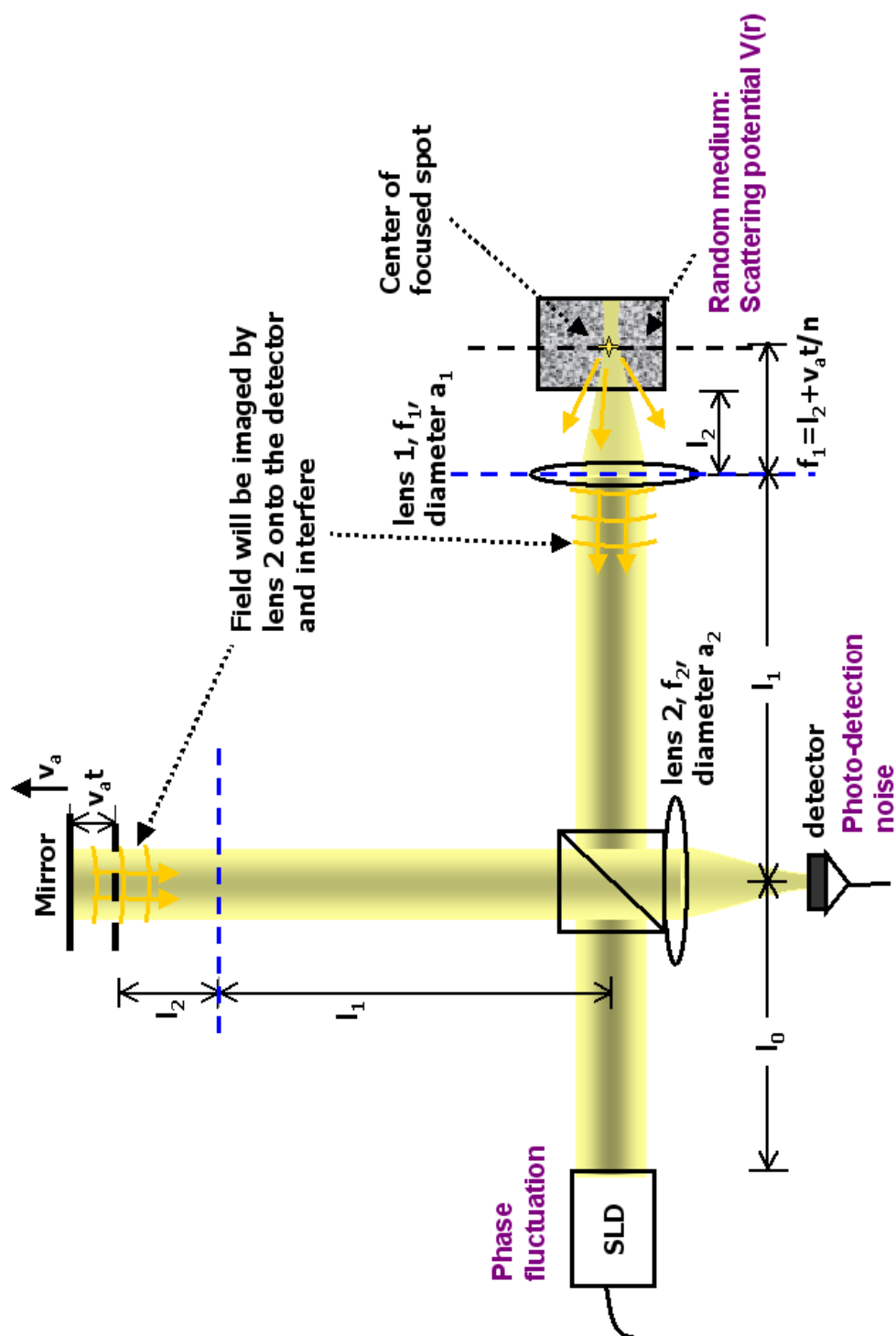


FIGURE 4.1. Free space Optical Coherence Tomography modality with dynamic focusing.

- Axial and transverse resolutions are decoupled from each other. The transverse resolution is defined by the width of the focused spot in the sample, which is determined by the NA of the optical lens used to focus the probe beam into the sample. The axial resolution of an OCT system is mainly determined by the bandwidth of the source. The first generation OCT modality demonstrated an axial resolution of $\sim 30\mu\text{m}$. With the advances of new broadband sources, sub-micron axial resolution is possible. This makes OCT superior to MRI (Magnetic Resonance Imaging) or ultrasound when minute morphological detail of the sample is desired.
- The heterodyne interferometric detection provides high dynamic range and sensitivity (>100 dB). This high sensitivity makes it possible to image weakly scattering structures in a scattering background, and thus enables ‘in situ optical biopsy’.

OCT has become a well accepted imaging modality that can provide "in-vivo" images in ophthalmology, other biomedical applications and art conservation in which different layers of paintings are analyzed. For a review of early work in LCI and OCT, see ref [64].

4.1.1 Dynamic Focusing

The transversal resolution in OCT is inherently limited by the spot size of the focused beam in the sample. As shown in [10], the transversal resolution can be defined as

$$\Delta_{trans} = 2\sqrt{\ln 2}w_0, \quad (4.1)$$

where w_0 is the beam waist inside the sample. In order to achieve high transverse resolution, a tightly focused beam inside the sample is desirable. However, due to the nature of beam optics, the tighter the beam is focused, the faster it diverges (see

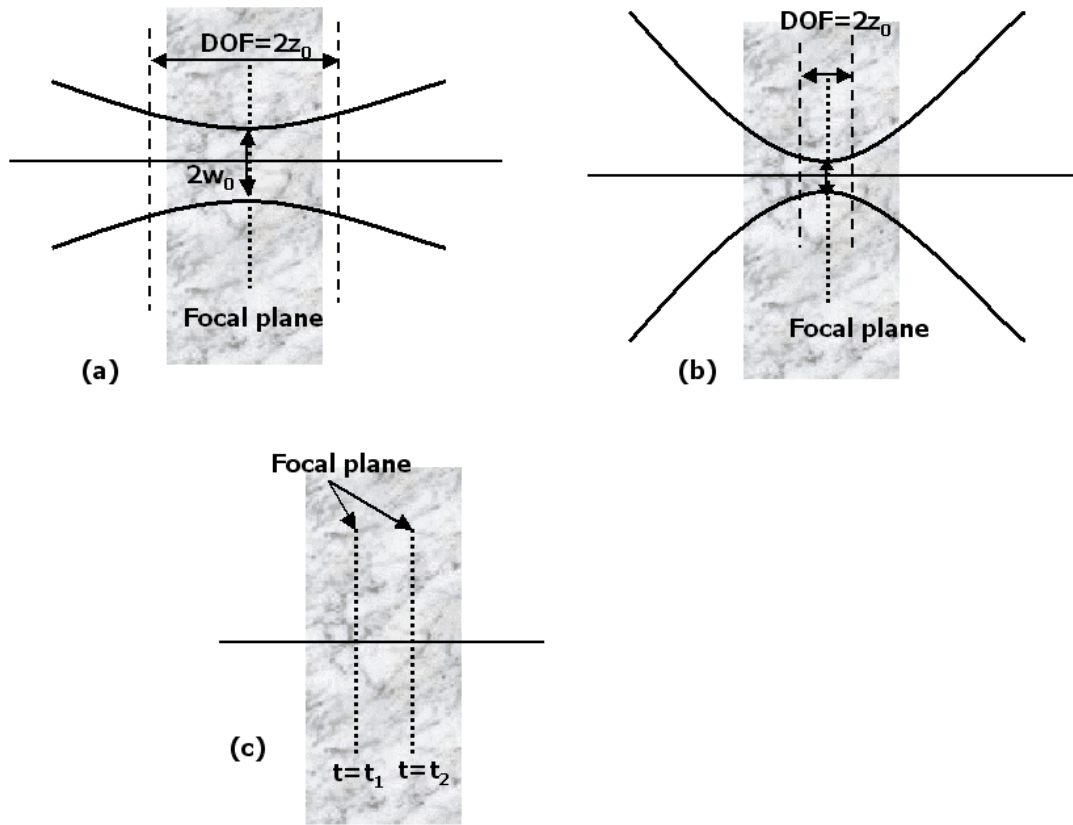


FIGURE 4.2. Relationship between beam width and depth of focus (DOF). (a) Wider beam width, longer DOF. (b) Narrower beam width, shorter DOF. (c) In dynamic focusing, the location of the focal plane inside the sample is moving in accordance with the scanning depth, which is defined by the reference mirror.

figure 4.2). Indeed, the depth of focus (DOF) of a beam is defined as twice of its Rayleigh length (z_0), which is proportional to the square of the beam waist:

$$z_0 = \frac{\pi w_0^2}{\lambda}, \quad (4.2)$$

and

$$DOF = 2z_0. \quad (4.3)$$

Therefore, in the traditional OCT modality, in which the focal plane of the sample beam is fixed to a certain location, the transverse resolution will deteriorate quickly

while the axial scan moves out of the DOF of the beam (see figure 4.2). To solve this problem, Schmitt et al. [12] proposed a dynamic focus tracking system. In such dynamic focusing system, the focal plane of the focusing lens in the sample beam moves in sync with the motion of the reference mirror such that the transversal resolution will be consistent for the complete axial scan. Recently, Murali et al. demonstrated dynamic focusing with no moving parts and a lateral resolution of less than $5 \mu\text{m}$ using liquid crystal as well as liquid lenses ([65], [66], and [67]).

4.2 Mathematical Modeling of an OCT System

We start the mathematical description of OCT by introducing some important concepts in the theory of optical coherence, which concerns the study of the random fluctuations of light. Since OCT is basically a low-coherence-time interferometer, we will emphasize the relationship between optical coherence and interference. After introducing the concepts in optical coherence, we will derive expressions for the reference and sample fields in the OCT system with considerations of the effects of a random medium on the sample field. Finally, the data acquisition and demodulation process will be addressed, and an expression of the demodulated OCT data stream will be presented.

4.2.1 Optical Coherence and Interference

Temporal Coherence and Spectrum

Consider a random field $U(\mathbf{r}, t)$, which is a random function of time and spatial position. The instantaneous (random) intensity of the field can be defined as

$$I(\mathbf{r}, t) = |U(\mathbf{r}, t)|^2, \quad (4.4)$$

which in itself is a random function. The average intensity is the ensemble average of eq. (4.4)

$$\bar{I}(\mathbf{r}, t) = \langle I(\mathbf{r}, t) \rangle = \langle |U(\mathbf{r}, t)|^2 \rangle. \quad (4.5)$$

For simplicity, from now on, we will leave out the spatial dependence by limiting the observation to a particular point in the space. For a random process of time, if the characteristics of the fluctuations do not change with time (meaning all the moments of the random process are constants), it will be referred to as statistically stationary. A less restricted condition for stationary process is referred to as stationary in the wide sense, in which its mean is independent of time, and its auto-correlation function $\langle U^*(t_1)U(t_2) \rangle$ depends only on the difference between the two time points $\tau = t_1 - t_2$. Then the temporal coherence function of a stationary random field is defined as

$$\Gamma(\tau) = \langle U^*(t)U(t + \tau) \rangle, \quad (4.6)$$

which is the auto-correlation of the random field at two different time points. The temporal coherence function describes the extent to which the random function fluctuates in phase at two different time points separated by a time delay (τ). Through the temporal coherence function, a time scale (coherence time) can be established to characterize the "memory span" of the random function. The coherence time reflects the behavior of the random mechanism driving the stochastic process. Fluctuations at points separated by a time interval larger than the coherence time are basically independent from each other, or weakly correlated. Whereas, when the time interval is smaller than the coherence time, the fluctuations are considered to be strongly correlated. The random function appears to be smoother within this time scale, but more variable when examined over a larger interval. The degree of temporal coherence can be defined as the normalized version of the temporal coherence

$$\gamma(\tau) = \frac{\Gamma(\tau)}{\Gamma(0)} = \frac{\langle U^*(t)U(t + \tau) \rangle}{\langle U^*(t)U(t) \rangle}. \quad (4.7)$$

A very important aspect of the stationary random process is its spectrum. If one expresses the random field $U(t)$ through a Fourier integral

$$U(t) = \int_{-\infty}^{\infty} \tilde{U}(\nu) \exp(-i2\pi\nu t) d\nu. \quad (4.8)$$

Then the power spectrum of $U(t)$ can be defined as (see ref. [40] for a discussion of this):

$$S(\nu) = \langle |\tilde{U}(\nu)|^2 \rangle. \quad (4.9)$$

The power spectrum $S(\nu)$ serves as a measure of the strength of the fluctuations associated with a particular Fourier component of the random field. In the rigorous sense, for a stationary random process, $U(t)$ is neither square-integrable nor absolutely integrable and hence the Fourier transform as shown in eq. (4.8) does not exist. This difficulty was removed by applying the generalized harmonic analysis first published by Wiener [68]. Following the derivation in ref. [40], it can be shown that, if $U(t)$ is a stationary process, the following relationship holds for its auto-correlation function and power spectrum,

$$S(\nu) = \int_{-\infty}^{\infty} \Gamma(\tau) \exp(i2\pi\nu\tau) d\tau, \quad (4.10)$$

and

$$\Gamma(\tau) = \int_{-\infty}^{\infty} S(\nu) \exp(-i2\pi\nu\tau) d\nu. \quad (4.11)$$

Eqs. ((4.10) and (4.11)) are known as the Wiener-Khintchine theorem. When $\Gamma(\tau)$ is a monotonically decaying function, the coherence time of the random process can be defined as the time τ_c at which $\Gamma(\tau)$ drops to a certain level, for example, $\frac{1}{2}$ or e^{-1} of its peak value. A power-equivalent width can be defined through the degree of coherence (eq. (4.7)) as a definition of coherence time [69]:

$$\tau_c = \int_{-\infty}^{\infty} |\gamma(\tau)|^2 d\tau, \quad (4.12)$$

and a corresponding coherence length in the free space can be defined as

$$l_c = c\tau_c. \quad (4.13)$$

The effective spectral range is defined as

$$(\Delta S)^2 = \frac{(\int_0^\infty S(\nu) d\nu)^2}{\int_0^\infty S^2(\nu) d\nu}. \quad (4.14)$$

By using Parseval's theorem, it can be shown that

$$\tau_c \Delta S = 1. \quad (4.15)$$

Alternatively, one can define τ_c and ΔS as [40],

$$(\tau'_c)^2 = \frac{\int_{-\infty}^\infty \tau^2 |\Gamma(\tau)|^2 d\tau}{\int_{-\infty}^\infty |\Gamma(\tau)|^2 d\tau},$$

and

$$(\Delta S')^2 = \frac{\int_0^\infty (\nu - \bar{\nu})^2 S^2(\nu) d\nu}{\int_0^\infty S^2(\nu) d\nu},$$

with

$$\bar{\nu} = \frac{\int_0^\infty \nu S^2(\nu) d\nu}{\int_0^\infty S^2(\nu) d\nu}.$$

It was shown that for simple spectral profiles, $\tau'_c \approx \tau_c$ and $\Delta S \approx \Delta S'$ ([70] and [71]). However, if the spectral profiles become more complicated, the two sets of definitions may lead to results differing by orders of magnitude. Therefore, the definitions of coherence time and spectral width need to be chosen with caution.

Degree of Coherence and Interference

The degree of coherence measures the coherence of the field and its ability to form interference fringes. If $|\gamma(\tau)| = 0$, the field is referred to as incoherent. If $|\gamma(\tau)| = 1$, the field is referred to as coherent. Anything in between, i.e., $0 < |\gamma(\tau)| < 1$, will correspond to a partially coherent field. Any realistic light wave will be partially coherent.

In the Michelson interferometry experiment, assume that a stationary partially coherent wave $U(t)$ of intensity I_0 and complex degree of coherence $\gamma(\tau)$ is used as the source. The interference between the waves from the two arms can be written as

$$I = \langle |U_1(t) + U_2(t)|^2 \rangle, \quad (4.16)$$

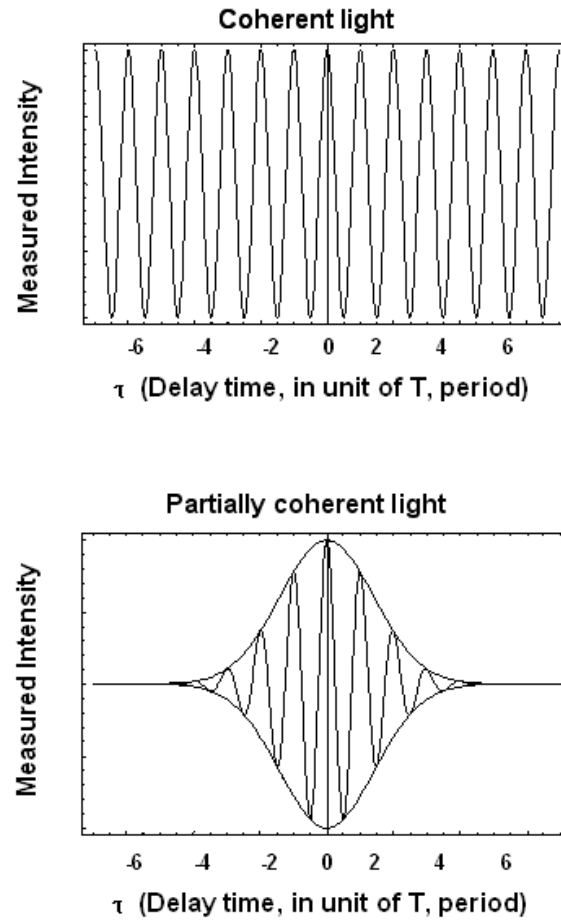


FIGURE 4.3. (a) Interferogram of a coherent source. (b) Interferogram of a partially coherent source. The visibility of the fringes decays as the delay time increases, and vanishes when the delay time is larger than the source coherent time.

where

$$U_1(t) = U(t), \quad (4.17)$$

and

$$U_2(t) = U(t + \tau) \quad (4.18)$$

represent the waves from path 1 and 2 respectively, with τ a time delay corresponding to the optical path difference between the two paths. If $|U_1(t)| = |U_2(t)| = \sqrt{\frac{I_0}{2}}$, eq. (4.16) can be written as

$$\begin{aligned} I &= \langle |U_1(t)|^2 \rangle + \langle |U_2(t)|^2 \rangle + 2 \operatorname{Re}\{\Gamma(\tau)\} \\ &= I_0[1 + |\gamma(\tau)| \cos \varphi(\tau)], \end{aligned} \quad (4.19)$$

where $\varphi(\tau)$ is the argument of the complex degree of coherence $\gamma(\tau)$. Eq. (4.19) states that the ability of a wave to interfere with its own time delayed replica is determined by the complex degree of coherence at that delay interval τ . The plot of I vs the delay time τ as shown in figure 4.3 is known as the interferogram. The width of the slow varying envelope corresponds to the coherence time of the partially coherent wave. As shown in the figure, the visibility of the interferogram decreases as τ increases and vanishes as $\tau \gg \tau_c$. In other words, interference happens only if the optical path difference between the two paths is smaller than the coherence length of the partially coherent wave.

4.2.2 Source, Reference, and Sample Fields in OCT

Source Field

In this analysis, the partially coherent source is modeled as the product of a non-fluctuating field ($U(\mathbf{r}, t)$) and a random function ($T(t)$) which describes the temporal fluctuation of the field. When observed on a plane at a distance z away from the source (assumed to be at the origin), the source field can be written as [72]:

$$E_0(\mathbf{r}, t) = U(\mathbf{r}, t)T(t), \quad (4.20)$$

where $t' = t - \frac{z}{c}$ is the retarded time from the source to the observation point. The non-fluctuating field $U(\mathbf{r}, t)$ is assumed to be coherent with a Gaussian spatial profile, i.e., a regular Gaussian beam:

$$\begin{aligned} U(\mathbf{r}, t) &= \mathcal{A}_0 \frac{w_0}{w(z)} \exp\left(-\frac{\rho^2}{w^2(z)}\right) \exp[i(k_0 z - \omega_0 t)] \exp\left[i\left(\frac{k_0 \rho^2}{2R(z)} - \phi_z\right)\right] \\ &\equiv \mathcal{U}(\mathbf{r}) \exp[i(k_0 z - \omega_0 t)], \end{aligned} \quad (4.21)$$

where \mathcal{A}_0 is the amplitude of the field. Its magnitude is given by $|\mathcal{A}_0| = \sqrt{I_0} = \sqrt{\frac{2P_0}{\pi w_0^2}}$, with P_0 the optical power of the source. The carrier frequency of the source field is ν_0 (wavelength λ_0). The propagating wave nature is described by the plane wave factor $\exp[i(k_0 z - \omega_0 t)]$, with $\mathbf{k}_0 \parallel \hat{z}$. The symbol ϕ_z represents the Guoy phase of a Gaussian beam at coordinate z . The Guoy phase is a slow function in z , except for a phase reversal (phase change of π) when passing through a focus. The beam width at coordinate z is described by $w(z) = w_0 \sqrt{1 + \left(\frac{z}{z_0}\right)^2}$, with w_0 the beam waist as it leaves the source (usually a superluminescent diode (SLD)), and z_0 the Rayleigh length of the Gaussian beam. The coherence function for the source field is

$$\begin{aligned} \Gamma(\mathbf{r}_1, \mathbf{r}_2, \tau) &= \langle E_0^*(\mathbf{r}_1, t) E_0(\mathbf{r}_2, t + \tau) \rangle_F \\ &= \mathcal{U}^*(\mathbf{r}_1) \mathcal{U}(\mathbf{r}_2) \exp[i(k_0(z_2 - z_1) - \omega_0 \tau)] \langle T^*(t) T(t + \tau) \rangle_F, \end{aligned} \quad (4.22)$$

where $\langle \dots \rangle_F$ represent the ensemble average over all the possible realizations of the source field. Letting $\mathbf{r}_1 = \mathbf{r}_2 = \mathbf{r}$ in eq. (4.22), then the temporal coherence function can be written as

$$\Gamma(\mathbf{r}, \mathbf{r}, \tau) = |\mathcal{U}(\mathbf{r})|^2 \exp(-i\omega_0 \tau) \langle T^*(t) T(t + \tau) \rangle_F. \quad (4.23)$$

In most cases, the power spectrum of many light sources used in OCT can be approximated by a normalized Gaussian spectrum

$$\Sigma(\nu) = \frac{S(\nu)}{\Gamma(0)} = \left(\frac{\Delta\nu\sqrt{\pi}}{2\sqrt{\ln 2}}\right)^{-1} \exp[-4 \ln 2 \left(\frac{\nu - \nu_0}{\Delta\nu}\right)^2]. \quad (4.24)$$

By taking the Fourier transformation of the normalized power spectrum (eq. (4.24)), the degree of temporal coherence can be written as

$$\gamma(\tau) = \exp[-(\frac{\pi\Delta\nu\tau}{2\sqrt{\ln 2}})^2] \exp(-i2\pi\nu_0\tau). \quad (4.25)$$

Using eqs. ((4.23) and (4.25)), it can be shown that

$$\langle T^*(t)T(t+\tau) \rangle_F = |\gamma(\tau)| = \exp[-(\frac{\pi\Delta\nu\tau}{2\sqrt{\ln 2}})^2]. \quad (4.26)$$

The coherence time of the source can be evaluated by using eq. (4.12)

$$\tau_c = \sqrt{\frac{2\ln 2}{\pi}} \frac{1}{\Delta\nu}, \quad (4.27)$$

and the corresponding coherence length in free space is

$$l_c = \sqrt{\frac{2\ln 2}{\pi}} \frac{c}{\Delta\nu}. \quad (4.28)$$

Using eqs. (4.15 and 4.27), the effective spectral range, which describes the bandwidth of the source, can be written as

$$\Delta S = \frac{1}{\tau_c} = \sqrt{\frac{\pi}{2\ln 2}} \Delta\nu. \quad (4.29)$$

Upon leaving the SLD, the source field will propagate for a distance of l_0 and then split into the sample field

$$E_s(\mathbf{r}, t) = \alpha_s E_0(\mathbf{r}, t), \quad (4.30)$$

and the reference field $E_r(\mathbf{r}, t)$

$$E_r(\mathbf{r}, t) = \alpha_r E_0(\mathbf{r}, t), \quad (4.31)$$

at the beam splitter. The coefficients α_r and α_s correspond to the fractions of the field split into the reference and the sample beam respectively. Assuming that there is no absorption by the beam splitter (free-space optics configuration) or the fiber

coupler (fiber optics configuration), $|\alpha_s|^2 + |\alpha_r|^2 = 1$. The reference and the sample field will then propagate along different paths and finally recombine:

$$E_t(\mathbf{r}, t) = E_r(\mathbf{r}, t) + E_s(\mathbf{r}, t), \quad (4.32)$$

where $E_t(\mathbf{r}, t)$ is the total field at the mixing plane. For simplicity, dispersion and chromatic effects are ignored in this analysis, and the fields are treated as scalar fields. A more rigorous discussion will demand the full treatment of the vector field, especially due to the fact that scattering in the random medium will depolarize the sample field. However, in order to focus on the relationship between detectability and the sample randomness, the depolarization effect will be ignored in this analysis. The following sections will discuss the propagation of the sample and reference fields in a free-space optic configuration.

Sample field

After leaving the beam splitter, the sample field travels a distance l_1 before it hits a thin lens which is at a distance l_2 away from the sample surface (see figure 4.1). The field propagating toward the lens from the beam splitter is assumed to be collimated with a beam width w_0 . The lens is assumed to be an ideal thin lens with focal length f_1 and radius a_1 . The field is then focused down to a spot with beam waist w_{0s} at the focal plane inside the sample.

The incident field will experience scattering inside the sample due to refractive index fluctuations. Because of the coherence gating and the heterodyne detection scheme of OCT, only the field that is singly scattered and propagates in the backward direction after scattering will interfere constructively with the reference field and exhibit significant contribution to the interferometric optical power. The deeper the field travels in the sample, the higher the probability that the field will experience multiple scattering. In the spirit of the ‘first-order multiple scattering’ approach described in Chapter 3, the field that has not suffered any scattering at a particular

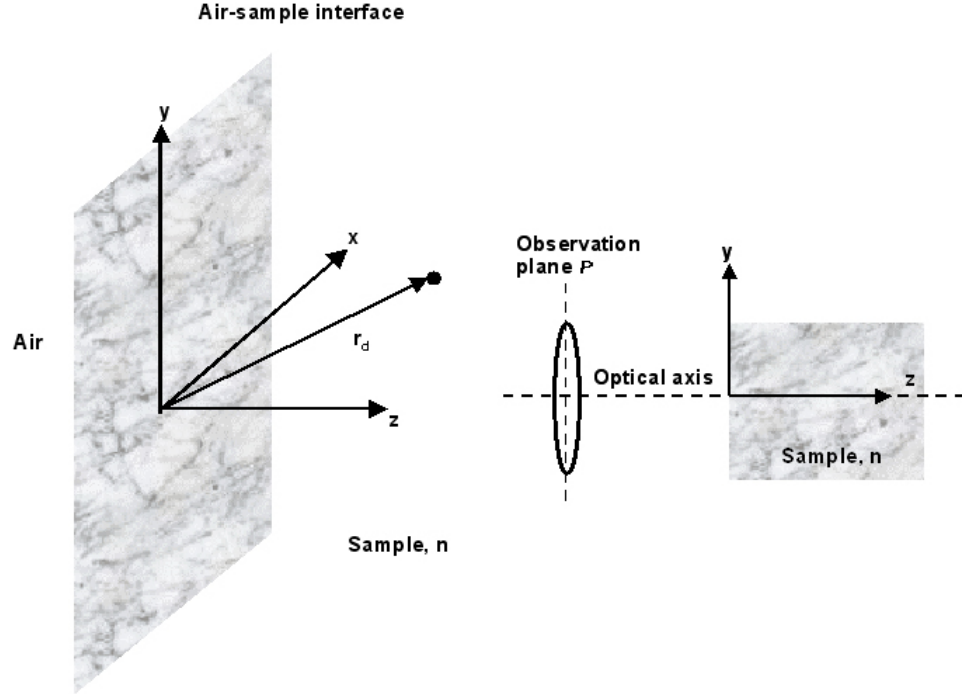


FIGURE 4.4. Illustration of \mathbf{r}_d and the reference plane for the mixing of the sample and reference beams.

scattering site at the location \mathbf{r}_d inside the sample is described as

$$E(\mathbf{r}_d, t) = \exp\left(-\frac{\mu}{2}z_d\right)E_{sf}(\mathbf{r}_d, t). \quad (4.33)$$

The position vector $\mathbf{r}_d = (z_d, \boldsymbol{\rho}_d)$ has its origin at the intersection of the optical axis and the sample-air interface (see figure 4.4). The factor $\exp(-\frac{\mu}{2}z_d)$ describes the attenuation due to absorption and scattering within the random medium. In general, $\mu = \mu_s + \mu_a$, with μ_s the scattering coefficient and μ_a the absorption coefficient. For most biological tissue, the absorption at near infrared wavelength used in the OCT can be ignored. The quantity $E_{sf}(\mathbf{r}_d, t)$ corresponds to the field strength at the scattering site as if the field is propagating in a medium that is free of scattering and absorption. Similar to eq. (4.20), $E_{sf}(\mathbf{r}_d, t)$ can be written as

$$E_{sf}(\mathbf{r}_d, t) = U_s(\mathbf{r}_d, t)T(t'_{s,d}), \quad (4.34)$$

where $t'_{s,d}$ is the corresponding retarded time from the source to the scattering site. The geometric distance from the source to the scattering site can be written as

$$l_d = l_0 + l_1 + l_2 + z_d. \quad (4.35)$$

However, since light travels slower in the sample, the retarded time is evaluated as

$$t'_{s,d} = t - \frac{l_0 + l_1 + l_2}{c} - \frac{\bar{n}z_d}{c}, \quad (4.36)$$

where \bar{n} is the average refractivity of the sample. The non-fluctuating Gaussian beam ($U_s(\mathbf{r}_d, t)$) in the sample can be written as:

$$\begin{aligned} U_s(\mathbf{r}_d, t) = & \alpha_s \mathcal{A}_s \frac{w_{0s}}{w_s(l_d, t)} \exp\left(-\frac{\rho_d^2}{w_s^2(l_d, t)}\right) \exp[i(k_0(l_0 + l_1 + l_2) - \omega_0 t)] \\ & \exp(ikz_d) \exp\left[i\left(\frac{k\rho_d^2}{2R_s(l_d, t)} - \phi(l_d, t)\right)\right], \end{aligned} \quad (4.37)$$

where $k = nk_0$ is the wave number inside the sample. The amplitude of the Gaussian beam has changed to be \mathcal{A}_s since now the sample beam is focused down to a beam waist of w_{0s} . If we assume that the optical power carried by the beam remains the same before and after focusing, then \mathcal{A}_s relates to the amplitude of the source field (\mathcal{A}_0) through the following equation:

$$|\mathcal{A}_s|^2 w_{0s}^2 = |\mathcal{A}_0|^2 w_0^2. \quad (4.38)$$

In this analysis, we assume a dynamic focusing scheme. For simplicity, we will assume that the position of the lens is static while the focal length of the lens is changed dynamically so that the focal plane inside the sample will be in sync with the movement of the axial scanning which is controlled by the motion of the reference mirror. At the beginning of the scan, the focal length of the focusing lens is $f_1(t = 0) = l_2$, so that the focal plane of the focusing lens is on the sample surface. The focal length of the lens will increase in the course of scanning so that the focal plane will coincide with the scanning depth and can be described as

$$f_1(t) = l_2 + z_{fp}, \quad (4.39)$$

where

$$z_{fp} = \frac{v_a t}{\bar{n}} \quad (4.40)$$

is the location of the focal plane, with v_a the scanning speed of the reference mirror. Due to the fact that light travels slower in the sample, the change in the location of the focal plane is $\frac{v_a t}{\bar{n}}$ instead of $v_a t$, which is the distance traveled by the reference mirror in free space. In eq. (4.37), the beam width $w_s(l_d, t)$ and the wavefront curvature $R_s(l_d, t)$ of the sample beam are functions of time due to the fact that the focal plane of the sample beam (i.e., the beam waist) is moving in the dynamic focusing scheme. The beam width $w_s(l_d, t)$ can be written in terms of z_{d1} (the location of the scattering site) as

$$w^2(z_{d1}, t) = w_{0s}^2 \left(1 + \left(\frac{\Delta_z(z_{d1}, t)}{z_{0s}} \right)^2 \right), \quad (4.41)$$

where $\Delta_z(z_{d1}, t)$ is the axial distance from the scattering site (z_{d1}) to the location of the focal plane measured from the air-sample interface (z_{fp}):

$$\Delta_z(z_{d1}, t) = z_{d1} - \frac{v_a t}{\bar{n}}.$$

The quantity z_{0s} in eq. (4.41) is the Rayleigh length for the focused sample beam, and is related to the Rayleigh length of the incident beam z_0 as shown below:

$$z_{0s} z_0 = \bar{n} f(t)^2 \approx \bar{n} f_1^2,$$

where $f(t)$ is the focal length of the focusing lens at time t , and f_1 the focal length of the lens at the beginning of the imaging process, i.e., $t = 0$. Usually, the lens is set to focus on the air-sample interface at $t = 0$ and move into the sample in synchronization with the scanning depth set by the reference mirror. In a typical OCT imaging setting, the imaging depth usually will not exceed the range of several millimeters underneath the air-sample interface. In this analysis, we will assume that f_1 is large and that the change in $f(t)$ due to dynamic focusing can be ignored for the calculation of the Rayleigh length inside the sample. Therefore, we will

approximate the time varying focal length by f_1 , which is the focal length of the lens at the beginning of the imaging process, and also the distance between the lens and the air-sample interface.

Using the first order multiple scattering approximation (see Chapter 3), the scattered field can be written as

$$E_{sc}(\mathbf{r}, t) = -\frac{1}{4\pi} \int d\mathbf{r}' \frac{1}{|\mathbf{r} - \mathbf{r}'|} \mathcal{V}(\mathbf{r}') E(\mathbf{r}', t - \frac{|\mathbf{r} - \mathbf{r}'|}{v}) \exp(-\frac{\gamma'}{2}). \quad (4.42)$$

- $E_{sc}(\mathbf{r}, t)$ is the scattered field observed at location $\mathbf{r} = (z, \boldsymbol{\rho})$. In this analysis, the exit plane of the focus lens is chosen as the observation plane (plane \mathcal{P}) for the backscattered field (see figure 4.4).
- $\mathcal{V}(\mathbf{r}) = -k^2 \left(\frac{\varepsilon(\mathbf{r}) - \bar{\varepsilon}(\mathbf{r})}{\bar{\varepsilon}(\mathbf{r})} \right)$ is the scattering potential as defined in Chapter 3. In a 2D imaging setting, axial and transverse scans are implemented. The effect of the transverse scan is mathematically described by moving the sample an amount of $\boldsymbol{\rho}_b = v_t t \hat{l}$ (i.e., replacing $\mathcal{V}(\mathbf{r}_d)$ by $\mathcal{V}(\mathbf{r}_d + \boldsymbol{\rho}_b)$), where v_t is the transverse scan speed, and \hat{l} the scan direction, which is assumed to be parallel to the y -axis of the coordinate system.
- $\frac{-1}{4\pi} \frac{1}{|\mathbf{r} - \mathbf{r}'|}$ is the three dimensional Green's function.
- $E(\mathbf{r}', t - \frac{|\mathbf{r} - \mathbf{r}'|}{v})$ is the field strength at the scattering site given by eq. (4.33), with $t - \frac{|\mathbf{r} - \mathbf{r}'|}{v}$ the retarded time from the scattering site to the observation point. The velocity v will take on values of c (light speed in free space) or $\frac{c}{n}$ (propagation speed in a medium with refractivity n) according to whether the field is propagating in free space or in the sample. The factor $\exp(-\frac{\gamma'}{2})$ corresponds to the attenuation on the field due to absorption and/or scattering upon propagation from the scattering site to the observation plane.

Although physically the mixing between the reference and the scattered field will happen at the detector, in this analysis, they will be mixed at a observation plane

(\mathcal{P}) to simplify the mathematics. The observation plane (\mathcal{P}) in the sample arm is chosen to be the exit plane of the focusing lens in the return path, which is assumed to be conjugate to the detector entrance plane with respect to the detector lens (see figure 4.1). Using eqs. (3.12, 4.34, and 4.42), the sample field on the observation plane (\mathcal{P}) just at the left of the focusing lens can be written as the product of the transmittance function of the lens ($t_1(\boldsymbol{\rho})$) and the scattered field ($E_{sc}(\mathbf{r}, t)$, see eq. (4.42)):

$$E_{s,\mathcal{P}}(\boldsymbol{\rho}, t) = t_1(\boldsymbol{\rho})E_{sc}(\mathbf{r}, t), \quad (4.43)$$

where $t_{l1}(\boldsymbol{\rho})$ is the transmittance function of the focusing lens (lens 1) in front of the sample,

$$t_1(\boldsymbol{\rho}) = \exp(-i\frac{k_0\boldsymbol{\rho}^2}{2f_1} - ik_0f_1)cyl(\frac{\boldsymbol{\rho}}{2a_1}). \quad (4.44)$$

Using eq. (4.33) for the field at the scattering site ($E(\mathbf{r}', t - \frac{|\mathbf{r}-\mathbf{r}'|}{v})$), then eq. (4.43) can be written as

$$E_{s,\mathcal{P}}(\boldsymbol{\rho}, t) = t_1(\boldsymbol{\rho})\left(-\frac{1}{4\pi}\right) \int d\mathbf{r}_d \frac{1}{|\mathbf{r}-\mathbf{r}_d|} \exp(-\mu_s z_d) E_{sf}(\mathbf{r}_d, t - \frac{|\mathbf{r}-\mathbf{r}_d|}{v}) \mathcal{V}(\mathbf{r}_d + \boldsymbol{\rho}_b). \quad (4.45)$$

The factor $\exp(-\mu_s z_d)$ in eq. (4.45) corresponds to the attenuation to the field due to scattering or absorption from the random media. Since the field passes through the medium twice – first in the forward direction toward the sample, then in the backward direction toward the detector from the sample, $\exp(-\mu_s z_d)$ is used instead of $\exp(-\frac{1}{2}\mu_s z_d)$. Using eq. (4.34), eq. (4.45) can be written as

$$\begin{aligned} & E_{s,\mathcal{P}}(\boldsymbol{\rho}, t) \\ &= t_1(\boldsymbol{\rho})\left(-\frac{1}{4\pi}\right) \int d\mathbf{r}_d \frac{\exp(ik_0|\mathbf{r}-\mathbf{r}_d|)}{|\mathbf{r}-\mathbf{r}_d|} \exp(-\mu_s z_d) U_s(\mathbf{r}_d, t) T(t'_{s,\mathcal{P}}) \mathcal{V}(\mathbf{r}_d + \boldsymbol{\rho}_b) \\ &\equiv \int d\mathbf{r}_d \mathcal{U}_{s,\mathcal{P}}(\boldsymbol{\rho}, \mathbf{r}_d; t) \mathcal{V}(\mathbf{r}_d + \boldsymbol{\rho}_b) T(t'_{s,\mathcal{P}}), \end{aligned} \quad (4.46)$$

where

$$\mathcal{U}_{s,\mathcal{P}}(\boldsymbol{\rho}, \mathbf{r}_d; t) = t_{l1}(\boldsymbol{\rho})\left(-\frac{1}{4\pi}\right) \frac{\exp(ik_0|\mathbf{r}-\mathbf{r}_d|)}{|\mathbf{r}-\mathbf{r}_d|} \exp(-\mu_s z_d) U_s(\mathbf{r}_d, t). \quad (4.47)$$

In eq. (4.46), there are three components in the expression of the scattered field. The first part $\mathcal{U}_{s,\mathcal{P}}(\boldsymbol{\rho}, \mathbf{r}_d; t)$ corresponds to the non-fluctuating quantities in the scattered field. The second part $\mathcal{V}(\mathbf{r}_d + \boldsymbol{\rho}_b)$ is the scattering potential of the random medium describing the index fluctuation in the sample. The third component $T(t'_{s,\mathcal{P}})$ corresponds to the temporal fluctuation of the source at the retarded time from the source to the observation plane: $t'_{s,\mathcal{P}} = t - \tau_{s,\mathcal{P}}$, with $\tau_{s,\mathcal{P}} = (l_0 + l_1 + 2l_2)/c + 2nz_d/c$.

To simplify eq. (4.47), we will approximate the distance in the denominator as $|\mathbf{r} - \mathbf{r}_d| \approx l_2$. Using eq. (4.39), we can rewrite

$$|\mathbf{r} - \mathbf{r}_d| \approx l_2 = f_1(0) \equiv f_1. \quad (4.48)$$

For the phase term $\exp(ik_0|\mathbf{r} - \mathbf{r}_d|)$, we will employ Fresnel approximation

$$\exp(ik_0|\mathbf{r} - \mathbf{r}_d|) \approx \exp(ik_0(l_2 + nz_d)) \exp(ik_0 \frac{(\boldsymbol{\rho} - \boldsymbol{\rho}_d)^2}{2l_2}). \quad (4.49)$$

Assume that far-field approximation is applicable, i.e., the distance from the random medium to the observation plane (l_2) is much larger than the transverse dimension of the scattering volume ($|\boldsymbol{\rho}_d|$). Then the corresponding quadratic phase term can be approximated as one:

$$\exp(ik_0 \frac{\boldsymbol{\rho}_d^2}{2l_2}) \approx 1,$$

and eq. (4.49) can be written as

$$\exp(ik_0|\mathbf{r} - \mathbf{r}_d|) \approx \exp(ik_0(l_2 + nz_d)) \exp(ik_0(\frac{|\boldsymbol{\rho}|^2}{2l_2} - \frac{\boldsymbol{\rho} \cdot \boldsymbol{\rho}_d}{l_2})). \quad (4.50)$$

Substituting eqs. (4.48 and 4.50) into eq. (4.47), then $\mathcal{U}_{s,\mathcal{P}}(\boldsymbol{\rho}, \mathbf{r}_d; t)$ can be written as

$$\begin{aligned} \mathcal{U}_{s,\mathcal{P}}(\boldsymbol{\rho}, \mathbf{r}_d; t) &= -\frac{1}{4\pi f_1} t_{l1}(\boldsymbol{\rho}) \exp(ik_0(l_2 + nz_d)) \exp(ik_0(\frac{|\boldsymbol{\rho}|^2}{2f_1} - \frac{\boldsymbol{\rho} \cdot \boldsymbol{\rho}_d}{f_1})) \\ &\quad \exp(-\mu_s z_d) U_s(\mathbf{r}_d, t). \end{aligned} \quad (4.51)$$

Using eqs. (4.51 and 4.45), the sample field observed on the plane \mathcal{P} can be written

as

$$\begin{aligned}
E_{s,\mathcal{P}}(\boldsymbol{\rho}, t) &= \text{cyl}\left(\frac{\boldsymbol{\rho}}{2a_1}\right)\left(-\frac{1}{4\pi f_1}\right)\alpha_s \mathcal{A}_s w_{0s} \exp(ik_0(l_0 + l_1 + l_2) - i\omega_0 t) \\
&\int d\mathbf{r}_d \exp(i2nk_0 z_d - i\phi(l_d)) \exp(-ik_0 \frac{\boldsymbol{\rho} \cdot \boldsymbol{\rho}_d}{l_2}) \exp(-\mu_s z_d) \\
&\frac{1}{w_s(l_d, t)} \exp\left(-\frac{\rho_d^2}{w_s^2(l_d, t)}\right) \exp\left(i\frac{k\rho_d^2}{2R_s(l_d, t)}\right) \mathcal{V}(\mathbf{r}_d + \boldsymbol{\rho}_b) T(t'_{s,\mathcal{P}}).
\end{aligned} \tag{4.52}$$

This expression will be used for the evaluation of the optical power later in the following sections.

Reference Field

In the reference arm, the field is assumed to be collimated, which means that it is treated as a field with flat wavefront and constant beam width w_0 throughout the propagation. That is, the q -parameter of the reference field can be written as, $\frac{1}{q_r(z)} = i\frac{\lambda}{\pi w_0^2}$. For this assumption to be valid, it is necessary that the Rayleigh length of the source field (z_0) is much larger than the propagation distance. This condition usually can be easily satisfied.

Upon leaving the beam splitter, the reference field will propagate for a distance before it hits the reference mirror that scans at a velocity v_a (see figure 4.1). It is assumed that it is a perfect mirror, and no absorption or phase change occurs upon the reflection. Physically, the field is reflected back toward the beam splitter, and mixed with the back scattered or back reflected sample field at the detector plane. However, as discussed in the previous section, mathematically, the mixing happens on a reference plane that is conjugate to the detector plane with respect to the lens 2 in figure 4.1. In the reference arm, this reference plane is placed at a distance of l_2 away from the reference mirror at time $t = 0$ (see figure 4.1). Similar to eq. (4.20), the reference field on the observation plane \mathcal{P} can be written as

$$E_{r,\mathcal{P}}(\boldsymbol{\rho}, t) = U_{r,\mathcal{P}}(\boldsymbol{\rho}, t) T(t'_{r,\mathcal{P}}), \tag{4.53}$$

where $t'_{r,\mathcal{P}}$ is the retarded time from the source to the observation plane. It can be written as

$$t'_{r,\mathcal{P}} = t - \frac{l_r}{c}, \quad (4.54)$$

with

$$l_r = l_0 + l_1 + 2l_2 + 2v_a t, \quad (4.55)$$

the physical optical path from the source to the observation plane \mathcal{P} in the reference arm. The non-fluctuating component of the reference field $U_{r,\mathcal{P}}(\boldsymbol{\rho}, t)$ is a Gaussian beam as shown below:

$$\begin{aligned} U_{r,\mathcal{P}}(\boldsymbol{\rho}, t) = & \alpha_r \mathcal{A}_0 \frac{w_0}{w(l_r)} \exp[i(k_0 l_{r0} - \omega' t)] \\ & \exp\left(-\frac{\rho^2}{w^2(l_r)}\right) \exp\left[i\left(\frac{k_0 \rho^2}{2R(l_r)} - \phi(l_r)\right)\right], \end{aligned} \quad (4.56)$$

where α_r describes the fraction of the source field being split into the reference arm. Due to the motion of the reference mirror, the angular frequency of the reference beam is modified to be

$$\omega' = \omega_0 \left(1 - \frac{2v_a}{c}\right) = \omega_0 - \omega_D, \quad (4.57)$$

where

$$\omega_D = \omega_0 \frac{2v_a}{c} \quad (4.58)$$

is the change in the angular frequency of the reference beam due to the Doppler effect. The phase term $\phi(l_r)$ represents the Guoy phase of the reference beam. It is assumed that $\phi(l_r) \approx \pi$ throughout the propagation. Notice that in eq. (4.56), instead of using the physical optical path l_r as described in eq. (4.55), we have introduced a notation l_{r0} in the plane wave term ($\exp[i(k_0 l_{r0} - \omega' t)]$) to describe the phase. The quantity l_{r0} is the optical path from the source to the observation plane at $t = 0$, i.e.,

$$l_{r0} = l_0 + l_1 + 2l_2. \quad (4.59)$$

The reason for making this replacement is that the phase change due to the movement of the reference mirror has already been taken into account by considering the Doppler

effect on the frequency modulation of the reference beam. As discussed in ref. [73], Malacara pointed out that the fringe movement in an interferometer with a moving mirror was solely accounted for by the Doppler effect to the frequency of the moving beam. As we have modified the frequency from ω_0 to ω' in eq. (4.56), the effect of the change in the optical path due to the mirror movement on the optical phase of the plane wave term should be left out to avoid counting the phase change twice.

4.2.3 Heterodyne Detection and Optical Power

In heterodyne detection, the input signal is mixed with a local oscillator for detection. In OCT, the reference field serves as the local oscillator and is mixed with the backscattered field in the sample arm. The total optical intensity on the observation plane will be the sum of the intensities carried by the individual beam and the corresponding interferometric term between the two beams:

$$\begin{aligned} I(\boldsymbol{\rho}, t) &= |E_{r,\mathcal{P}}(\boldsymbol{\rho}, t) + E_{s,\mathcal{P}}(\boldsymbol{\rho}, t)|^2 \\ &= I_{DC}(\boldsymbol{\rho}, t) + I_{int}(\boldsymbol{\rho}, t), \end{aligned} \quad (4.60)$$

where $I_{DC}(\boldsymbol{\rho}, t)$ corresponds to the DC component of the optical intensity,

$$I_{DC}(\boldsymbol{\rho}, t) = |E_{r,\mathcal{P}}(\boldsymbol{\rho}, t)|^2 + |E_{s,\mathcal{P}}(\boldsymbol{\rho}, t)|^2, \quad (4.61)$$

and $I_{int}(\boldsymbol{\rho}, t)$ is the interferometric term of the optical intensity,

$$\begin{aligned} I_{int}(\boldsymbol{\rho}, t) &= 2 \operatorname{Re}[E_{r,\mathcal{P}}^*(\vec{\rho}, t)E_{s,\mathcal{P}}(\vec{\rho}, t)] \\ &= I_{rs}(\boldsymbol{\rho}, t) + I_{rs}^*(\boldsymbol{\rho}, t), \end{aligned} \quad (4.62)$$

with $I_{rs}(\boldsymbol{\rho}, t) = E_{r,\mathcal{P}}^*(\vec{\rho}, t)E_{s,\mathcal{P}}(\vec{\rho}, t)$ the complex interferometric intensity.

The corresponding optical power can be written as

$$P(t) = P_{DC}(t) + P_{int}(t), \quad (4.63)$$

where $P_{DC}(t)$ is referred to as the DC term of the optical power, and $P_{int}(t)$ the interferometric term.

Optical power – DC term

The DC optical power consists of two terms, i.e., the contributions from the reference and the sample beams:

$$\begin{aligned} P_{DC}(t) &= P_r(t) + P_s(t) \\ &= \int d\boldsymbol{\rho} (|E_{r,\mathcal{P}}(\boldsymbol{\rho}, t)|^2 + |E_{s,\mathcal{P}}(\boldsymbol{\rho}, t)|^2). \end{aligned} \quad (4.64)$$

Using eqs. (4.53 and 4.56), and letting $w(l_r) = w_0$ for the reference field, $|E_{r,\mathcal{P}}(\boldsymbol{\rho}, t)|^2$ can be written as

$$|E_{r,\mathcal{P}}(\boldsymbol{\rho}, t)|^2 = |\alpha_r \mathcal{A}_0|^2 \exp\left(-\frac{2\rho^2}{w_0^2}\right) T^*(t'_{r,\mathcal{P}}) T(t'_{r,\mathcal{P}}). \quad (4.65)$$

When averaged over the field fluctuation, the optical power from the reference beam can be evaluated as

$$\langle P_r(t) \rangle_{F=} = \int d\boldsymbol{\rho} \langle |E_{r,\mathcal{P}}(\boldsymbol{\rho}, t)|^2 \rangle_{F=} = |\alpha_r|^2 I_0 \frac{\pi w_0^2}{2} = |\alpha_r|^2 P_0, \quad (4.66)$$

where $P_0 = I_0 \frac{\pi w_0^2}{2}$ the optical power of the source field, with $I_0 = |\mathcal{A}_0|^2$ the intensity.

The DC optical power from the sample beam is $P_s(t) = \int d\boldsymbol{\rho} |E_{s,\mathcal{P}}(\boldsymbol{\rho}, t)|^2$. Using eq. (4.46), the averaged optical power from the sample beam can be written as

$$\begin{aligned} \langle P_s(t) \rangle_{F,M=} &= \int d\boldsymbol{\rho} \int d\mathbf{r}_{d1} \int d\mathbf{r}_{d2} \mathcal{U}_{s,\mathcal{P}}(\boldsymbol{\rho}, \mathbf{r}_{d1}; t) \mathcal{U}_{s,\mathcal{P}}^*(\boldsymbol{\rho}, \mathbf{r}_{d2}; t) \\ &\langle T(t'_{s,\mathcal{P}1}) T^*(t'_{s,\mathcal{P}2}) \rangle_{F=} \langle \mathcal{V}(\mathbf{r}_{d1} + \boldsymbol{\rho}_{bt}) \mathcal{V}(\mathbf{r}_{d2} + \boldsymbol{\rho}_{bt}) \rangle_{M=}. \end{aligned} \quad (4.67)$$

In eq. (4.67), the fluctuations in the radiation field, described by the magnitude of the degree of temporal coherence of the field $\langle T(t'_{s,\mathcal{P}1}) T^*(t'_{s,\mathcal{P}2}) \rangle_{F=}$, is decoupled from the index fluctuations in the sample, described by the spatial correlation of the scattering potential $\langle \mathcal{V}(\mathbf{r}_{d1} + \boldsymbol{\rho}_{bt}) \mathcal{V}(\mathbf{r}_{d2} + \boldsymbol{\rho}_{bt}) \rangle_{M=}$.

Optical power – interferometric term

The optical power for the interferometric term can be written as

$$P_{int}(t) = \int d\boldsymbol{\rho} I_{int}(\boldsymbol{\rho}, t) = \int d\boldsymbol{\rho} (I_{rs}(\boldsymbol{\rho}, t) + I_{rs}^*(\boldsymbol{\rho}, t)) = P_{rs}(t) + P_{rs}^*(t), \quad (4.68)$$

where

$$P_{rs}(t) = \int d\boldsymbol{\rho} I_{rs}(\boldsymbol{\rho}, t) = \int d\boldsymbol{\rho} E_{r,\mathcal{P}}^*(\vec{\rho}, t) E_{s,\mathcal{P}}(\vec{\rho}, t)$$

is the complex interferometric optical power. Using eqs. (4.53 and 4.46), the complex power can be written as

$$P_{rs}(t) = \int_{\infty} d\boldsymbol{\rho} \int d\mathbf{r}_d T(t'_{s,\mathcal{P}}) T^*(t'_{r,\mathcal{P}}) \mathcal{U}_{s,\mathcal{P}}(\boldsymbol{\rho}, \mathbf{r}_d; t) \mathcal{V}(\mathbf{r}_d + \boldsymbol{\rho}_b) U_{r,\mathcal{P}}^*(\boldsymbol{\rho}, t). \quad (4.69)$$

When averaged over the source fluctuation, $P_{rs,F}(t)$ can be written as,

$$\begin{aligned} \langle P_{rs}(t) \rangle_F = & \int d\boldsymbol{\rho} \int d\mathbf{r}_d \langle T(t'_{s,\mathcal{D}}) T^*(t'_{r,\mathcal{D}}) \rangle_F \\ & \mathcal{U}_{s,\mathcal{P}}(\boldsymbol{\rho}, \mathbf{r}_d; t) \mathcal{V}(\mathbf{r}_d + \boldsymbol{\rho}_b) U_{r,\mathcal{P}}^*(\boldsymbol{\rho}, t), \end{aligned} \quad (4.70)$$

where $\mathcal{U}_{s,\mathcal{P}}(\boldsymbol{\rho}, \mathbf{r}_d; t)$ and $U_{r,\mathcal{P}}^*(\boldsymbol{\rho}, t)$ correspond to the non-fluctuating components in the sample field (see eq. (4.46)) and the reference field (see eq. (4.53)) respectively.

4.2.4 Data Acquisition

We have discussed the optics of an OCT system in the previous sections. The chain of events happening during the data acquisition process is key to presenting the detected optical signal in the digital form for further study, and will be discussed here. A good review article on the topic of data acquisition in OCT can be found in ref. [74].

Figure 4.5 shows the basic data acquisition electronics in an OCT system. The first component after the PIN detector is a transimpedance amplifier, which is usually embedded in the photo detector converting the incoming photocurrent signal to a voltage signal (In this analysis, we will ignore the current-voltage conversion and deal with the photocurrent directly. In essence, we have ignored the effect of the transimpedance amplifier). The output from the PIN detector consists of two terms: an almost DC term corresponding to the optical power originating from the sample and reference beams respectively, and an interferometric term resulting from the interference between the reference and the sample beams. The interferometric

term is oscillating at a modulation frequency determined by the Doppler shift and/or any external modulation applied to the system. In this analysis, it is assumed that no external modulation is applied. A band-pass filter is then used to extract the interferometric term. Usually, the band-pass filter is centered around the modulation frequency and its bandwidth is proportional to the bandwidth of the broadband source. The filtered signal is then sent into a demodulator as shown in the dashed box in figure 4.5 for demodulation of the oscillating interferometric term. Demodulation can be achieved by different schemes such as mixing, square-law detection, and logarithmic detection [75]. In the mixing scheme, the input oscillating signal is multiplied with a local oscillating reference signal of the correct phase followed by low-pass filtering. The square-law detection and the logarithmic detection fall into the category of envelope detection method in which the input signal is rectified followed by low-pass filtering. Single chip implementation for demodulation has been developed for compact OCT imaging modules [76]. In this work, we will present an analysis based on the mixing scheme.

Let $P(t)$ be the total optical power at the detector, and $s(t)$ the output at the demodulator, which will be referred to as the demodulated OCT data. The data stream $s(t)$ is a stochastic process driven by multiple sources of randomness, including the randomness of the imaging process (assumed to be Poisson), the source fluctuation (assumed to be Gaussian), and the sample randomness (described by the scattering potential), among the other sources of randomness. In the following sections, a relationship between $s(t)$ and $P(t)$ based on the mixing demodulation will be derived.

Detector Front-End

The detector front-end consists of a photodetector and a band-pass filter. A PIN (p-i-n, positive-intrinsic-negative) photodetector is used to convert the incoming optical power into photocurrent output. The interferometric component of the optical power is extracted by the band-pass filter for further processing. Let $h_d(t)$ repre-

sents the detector response function, and $h_b(t)$ the band-pass filter response function. Assuming shift-invariant system, the front-end response function $h_f(t)$ then can be written as the convolution of the detector response and the band-pass filter response functions:

$$h_f(t) = h_d(t) \otimes h_b(t). \quad (4.71)$$

Then the output current at the front-end, when averaged over the detector noise, which is assumed to be Poisson statistics, can be written as:

$$\langle i(t) \rangle_P = \frac{\varsigma e}{h\nu_0} P(t) \otimes h_f(t) = \mathfrak{R} P(t) \otimes h_f(t), \quad (4.72)$$

where $\langle \dots \rangle_P$ represents averaging over the Poisson statistics. The quantity $\mathfrak{R} = \frac{\varsigma e}{h\nu_0}$, with units of *Amp/Watt*, is the responsivity of the detector, where ς is the quantum efficiency of the detector (probability of a photon being converted into a charge carrier in the detector). The function $h_f(t)$ is the corresponding front-end response function and integrates to a unit area.

For a PIN photodetector, the response time is usually less than a nanosecond (*ns*). On the other hand, the band-pass filter at the front-end usually has a wider bandwidth (Δ_{fb}) so that it can capture fully the spectrum spanned by the source, and is proportional to the source bandwidth ΔS (see eq. (4.29)) as [74]:

$$\Delta_{fb} = \frac{2v_a}{c} \Delta S = \sqrt{\frac{\pi}{2 \ln 2}} \frac{2v_a}{c} \Delta \nu. \quad (4.73)$$

The central frequency of the band-pass filter is set at the modulation frequency. In the situation when there is no external modulation, the modulation frequency corresponds to the Doppler shift relating to the movement of the reference mirror:

$$f_m = f_D = \frac{2v_a}{c} \nu_0. \quad (4.74)$$

For example, in a certain imaging setting, the central wavelength of the source (λ_0) is about $1\mu m$, and the source bandwidth (Δ_λ) is about $20nm$. For a total imaging depth $d \sim 3mm$, and a reference mirror scanning rate of $\nu_s \sim 100Hz$, the scanning

velocity is $v_a = \nu_s d \approx 0.3ms^{-1}$. Using eq. (4.73), the bandwidth of the band-pass filter can be approximated as $\Delta_{fb} \approx 18KHz$, corresponding to a response time of $55\mu s$. Since the response time of the band-pass filter is much longer than that of the PIN photodetector, we can approximate the detector response $h_d(t)$ in eq. (4.71) as a delta function. Then the front-end response $h_f(t)$ can be approximated as (see eq. (4.71))

$$h_f(t) \approx h_b(t). \quad (4.75)$$

Substituting this result into eq. (4.72), then the averaged output current at the front-end can be written as

$$\langle i(t) \rangle_p = \Re P(t) \otimes h_b(t). \quad (4.76)$$

Demodulation

The front-end output $i(t)$ is sent into a demodulator to extract information about the oscillating interferometric term. As discussed before, there are different schemes available for demodulation. In this analysis, only the mixing scheme will be demonstrated.

The mixer scheme operates basically on the same principle as lock-in detection, or the coherent detection as phrased in the communication community. The input signal is first multiplied with a sinusoidal signal oscillating at the same modulation frequency of the input, and then filtered by a low pass filter to extract the slow varying amplitude of the input signal. Let $r(t)$ be the reference signal. It is assumed that $r(t)$ is in phase with the front-end output $i(t)$, and let $h_l(t)$ be the response function of the low-pass filter. The output of the demodulator $s(t)$ can then be written as

$$\begin{aligned} s(t) &= (i(t)r(t)) \otimes h_l(t) \\ &= \int dt' i(t')r(t')h_l(t-t'). \end{aligned} \quad (4.77)$$

Therefore, when averaged over the Poisson noise of the imaging system, using eq.

((4.76) and (4.77)), the averaged output at the demodulator can be written as

$$s_P(t) = \langle s(t) \rangle_P = [(\Re P(t) \otimes h_f(t))r(t)] \otimes h_l(t). \quad (4.78)$$

Fourier Domain Analysis for the Response Functions

In this section, we will simplify the expression of eq. (4.78) by performing a Fourier analysis. Switching to the Fourier domain, and using eq. (4.78), the spectrum of the demodulated data can be written as

$$\begin{aligned} \tilde{s}_P(f) &= \Re \mathcal{F}\{(P(t) \otimes h_f(t))r(t)\} \tilde{h}_l(f) \\ &= \Re((\tilde{P}(f) \tilde{h}_f(f)) \otimes \tilde{r}(f)) \tilde{h}_l(f). \end{aligned} \quad (4.79)$$

For simplicity, it is assumed that the reference signal $r(t)$ is a sinusoidal function with frequency f_m , where f_m is the modulation frequency of the OCT system. Therefore, the Fourier transform of $r(t)$ can be written as

$$\tilde{r}(f) = \frac{1}{2}(\delta(f + f_m) + \delta(f - f_m)). \quad (4.80)$$

Then eq. (4.79) can be written as

$$\tilde{s}_P(f) = \frac{\Re}{2} \tilde{P}(f + f_m) \tilde{h}_b(f + f_m) \tilde{h}_l(f) + \frac{\Re}{2} \tilde{P}(f - f_m) \tilde{h}_b(f - f_m) \tilde{h}_l(f). \quad (4.81)$$

Just as in the lock-in amplifier, the mixing of the input signal centered at the modulation frequency (f_m) with the reference signal will generate two terms: one oscillates at a near zero frequency (the difference-frequency term), and one oscillates at two times of the modulation frequency (the sum-frequency term). These two terms will then be fed into a low pass filter and the sum-frequency term will be removed. It is desirable for the low pass filter to have a wider frequency spectrum such that faster response is possible. However, at the same time, the frequency spectrum of the low pass filter should be narrow enough so that the higher frequency components relating to the sum-frequency term will be rejected more completely. A convenient choice is

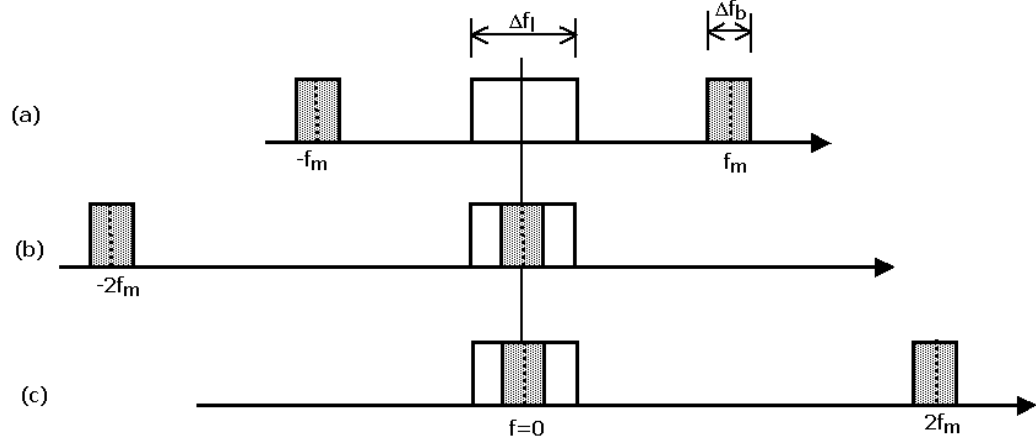


FIGURE 4.5. Illustration of the band-pass (shaded rectangles) and the low-pass filters. (a) The band-pass filter has its spectrums centered around f_m and $-f_m$. (b) The band-pass filter is shifted by an amount of $-f_m$. (c) The band-pass filter is shifted by an amount of f_m .

to set the cutoff frequency for the low pass filter as half of the sum frequency. For a simple low pass filter, its spectrum thus can be written as [77]

$$\tilde{h}_l(f) = \text{rect}\left(\frac{f}{\Delta f_l}\right), \quad (4.82)$$

where

$$\Delta f_l = 2f_m = 2\frac{2v_a}{c}\nu_0 \quad (4.83)$$

is the cutoff frequency for the low pass filter. Similarly, for a simple band-pass filter, its spectrum $\tilde{h}_b(f)$ can be written as

$$\tilde{h}_b(f) = \text{rect}\left(\frac{f - f_m}{\Delta f_b}\right) + \text{rect}\left(\frac{f + f_m}{\Delta f_b}\right), \quad (4.84)$$

where Δf_b is the bandwidth of the band-pass filter and is given by eq. (4.73) (see figure 4.6). Using eqs. (4.82 and 4.84), the products $\tilde{h}_b(f + f_m)\tilde{h}_l(f)$ and $\tilde{h}_b(f - f_m)\tilde{h}_l(f)$ in eq. (4.81) can be written as

$$\tilde{h}_b(f + f_m)\tilde{h}_l(f) = \text{rect}\left(\frac{f}{\Delta f_b}\right)\text{rect}\left(\frac{f}{\Delta f_l}\right) + \text{rect}\left(\frac{f + 2f_m}{\Delta f_b}\right)\text{rect}\left(\frac{f}{\Delta f_l}\right), \quad (4.85)$$

and

$$\tilde{h}_b(f - f_m)\tilde{h}_i(f) = \text{rect}\left(\frac{f - 2f_m}{\Delta_{fb}}\right)\text{rect}\left(\frac{f}{\Delta_{fl}}\right) + \text{rect}\left(\frac{f}{\Delta_{fb}}\right)\text{rect}\left(\frac{f}{\Delta_{fl}}\right). \quad (4.86)$$

Using eqs. (4.83 and 4.73), it can be shown that $\Delta_{fl} > \Delta_{fb}$, and the products $\text{rect}\left(\frac{f+2f_m}{\Delta_{fb}}\right)\text{rect}\left(\frac{f}{\Delta_{fl}}\right)$ and $\text{rect}\left(\frac{f-2f_m}{\Delta_{fb}}\right)\text{rect}\left(\frac{f}{\Delta_{fl}}\right)$ in the the above equations are zero since there is no overlapping between the two *rect*-functions (see figure 4.6). Also, since the width of $\text{rect}\left(\frac{f}{\Delta_{fb}}\right)$ is narrower than that of $\text{rect}\left(\frac{f}{\Delta_{fl}}\right)$, then

$$\text{rect}\left(\frac{f}{\Delta_{fb}}\right)\text{rect}\left(\frac{f}{\Delta_{fl}}\right) = \text{rect}\left(\frac{f}{\Delta_{fb}}\right).$$

Therefore, eqs. (4.85 and 4.86) can be simplified as

$$\tilde{h}_b(f + f_m)\tilde{h}_i(f) = \text{rect}\left(\frac{f}{\Delta_{fb}}\right), \quad (4.87)$$

and

$$\tilde{h}_b(f - f_m)\tilde{h}_i(f) = \text{rect}\left(\frac{f}{\Delta_{fb}}\right). \quad (4.88)$$

Substituting these results into eq. (4.81), then $\tilde{s}_P(f)$ can be written as

$$\tilde{s}_P(f) = \frac{\Re}{2}(\tilde{P}(f + f_m) + \tilde{P}(f - f_m))\text{rect}\left(\frac{f}{\Delta_{fb}}\right).$$

When transformed back to the time domain, the averaged demodulated data can be written as

$$\begin{aligned} s_P(t) &= \Re(\cos(\omega_m t)P(t)) \otimes \frac{1}{\tau_b} \text{sinc}\left(\frac{t}{\tau_b}\right) \\ &= \int dt' \Phi(t')H(t, t'), \end{aligned} \quad (4.89)$$

with

$$\Phi(t) = \frac{P(t)}{h\nu_0}, \quad (4.90)$$

which is the photon flux corresponding to the optical power $P(t)$, and

$$H(t, t') = e\varsigma \cos(\omega_m t') \frac{1}{\tau_b} \text{sinc}\left(\frac{1}{\tau_b}(t - t')\right), \quad (4.91)$$

where $\omega_m = 2\pi f_m$, with f_m given by eq. (4.74). The quantity τ_b is the response time of the bandpass filter, and is given as (see eq. (4.73))

$$\tau_b = \frac{1}{\Delta_{fb}} = \frac{c}{2v_a} \frac{1}{\Delta\nu} \sqrt{\frac{2 \ln 2}{\pi}}. \quad (4.92)$$

The function $H(t, t')$ represents the combined response function (in the unit of current, Amp) of the front-end and the demodulator.

Shannon Wavelet and Meyer Wavelet

In the previous sections, it is assumed that the band-pass and the low pass filters (see eqs. (4.84) and (4.82)) are of ideal configurations: the pass-bands cut off sharply at the desired cutoff frequencies. However, in reality, the sharp cut-off will introduce an undesirable property of a slowly decaying impulse response in the time domain. Therefore, substantial effort has been injected into designing filters that have fast roll-offs in the frequency domain, and also a fast decaying impulse response in the time domain [78].

The filter configuration adopted in the previous sections (eq. (4.82) and eq. (4.84)) actually corresponds to a Shannon wavelet. The scaling function $\phi(t)$ of a Shannon wavelet in the time domain can be written as

$$\phi(t) = \frac{\sin(\pi t)}{\pi t} = \text{sinc}(t),$$

and, in the Fourier domain,

$$\widehat{\phi}(\omega) = \text{rect}\left(\frac{\omega}{2\pi}\right).$$

The Shannon wavelet gives a perfect sharp cut-off in the frequency domain, but a slow decaying impulse response function in the time domain. The long ripples in the impulse response function may spread through the time axis and introduce artificial overlap between events happening at time points that are far apart. This behavior is not desirable since it will introduce artificial correlation between two inherently uncorrelated events. To reduce this artificial correlation, we will use a

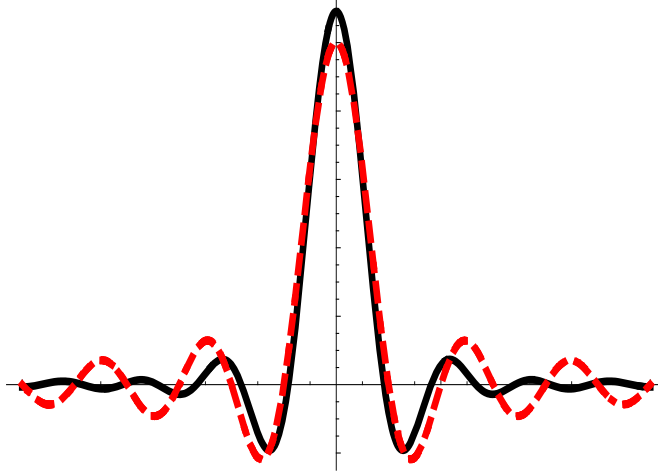


FIGURE 4.6. Comparison between the scaling function of a Shannon wavelet (dashed line) and a Meyer wavelet (solid line). The ripples in the scaling function of the Meyer wavelet die out more quickly than that of the Shannon wavelet.

Meyer wavelet in this simulation to replace the Shannon wavelet for the time domain response function of the data acquisition system (the front-end and the demodulation system).

The Meyer wavelet is similar to the Shannon wavelet, but has a smoother roll-off at the cut-off frequencies for the frequency domain scaling function, instead of a sharp discontinuity. Due to the smoothing in the frequency domain, the Meyer wavelet scaling function has a faster decay in the time domain (see figure 4.7). The scaling function of the Meyer wavelet in the frequency domain is usually described as

$$\widehat{\phi}(\omega) = \begin{cases} 1 & |\omega| \leq \frac{2\pi}{3} \\ \cos\left[\frac{\pi}{2}v\left(\frac{3}{2\pi}|\omega| - 1\right)\right] & \frac{2\pi}{3} \leq |\omega| \leq \frac{4\pi}{3} \\ 0 & \text{otherwise} \end{cases} \quad (4.93)$$

where $v(x)$ is a smooth function satisfying

$$v(x) = \begin{cases} 0 & \text{if } x \leq 0 \\ 1 & \text{if } x > 1 \end{cases}$$

and

$$v(x) + v(1 - x) = 1.$$

The scaling function for the Meyer wavelet then can be obtained through the Fourier transform of eq. (4.93). We will simply replace the response function in eq. (4.89) and eq. (4.91) with the Meyer Wavelet and rewrite the equations as

$$\begin{aligned} s_P(t) &= \Re(\cos(\omega_m t)P(t)) \otimes \psi_{Meyer}(t, t') \\ &= \int dt' \Phi(t') H_{Meyer}(t, t'), \end{aligned} \quad (4.94)$$

and

$$H_{Meyer}(t, t') = \zeta e \cos(\omega_m t') \psi_{Meyer}(t, t'), \quad (4.95)$$

where $\psi_{Meyer}(t)$ is the scaling function of the Meyer wavelet in the time domain. Eqs. ((4.94) and (4.95)) will be the foundation for the statistical analysis on the OCT data that will be discussed in the coming chapters.

Chapter 5

STATISTICAL ANALYSIS OF OCT DATA

In this chapter, we will derive an expression for the covariance function of the demodulated OCT data. First we will give a general description of the different sources of randomness in an OCT imaging modality. Then we will present a mathematical model for the random medium before we finally derive the covariance function for the OCT data.

5.1 Sources of Randomness in OCT

As with any other realistic imaging system, there are many sources of randomness in an OCT imaging system. For example, fluctuations in the phase and the intensity of the source; shot noise, thermal noise, or $1/f$ noise in the detector; as well as fluctuations in the index of refraction in the object being imaged. In a lot of the OCT literature, the fluctuations in the refractive index have been ignored, and the object usually is modeled as a stack of homogeneous slabs described by different indices. In this analysis, we intend to present a model that will address the representative sources of randomness in an OCT system. The specific sources of randomness being discussed in the following sections include:

1. Intensity fluctuation of a broadband source due to phase fluctuation.
2. Fluctuations in the optical field due to scattering caused by fluctuations in refractive index of the object being imaged.
3. Shot noise caused by photo-detection process.

5.1.1 Phase Fluctuation of a Broadband Source

A light source can in general be considered as an ensemble of radiation emitters (for example, atoms) emitting electromagnetic waves at certain frequencies and phases. If every emitter emits at the same frequency and at a fixed phase relationship to each other, the source is termed a coherent source. When there is randomness in the frequencies or the phases at which the radiation is emitted within the ensemble of atoms, the source is termed an incoherent source, or partially coherent source, depending on the degree of coherence the source exhibits. The degree of coherence basically quantifies the randomness in the amplitudes, phases, and frequencies of a source's radiation. It also measures the source's capability in forming interference fringes. Coherent (deterministic) and incoherent sources only exist in the textbook paradigm, and any realistic source will be partially coherent.

A partially coherent source such as a non-laser source can be considered as a localized ensemble of independent classical radiators emitting electromagnetic fields that can be described by some random phasors. At an observation point far away from the source, the instantaneous field is the summation of all the random phasors. This instantaneous field will fluctuate on a time scale determined by the coherence time (τ_c) of the source, which is inversely proportional to the source spectral width ($\Delta\nu$). A longitudinal coherence length in the free space can be defined as (see also §4.2.1 on a discussion of optical coherence):

$$l_c = c\tau_c. \quad (5.1)$$

The transverse or spatial coherence length of the radiation is determined by the wavefront structure of the field.

5.1.2 Scattering Noise

As described in ref. [56], in the context of point scatterers, scattering noise corresponds to the intensity fluctuations of the scattered radiation which result from interactions between electromagnetic waves and media containing inhomogeneities of scattering centers. Two mechanisms – number fluctuation and interference fluctuation – contribute to the intensity fluctuation in the scattered radiation.

In the case of a continuous random medium, the description of the ensemble of points scatterers will be replaced by a continuous random field corresponding to the stochastic permittivity field of the medium. The discussion on number fluctuation will then be replaced by a discussion on whether the permittivity field exhibits Gaussian statistics or not. The concept of interference fluctuation will still be applicable.

Number Fluctuation

This corresponds to changes in the number of scattering centers inside the scattering volume, which is defined by the field of view of the detector, the dimensions of the incident beam and/or those of the scattering medium. Information of the motions and number of the particles can be obtained by analysis of such fluctuations in the scattered intensities. This type of fluctuation is usually termed "non-Gaussian" fluctuation. As the mean number of scattering centers increases, the effect of number fluctuation to the scattered intensity will be less pronounced. For a detailed discussion on effects of number fluctuation to scattered radiation, see ref. [56].

Interference Fluctuation

This type of fluctuation is caused by interference between the fields from different scattering centers. As mentioned in chapter 3 (Stochastic Waves), the fields originated from different scattering centers will sum up constructively or destructively and give rise to random bright or dark spots according to the spatial distribution

of the scattering centers. This rapidly varying dark and bright spatial pattern in the far-field is termed speckle. If a large number of scattering centers is present so that the effects of number fluctuations can be neglected, it can be shown that the fluctuating scattered radiation behaves mostly according to the Gaussian statistics, and thus will be referred to as the "Gaussian regime".

Though speckle is viewed as noise in coherent imaging, it is also used in a variety of measurement techniques to extract information of the object being imaged ([79] and [80]). In OCT, the sample wave is the sum of the scattered fields arising at different scattering sites within the coherent volume. These fields have random phases due to the random spatial distribution of scattering sites in the sample and due to fluctuating refractive index in the sample. If the phases and amplitudes of the individual fields can be considered as a series of statistically independent, and identically distributed random variables, having phases uniformly distributed over the 2π range, and the field is linearly polarized, then we have 'fully developed' speckle [81] and the resultant phasor of the sample wave behaves as a circular complex Gaussian random variable ([82] and [83]). The contrast of fully developed polarized speckle is a constant which is equal to one. However, the situation in OCT is more complex since the reference beam is mixed with the sample beam in the heterodyne detection and the condition leading to fully developed speckle will not hold anymore. Different techniques have been developed for suppression of speckle in OCT. A detailed description can be found in the review paper by [10] and the references therein.

In OCT, we can expect the observations of both type of fluctuations (namely, the number fluctuation and the interference fluctuation) in the scattered radiation, especially in dynamic focusing OCT where the coherent volume is moving according to the transverse and longitudinal scanning locations. As different parts of the sample are being imaged, the number of scattering centers falling into the coherent volume will vary from data point to data point.

From the analytical point of view, a complete study on the statistics of the scat-

tered field will demand the knowledge of the probability distributions for the solutions of stochastic differential equations. As mentioned in Chapter 3 (Stochastic Waves), solving stochastic differential equations is in itself a complicated problem still awaiting breakthrough theoretical developments and better mathematical tools. Some researchers have proposed approaches based on the characteristic functional of the wave field, which completely describes the probability structure of the stochastic field. However, this approach involves variational derivatives and there is not yet an effective method developed for its evaluation.

In general, the wave field is a non-Gaussian field [47]. However, two situations exist where one can define (at least approximately) the probability distribution of the scattered field. In the first case, if the quantities characterizing the field can be described by random functions of the Markovian type, the probability distributions can be obtained from the Fokker-Planck-Kolmogorov equations. The second case is the Born approximation, in which the scattered field is a linear functional of the random permittivity field (or scattering potential). If the permittivity of the random medium has Gaussian statistics, then the wave field is also Gaussian. In the case when the medium is non-Gaussian, on the basis of the central limit theorem, one can argue that the scattered field is the summation of a great number of random variables. Then, approximately, the wave field will exhibit Gaussian, or near Gaussian, characteristics.

5.1.3 Photodetector Noise

A photodetector is a device that measures photon flux or electromagnetic radiation power by converting the absorbed energy into a measurable form of current or voltage. The underlying principle is the photoelectric effect, in which the absorption of photons by some materials results in the generation of mobile charge carriers. These carriers give rise to a measurable electric current when under the influence of an applied field.

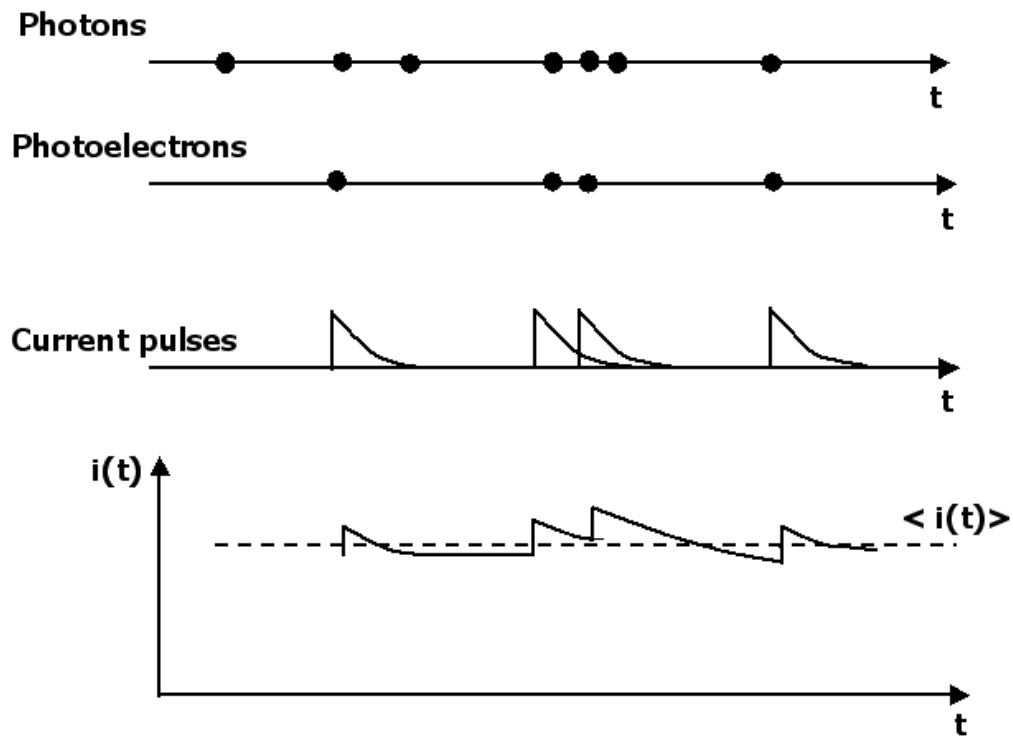


FIGURE 5.1. Illustration of shot noise. Photons arrive at a random time and are converted into photoelectrons randomly. The random current pulses cause fluctuations in the current output.

The output of such detectors consists of a series of discrete pulses of charge, each corresponding to a single photon detection. Even though the photoelectric effect involves the notion of photons as quantum particles, in most situations, a classical description of the electromagnetic wave without the photon notion will work fine for the understanding of the operation of photodetectors. The discrete pulses of charge, under many circumstances, behave as a Poisson process with a rate modulated by the incident intensity. A radiation detection system with the property that photoelectric noise is a major constraint on performance is referred to as photon-limited or quantum-noise-limited.

Mean and Variance of the Photocurrent

Figure 5.1 demonstrates the process of photocurrent generation [72]. When a photon hits the detector, a photoelectron will be generated by chance, and a current pulse $h(t, t')$ will be registered. The shape of the impulse response function of the detector $h(t, t')$ is determined by the material as well as the specific electronic design in the detector. However, the area of $h(t, t')$ will be a multiple of the unit electron charge e . The output current is the sum of all the discrete pulses.

Mathematically, the sequence of photoelectrons can be described as a random point process governed by Poisson statistics:

$$g(t) = \sum_{n=1}^N \delta(t - t_n). \quad (5.2)$$

Consider $g(t)$ as the input of a filter described by the impulse response function $h(t, t')$. Then the photocurrent $i(t)$ at the filter output can be written as

$$i(t) = \int_{-\infty}^{\infty} dt' h(t, t') g(t'). \quad (5.3)$$

The mean of $g(t)$ is the average rate of photoelectrons generated per unit time. It is proportional to the incoming photon flux ($\Phi(t)$) and the quantum efficiency of the detector (ς , which describes the probability of a photon being converted into a photoelectron in the detector):

$$\langle g(t) \rangle = \varsigma \Phi(t). \quad (5.4)$$

The instantaneous photon flux $\Phi(t)$ can be expressed as:

$$\Phi(t) = \frac{P(t)}{h\nu_0}, \quad (5.5)$$

where $P(t)$ is the optical power on the detector and $h\nu_0$ the energy per photon. Being a Poisson process, the covariance of $g(t)$ can be written as [3]:

$$\begin{aligned} K_g(t_1, t_2) &= \langle g(t_1)g(t_2) \rangle - \langle g(t_1) \rangle \langle g(t_2) \rangle \\ &= \langle g(t_1) \rangle \delta(t_1 - t_2) \end{aligned} \quad (5.6)$$

Using eq. (5.3, 5.4, and 5.6), the mean and the covariance of the photocurrent can be written as

$$\begin{aligned} \langle i(t) \rangle &= \int_{-\infty}^{\infty} dt' h(t, t') \langle g(t') \rangle \\ &= \frac{\varsigma}{h\nu_0} \int_{-\infty}^{\infty} dt' h(t, t') P(t'). \end{aligned} \quad (5.7)$$

and

$$\begin{aligned} K_i(t_1, t_2) &= \int_{-\infty}^{\infty} dt'_1 \int_{-\infty}^{\infty} dt'_2 h(t_1, t'_1) h(t_2, t'_2) \langle g(t'_1) \rangle \delta(t'_1 - t'_2) \\ &= \frac{\varsigma}{h\nu_0} \int_{-\infty}^{\infty} dt' h(t_1, t') h(t_2, t') P(t'). \end{aligned} \quad (5.8)$$

5.2 Stochastic Object Model

Before we go into the detailed derivation of the covariance function of the demodulated OCT data, we will first introduce a mathematical model for the random medium being imaged.

As mentioned in Chapter 3, most realistic media are stochastic in nature due to fluctuations in refractive index or other physical properties. In this section, we will introduce a stochastic model to describe the permittivity, and thus, the scattering potential, of a random medium. We will first establish the relationships between permittivity, refractive index, and scattering potential. Then a stochastic model for the permittivity field will be developed on a generalized Poisson process, with the derivation of the mean and the second order statistic of the random field. These results will be used in the evaluation of the covariance function of the demodulated OCT data stream. Finally, we will link the permittivity field of the medium to its bulk optical properties such as the attenuation coefficient and scattering cross section.

5.2.1 Permittivity Field, Refractive Index, and Scattering Potential

As shown in chapter 3, the relative permittivity field of the media can be written as

$$\varepsilon(\mathbf{r}) = \langle \varepsilon(\mathbf{r}) \rangle (1 + \tilde{\varepsilon}(\mathbf{r})), \quad (5.9)$$

where $\tilde{\varepsilon}(\mathbf{r})$ is the fluctuation of the permittivity field, and is defined as

$$\tilde{\varepsilon}(\mathbf{r}) = \frac{1}{\langle \varepsilon(\mathbf{r}) \rangle} (\varepsilon(\mathbf{r}) - \langle \varepsilon(\mathbf{r}) \rangle) \equiv \frac{\delta\varepsilon(\mathbf{r})}{\langle \varepsilon(\mathbf{r}) \rangle}. \quad (5.10)$$

From the above definition, it can be shown that

$$\langle \tilde{\varepsilon}(\mathbf{r}) \rangle = 0. \quad (5.11)$$

Similarly, the refractive index of the media can be written as

$$n(\mathbf{r}) = \langle n(\mathbf{r}) \rangle (1 + \tilde{n}(\mathbf{r})), \quad (5.12)$$

where $\tilde{n}(\mathbf{r})$ is the fluctuation of the refractive index, and is defined as

$$\tilde{n}(\mathbf{r}) = \frac{1}{\langle n(\mathbf{r}) \rangle} (n(\mathbf{r}) - \langle n(\mathbf{r}) \rangle) \equiv \frac{\delta n(\mathbf{r})}{\langle n(\mathbf{r}) \rangle}. \quad (5.13)$$

Also, by definition shown in eq. (5.13),

$$\langle \tilde{n}(\mathbf{r}) \rangle = 0. \quad (5.14)$$

The index of refraction relates to the permittivity of the media as :

$$\varepsilon(\mathbf{r}) = n^2(\mathbf{r}). \quad (5.15)$$

Using eqs. (5.12), the above equation can be written as

$$\varepsilon(\mathbf{r}) = \langle n(\mathbf{r}) \rangle^2 (1 + 2\tilde{n}(\mathbf{r}) + \tilde{n}^2(\mathbf{r})). \quad (5.16)$$

For weak fluctuation (see §3.2.1 for discussion on weak fluctuation), $\tilde{n}^2(\mathbf{r}) \ll \tilde{n}(\mathbf{r})$, then eq. (5.16) can be approximated as

$$\varepsilon(\mathbf{r}) \approx \langle n(\mathbf{r}) \rangle^2 (1 + 2\tilde{n}(\mathbf{r})). \quad (5.17)$$

Using eq. (5.14), the ensemble average of $\varepsilon(\mathbf{r})$, for weak fluctuation, can be written as

$$\langle \varepsilon(\mathbf{r}) \rangle = \langle n(\mathbf{r}) \rangle^2 \equiv \bar{n}^2 \quad (5.18)$$

where \bar{n} is the average refractive index of the sample and is assumed to be constant for a stationary permittivity field. Then eq. (5.9) can be written as

$$\varepsilon(\mathbf{r}) = \bar{n}^2(1 + \tilde{\varepsilon}(\mathbf{r})). \quad (5.19)$$

Comparing eq. (5.19) to eq. (5.17), it can be shown that

$$\tilde{\varepsilon}(\mathbf{r}) \approx 2\tilde{n}(\mathbf{r}). \quad (5.20)$$

Using eq. (5.19), the covariance function of the permittivity field ($K_\varepsilon(\mathbf{r}_1, \mathbf{r}_2)$) can be written as

$$\begin{aligned} K_\varepsilon(\mathbf{r}_1, \mathbf{r}_2) &= \langle \varepsilon(\mathbf{r}_1)\varepsilon(\mathbf{r}_2) \rangle - \bar{\varepsilon}(\mathbf{r}_1)\bar{\varepsilon}(\mathbf{r}_2) \\ &= \bar{n}^4 \langle \tilde{\varepsilon}(\mathbf{r}_1)\tilde{\varepsilon}(\mathbf{r}_2) \rangle. \end{aligned} \quad (5.21)$$

As shown in Chapter 3, the scattering potential of the random medium is defined as

$$\mathcal{V}(\mathbf{r}') = k^2\tilde{\varepsilon}(\mathbf{r}').$$

Using eq. (5.11), it is easy to show that

$$\langle \mathcal{V}(\mathbf{r}) \rangle = 0. \quad (5.22)$$

Therefore, the covariance function of $\mathcal{V}(\mathbf{r})$ is

$$K_{\mathcal{V}}(\mathbf{r}_1, \mathbf{r}_2) = \langle \mathcal{V}(\mathbf{r}_1)\mathcal{V}(\mathbf{r}_2) \rangle = k^4 \langle \tilde{\varepsilon}(\mathbf{r}_1)\tilde{\varepsilon}(\mathbf{r}_2) \rangle. \quad (5.23)$$

Using eq. (5.21), $K_{\mathcal{V}}(\mathbf{r}_1, \mathbf{r}_2)$ can be related to the covariance function of the permittivity field $K_\varepsilon(\mathbf{r}_1, \mathbf{r}_2)$ as:

$$K_{\mathcal{V}}(\mathbf{r}_1, \mathbf{r}_2) = \frac{k^4}{\bar{n}^4} K_\varepsilon(\mathbf{r}_1, \mathbf{r}_2) = k_0^4 K_\varepsilon(\mathbf{r}_1, \mathbf{r}_2). \quad (5.24)$$

In the following section, we will derive an expression for $K_\varepsilon(\mathbf{r}_1, \mathbf{r}_2)$ based on a generalized Poisson model.

5.2.2 Stochastic Model of the Permittivity Field

As described in ref [84], there are only limited classes of random fields for which complete descriptions of the probability density functions are available through the characteristic functionals. One class consists of Gaussian functions and another class is the generalized Poisson random field.

The sample function of a simple spatial Poisson random field is a sum of delta functions in space

$$f(\mathbf{r}) = \sum_{n=1}^N \delta(\mathbf{r} - \mathbf{r}_n), \quad (5.25)$$

where N is a random variable describing the total number of points in the region of interest, and it obeys the Poisson statistics:

$$\Pr(N) = \frac{\bar{N}^N}{N!} \exp(-\bar{N}). \quad (5.26)$$

The set of vectors $\{\mathbf{r}_n\}$ is a set of random vectors corresponding to the positions of the points. In a Poisson random field, the points are distributed randomly and independent to each other. Therefore, the probability density function (PDF) of the field composed of N particles is just simply the product of the PDFs of the individual particles:

$$pr(\{\mathbf{r}_n\}|N) = \prod_{n=1}^N pr(\mathbf{r}_n), \quad (5.27)$$

with $pr(\mathbf{r}_n)$ the probability of the site \mathbf{r}_n being occupied by a particle. It can be written as [3]:

$$pr(\mathbf{r}_n) = \frac{b(\mathbf{r}_n)}{\int_{\Omega} d\mathbf{r} b(\mathbf{r})}. \quad (5.28)$$

The domain of the integral Ω corresponds to the region of interest. It can be a plane for a 2D entity, or a volume in 3D. If $f(\mathbf{r})$ in eq. (5.25) describes the photon distribution of an object, $b(\mathbf{r})$ is the mean photon fluence of the object. On the other hand, $b(\mathbf{r})$ can also be interpreted as the mean number density of points in the region of interest. Integration of $b(\mathbf{r})$ over the region of interest corresponds to the mean

number of particles within the region of interest:

$$\int_{\Omega} d\mathbf{r} b(\mathbf{r}) = \bar{N}. \quad (5.29)$$

The independence between particles in the Poisson random field model basically corresponds to a "perfect gas" model in statistical physics. The mathematical simplicity of the Poisson model makes it popular in many applications. However, there are situations when the interaction between the particles cannot be ignored and the Poisson model will not be applicable. Such systems should be analyzed by using the general theory of stochastic point processes [85]. Also, if the particles are of finite size, and if the particle distribution is not sparse (for example, biological tissue), then the Poisson random field model will not be valid in general since it will introduce configurations in which the particles will overlap and correspond to unrealistic penetration of particles. Therefore, only when the particle distribution is sparse, the Poisson field will serve as a reasonable approximation.

In ref. [84], Tatarskii describes a generalized Poisson random field that can be applied to describe a non-Gaussian random medium or surface for wave scattering. Basically, the random field is composed of an assemble of "bursts", which can be understood as concentrations of material that correspond to changes in the permittivity field of the random medium. This generalized Poisson random field has the following properties:

- (i) The number of bursts is random and has an arbitrary probability distribution.
- (ii) The position of each burst is random and has an arbitrary probability distribution.
- (iii) The amplitude of each burst is random and has an arbitrary probability distribution.
- (iv) The shape of each burst is a given function that may depend on its position.

Employing the generalized Poisson random field model, the permittivity field $\varepsilon(\mathbf{r})$

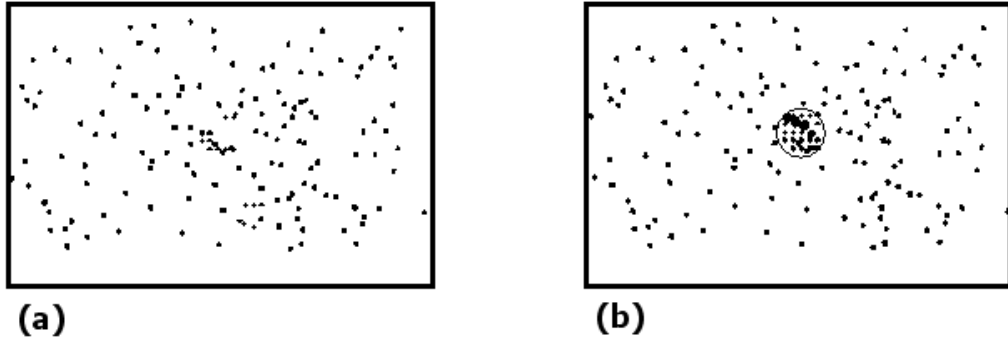


FIGURE 5.2. (a) The point particles distribute randomly but uniformly over the plane of area A . (b) There is a higher concentration of points within the central circle, but the location of the point particles are still random in a way that they are not laid out according to any pattern. If the width of the central circle varies, then the corresponding probability density function describing the spatial distribution of the particles is a random function.

of a random medium can be written as

$$\varepsilon(\mathbf{r}) = \sum_{n=1}^N \xi_n g(\mathbf{r}, \mathbf{r}_n). \quad (5.30)$$

Rolland et al. [86] proposed a lumpy model, which was developed on a similar random Poisson field model, to describe stochastic backgrounds for detection task studies in medical imaging. Using the terminologies of the lumpy model, eq. (5.30) indicates that $\varepsilon(\mathbf{r})$ is modeled as an aggregate of three dimensional lumps $\xi_n g(\mathbf{r}, \mathbf{r}_n)$. The total number of lumps N is a Poisson random variable. The amplitude or strength of each lump is described by ξ_n , which is a random variable with characteristic function:

$$\varphi(a) = \langle e^{ia\xi} \rangle = \int d\xi pr(\xi) e^{ia\xi}. \quad (5.31)$$

The lump function $g(\mathbf{r}, \mathbf{r}_n)$ has its center at \mathbf{r}_n , which is a random vector governed by the probability density function $W_g(\mathbf{r}_n)$. To illustrate the behavior of $W_g(\mathbf{r}_n)$, we will use a two dimensional spatial Poisson random field as an example. Consider a 2D plane with area A as shown in figure 5.2. For simplicity, we will assume that ξ_n is a non-random constant, and the lumps $g(\mathbf{r}, \mathbf{r}_n) \rightarrow \delta(\mathbf{r} - \mathbf{r}_n)$ are point particles.

The distribution of these points are governed by the function $W_g(\mathbf{r}_n)$. In the simplest case,

$$W_g(\mathbf{r}_n) = \frac{1}{A}. \quad (5.32)$$

It means that any location (\mathbf{r}_n) on the 2D plane will be equally probable to be occupied by the point particles with a probability of $\frac{1}{A}$. We will say that the point particles are randomly distributed according to a uniform probability distribution for their locations (see figure 5.2 (a)). In other cases, a particular region in the 2D plane may have a higher probability to be occupied by the point particles. Then we will have a non-uniform distribution for the location of the point particles (see figure 5.2 (b)). Sometimes, one can let the width of the central circle in figure 5.2 (b) vary as a random variable according to a certain probability law (such as a normal distribution described by the average width of the area with a certain variance). Then the distribution $W_g(\mathbf{r}_n)$ becomes a random field itself.

Similar to the discussion of eq. (5.28) in §5.2.2, the probability distribution function $W_g(\mathbf{r})$ can be defined via a function $\Upsilon(\mathbf{r})$ as:

$$W_g(\mathbf{r}) = \frac{\Upsilon(\mathbf{r})}{\int d\vec{r} \Upsilon(\mathbf{r})} = \frac{\Upsilon(\mathbf{r})}{\bar{N}}. \quad (5.33)$$

The function $\Upsilon(\mathbf{r})$ is the 3D version of the 2D photon fluence $b(\mathbf{r})$ in eq. (5.28), and it satisfies the relationship (see eq. (5.29))

$$\int d\mathbf{r} \Upsilon(\mathbf{r}) = \bar{N}, \quad (5.34)$$

with \bar{N} the average number of lumps constituting the object. Using eq. (5.34), it is easy to verify that the unit of $\Upsilon(r)$ is number per volume, ie, the number density of the lumps. Eq. (5.34) also shows that \bar{N} will be random if $\Upsilon(\mathbf{r})$ is a random field (ie, $W_g(\mathbf{r})$ is a random field).

In the case that $W_g(\mathbf{r}_n)$ is a random field, to evaluate the covariance of the permittivity field described in eq. (5.30), we need to consider the ensemble average over

all the possible randomnesses in N , $\{\mathbf{r}_n\}$, ξ_n , as well as W_g :

$$\begin{aligned} K_\varepsilon(\mathbf{r}_1, \mathbf{r}_2) &= \langle \varepsilon(\mathbf{r}_1)\varepsilon(\mathbf{r}_2) \rangle_{N, \{\mathbf{r}_n\}, \xi_n, W_g} \\ &- \langle \varepsilon(\mathbf{r}_1) \rangle_{N, \{\mathbf{r}_n\}, \xi_n, W_g} \langle \varepsilon(\mathbf{r}_2) \rangle_{N, \{\mathbf{r}_n\}, \xi_n, W_g}. \end{aligned} \quad (5.35)$$

Let

$$A_{\varepsilon|W_g}(\mathbf{r}) = \langle \varepsilon(\mathbf{r}) | W_g \rangle_{N, \{\mathbf{r}_n\}, \xi_n},$$

which represents the first moment of $\varepsilon(\mathbf{r})$ when conditioned on a particular realization of W_g , and

$$B_{\varepsilon|W_g}(\mathbf{r}_1, \mathbf{r}_2) = \langle \varepsilon(\mathbf{r}_1)\varepsilon(\mathbf{r}_2) | W_g \rangle_{N, \{\mathbf{r}_n\}, \xi_n}$$

the conditional second moment of $\varepsilon(\mathbf{r})$. Then, eq. (5.35) can be written as

$$K_\varepsilon(\mathbf{r}_1, \mathbf{r}_2) = \langle B_{\varepsilon|W_g}(\mathbf{r}_1, \mathbf{r}_2) \rangle_{W_g} - \langle A_{\varepsilon|W_g}(\mathbf{r}_1) \rangle_{W_g} \langle A_{\varepsilon|W_g}(\mathbf{r}_2) \rangle_{W_g}. \quad (5.36)$$

Eq. (5.36) indicates a two-step approach to calculate the covariance of the permittivity field. First, one will calculate the average of the permittivity field over the first set of random elements $\{N, \{\mathbf{r}_n\}, \xi_n\}$ when conditioned on a particular realization of W_g . Secondly, the average over the randomness of W_g (i.e., $\langle \dots \rangle_{W_g}$) will be carried out. It can be shown that, for a general random field $Q(\mathbf{r})$ described by the lumpy model in eq. (5.30) with a deterministic spatial distribution $W_g(\mathbf{r}_n)$, if the number of lumps obey Poisson statistics, the first and the second moments of $Q(\mathbf{r})$ can be written as [84]:

$$A_Q(\mathbf{r}) = \langle Q(\mathbf{r}) \rangle_{\{N, \{\mathbf{r}_n\}, \xi_n\}} = F_1 \langle \xi \rangle G_1(\mathbf{r}), \quad (5.37)$$

and

$$\begin{aligned} B_Q(\mathbf{r}_1, \mathbf{r}_2) &= \langle Q(\mathbf{r}_1)Q(\mathbf{r}_2) \rangle_{\{N, \{\mathbf{r}_n\}, \xi_n\}} \\ &= F_1 \langle \xi^2 \rangle G_2(\mathbf{r}_1, \mathbf{r}_2) + F_2 \langle \xi \rangle^2 G_1(\mathbf{r}_1)G_1(\mathbf{r}_2), \end{aligned} \quad (5.38)$$

where $\langle \xi \rangle$ and $\langle \xi^2 \rangle$ are the first and second moment of the random variable ξ , respectively, which can be evaluated using the characteristic function of ξ (see eq. (5.31)).

The quantities F_1 , F_2 , $G_1(\mathbf{r})$ and $G_2(\mathbf{r}_1, \mathbf{r}_2)$ can be evaluated using the following expressions given in ref. [84]:

$$F_n = \langle N(N-1)(N-2)\dots(N-n+1) \rangle = \overline{N}^n = (F_1)^n, \quad (5.39)$$

$$G_1(\mathbf{r}) = \int W_g(\mathbf{r}')g(\mathbf{r}, \mathbf{r}')d\mathbf{r}', \quad (5.40)$$

and

$$G_2(\mathbf{r}_1, \mathbf{r}_2) = \int W_g(\mathbf{r}')g(\mathbf{r}_1, \mathbf{r}')g(\mathbf{r}_2, \mathbf{r}')d\mathbf{r}'. \quad (5.41)$$

Substituting eqs. (5.37 and 5.38) into eq. (5.36), then the covariance of the permittivity field can be written as

$$\begin{aligned} K_\varepsilon(\mathbf{r}_1, \mathbf{r}_2) = & \langle F_1 \langle \xi^2 \rangle G_2(\mathbf{r}_1, \mathbf{r}_2) + F_2 \langle \xi \rangle^2 G_1(\mathbf{r}_1)G_1(\mathbf{r}_2) \rangle_{W_g} \\ & - \langle F_1 \langle \xi \rangle G_1(\mathbf{r}_1) \rangle_{W_g} \langle F_1 \langle \xi \rangle G_1(\mathbf{r}_2) \rangle_{W_g}. \end{aligned} \quad (5.42)$$

where $G_1(\mathbf{r}_1)$ and $G_2(\mathbf{r}_1, \mathbf{r}_2)$ are given by eqs. (5.40 and 5.41). According to eq. (5.39),

$$F_1 = \overline{N}, \quad (5.43)$$

and

$$F_2 = (F_1)^2 = \overline{N}^2, \quad (5.44)$$

then eq. (5.42) can be written as

$$\begin{aligned} K_\varepsilon(\mathbf{r}_1, \mathbf{r}_2) = & \langle \xi^2 \rangle \langle \overline{N}G_2(\mathbf{r}_1, \mathbf{r}_2) \rangle_{W_g} + \langle \xi \rangle^2 \langle \overline{N}^2G_1(\mathbf{r}_1)G_1(\mathbf{r}_2) \rangle_{W_g} \\ & - (\langle \xi \rangle)^2 \langle \overline{N}G_1(\mathbf{r}_1) \rangle_{W_g} \langle \overline{N}G_1(\mathbf{r}_2) \rangle_{W_g} \\ = & \langle \xi^2 \rangle \langle \overline{N}G_2(\mathbf{r}_1, \mathbf{r}_2) \rangle_{W_g} + \langle \xi \rangle^2 K_{G_1}(\mathbf{r}_1, \mathbf{r}_2), \end{aligned} \quad (5.45)$$

where

$$K_{G_1}(\mathbf{r}_1, \mathbf{r}_2) = \langle \overline{N}^2G_1(\mathbf{r}_1)G_1(\mathbf{r}_2) \rangle_{W_g} - \langle \overline{N}G_1(\mathbf{r}_1) \rangle_{W_g} \langle \overline{N}G_1(\mathbf{r}_2) \rangle_{W_g}. \quad (5.46)$$

We have to keep the quantities \overline{N} and \overline{N}^2 inside the angle bracket $\langle \dots \rangle_{W_g}$, since \overline{N} is random if $W_g(\mathbf{r})$ is a random field. In the case when $W_g(\mathbf{r})$ is deterministic, $K_{G_1}(\mathbf{r}_1, \mathbf{r}_2) = 0$ and \overline{N} is non-random. Then the covariance function of the permittivity field reduces to

$$\begin{aligned} K_\varepsilon(\mathbf{r}_1, \mathbf{r}_2) &= \overline{N} \langle \xi^2 \rangle G_2(\mathbf{r}_1, \mathbf{r}_2) \\ &= \overline{N} \langle \xi^2 \rangle \int W_g(\mathbf{r}') g(\mathbf{r}_1, \mathbf{r}') g(\mathbf{r}_2, \mathbf{r}') d\mathbf{r}'. \end{aligned} \quad (5.47)$$

5.2.3 Scattering Cross Section and Attenuation Coefficient

As mentioned in chapter 3, scattering is a phenomena caused by fluctuations in refractive index in a random medium. In this section, we will show the relationship between the fluctuation of the permittivity field and the scattering cross section of a random medium. As shown in ref. [51], for weak fluctuations, using the first Born approximation, the scattering amplitude of an incident plane wave $\widehat{\mathbf{e}}_i \exp(i\widehat{k}\mathbf{i} \cdot \mathbf{r})$ can be written as (similar to eq. (3.20)):

$$\mathbf{f}(\widehat{\mathbf{o}}, \widehat{\mathbf{i}}) = \widehat{\mathbf{e}}_s \sin \chi \frac{k^2}{4\pi} \int_V dV' \widetilde{\varepsilon}(\mathbf{r}') \exp(i\mathbf{k}_s \cdot \mathbf{r}'), \quad (5.48)$$

where the unit vector \widehat{i} depicts the incident direction of the beam, and \widehat{o} the scattered direction. The angle χ represents the angle between the polarization of the field and the plane spanned by the unit vectors \widehat{i} and \widehat{o} . It is assumed that $\chi = 90^\circ$ in this analysis. The wave vector for the scattered wave is $\mathbf{k}_s = k(\widehat{i} - \widehat{o})$, and $k_s = 2k \sin(\frac{\theta}{2})$, where θ is the deflected angle between the incident and scattered wave. The differential cross section per unit volume of the medium is defined as

$$\sigma(\widehat{o}, \widehat{i}) = \frac{\langle |\mathbf{f}(\widehat{\mathbf{o}}, \widehat{\mathbf{i}})|^2 \rangle}{V}, \quad (5.49)$$

where V is the scattering volume. Using eq. (5.48), $\sigma(\widehat{o}, \widehat{i})$ can be written as

$$\sigma(\widehat{o}, \widehat{i}) = \left(\frac{k^2}{4\pi} \right)^2 \frac{1}{V} \int_V dV_1 \int_V dV_2 \langle \widetilde{\varepsilon}(\mathbf{r}_1) \widetilde{\varepsilon}(\mathbf{r}_2) \rangle \exp(i\mathbf{k}_s \cdot (\mathbf{r}_1 - \mathbf{r}_2)). \quad (5.50)$$

If the medium is statistically homogeneous and isotropic, then $\langle \tilde{\varepsilon}(\mathbf{r}_1)\tilde{\varepsilon}(\mathbf{r}_2) \rangle$ is a function of $r_- = |\mathbf{r}_1 - \mathbf{r}_2|$:

$$\langle \tilde{\varepsilon}(\mathbf{r}_1)\tilde{\varepsilon}(\mathbf{r}_2) \rangle = B_{\tilde{\varepsilon}}(r_-). \quad (5.51)$$

Then eq. (5.50) can be simplified as [51]

$$\sigma(\hat{o}, \hat{i}) = 2\pi k^4 \Phi_{\tilde{n}}(k_s), \quad (5.52)$$

where

$$\Phi_{\tilde{n}}(k) = \frac{1}{(2\pi)^3} \int_{\infty} dV_d B_{\tilde{n}}(r_d) \exp(i\mathbf{K} \cdot \mathbf{r}_-), \quad (5.53)$$

and

$$B_{\tilde{n}}(r_d) = \langle \tilde{n}(\mathbf{r})\tilde{n}(\mathbf{r} + \mathbf{r}_-) \rangle = \frac{1}{4} B_{\tilde{\varepsilon}}(r_-). \quad (5.54)$$

The backscattering cross section per unit volume of a random medium is defined as

$$\sigma_b = 4\pi\sigma(-\hat{i}, \hat{i}). \quad (5.55)$$

Then for a statistically homogeneous and isotropic medium, using eqs. ((5.52) and (5.55)), the backscattering cross section per unit volume of the medium can be written as

$$\sigma_b = k^4 \frac{1}{4\pi} \frac{1}{\bar{n}^4} \mathcal{F}\{K_{\varepsilon}(\mathbf{r}_-)\}_{k_s=2k_0}, \quad (5.56)$$

where $K_{\varepsilon}(\mathbf{r}_-) = \bar{n}^4 \langle \tilde{\varepsilon}(\mathbf{r}_1)\tilde{\varepsilon}(\mathbf{r}_2) \rangle$ (see eq. (5.21)).

The attenuation constant due to scattering can then be obtained by integrating the differential scattering cross section per unit volume over all the possible direction [51]:

$$\mu_s = \int_{4\pi} d\Omega \sigma(\hat{o}, \hat{i}), \quad (5.57)$$

where $\sigma(\hat{o}, \hat{i})$ is given by eq. (5.50).

5.3 Covariance Function of a Random Field Driven by Multiple Sources of Randomness

In the previous sections, we have discussed the different sources of randomness in an OCT imaging modality, and particularly, a mathematical model for the random medium. In the following sections, we will derive a general expression of the covariance function for a random field driven by multiple sources of randomness, and then apply the result to an OCT imaging modality.

Consider a random field $s(t)$, with multiple sources driving its stochastic behavior. Let $s_i(t) = \langle s(t) \rangle_i$ represent the average of $s(t)$ over the i^{th} source of randomness, and $s_{i,j}(t) = \langle s(t) \rangle_{i,j} = \langle s_i(t) \rangle_j$ the average of $s(t)$ over the i^{th} and the j^{th} sources of randomness, etc.,.... Now, consider the case when there are three sources of randomness, as in the current model for OCT analysis. The goal of this section is to derive a general expression for the covariance function on $s(t)$ for such a system. Assuming that $s(t)$ is real, then by definition, the covariance function of $s(t)$ can be written as

$$K_s(x, y) = \langle s(x)s(y) \rangle_{1,2,3} - s_{1,2,3}(x)s_{1,2,3}(y). \quad (5.58)$$

By adding and subtracting $s_1(x)$ and $s_1(y)$ within the angle parenthesis, eq. (5.58) can be written as

$$\begin{aligned} K_s(x, y) &= \langle (s(x) - s_1(x) + s_1(x))(s(y) - s_1(y) + s_1(y)) \rangle_{1,2,3} \\ &\quad - s_{1,2,3}(x)s_{1,2,3}(y) \\ &= \langle (s(x) - s_1(x))(s(y) - s_1(y)) \rangle_{1,2,3} \\ &\quad + \langle s_1(x)s_1(y) \rangle_{2,3} - s_{1,2,3}(x)s_{1,2,3}(y). \end{aligned} \quad (5.59)$$

Similarly, we will rewrite $\langle s_1(x)s_1(y) \rangle_{2,3}$ as

$$\begin{aligned} &\langle s_1(x)s_1(y) \rangle_{2,3} \\ &= \langle (s_1(x) - s_{1,2}(x) + s_{1,2}(x))(s_1(y) - s_{1,2}(y) + s_{1,2}(y)) \rangle_{2,3} \\ &= \langle (s_1(x) - s_{1,2}(x))(s_1(y) - s_{1,2}(y)) \rangle_{2,3} + \langle s_{1,2}(x)s_{1,2}(y) \rangle_3. \end{aligned}$$

Then eq. (5.59) can be written as

$$\begin{aligned}
K_s(x, y) &= \langle \langle (s(x) - s_1(x))(s(y) - s_1(y)) \rangle_1 \rangle_{2,3} \\
&+ \langle \langle (s_1(x) - s_{1,2}(x))(s_1(y) - s_{1,2}(y)) \rangle_2 \rangle_3 \\
&+ \langle \langle (s_{1,2}(x) - s_{1,2,3}(x))(s_{1,2}(y) - s_{1,2,3}(y)) \rangle_3 \rangle_3 . \tag{5.60}
\end{aligned}$$

In a more compact form, eq. (5.60) can be written as

$$K_s(x, y) \equiv \langle K_s^1(x, y) | 2, 3 \rangle_{2,3} + \langle K_{s_1}^2(x, y) | 3 \rangle_3 + K_{s_{1,2}}^3(x, y), \tag{5.61}$$

where

$$\langle K_s^1(x, y) | 2, 3 \rangle_{2,3} = \langle \langle (s(x) - s_1(x))(s(y) - s_1(y)) \rangle_1 \rangle_{2,3}, \tag{5.62}$$

$$\langle K_{s_1}^2(x, y) | 3 \rangle_3 = \langle \langle (s_1(x) - s_{1,2}(x))(s_1(y) - s_{1,2}(y)) \rangle_2 \rangle_3, \tag{5.63}$$

and

$$K_{s_{1,2}}^3(x, y) = \langle (s_{1,2}(x) - s_{1,2,3}(x))(s_{1,2}(y) - s_{1,2,3}(y)) \rangle_3 . \tag{5.64}$$

Eq. (5.60) shows how the covariance function of a random field driven by multiple sources can be decomposed into the sum of covariance functions in which only one source of randomness is considered at each time.

In the first term of eq. (5.61), the notation $K_s^1(x, y)$ corresponds to the covariance between $s(x)$ and $s(y)$ with respect to the randomness driven by source 1, conditioned on a particular realization of the random fields corresponding to the random sources 2 and 3. That is, $K_s^1(x, y) = \langle (s(x) - s_1(x))(s(y) - s_1(y)) \rangle_1$. Then $K_s^1(x, y)$ is averaged over the ensembles of sources 2 and 3 to account for the complete randomness.

Similarly, the notation $K_{s_1}^2(x, y)$ in the second term corresponds to the covariance between the averaged signals $s_1(x)$ and $s_1(y)$ with respect to the randomness driven by source 2, conditioned on a particular realization of the random field corresponding to the source 3. That is, $K_{s_1}^2(x, y) = \langle (s_1(x) - s_{1,2}(x))(s_1(y) - s_{1,2}(y)) \rangle_2$.

Then $K_{s_1}^2(x, y)$ is averaged over the different realizations corresponding to source 3 to account for the complete randomness.

Finally, $K_{s_{1,2}}^3(x, y)$ is the covariance between $s_{1,2}(x)$ and $s_{1,2}(y)$ with respect to the randomness driven by source 3.

5.4 Covariance Function of OCT Data

In this analysis, as discussed at the beginning of this chapter, three sources of randomness will be discussed. They are: the source fluctuation, scattering noise and the photo-detection noise. We will adopt the following notations for the mean and covariance of the demodulated OCT data stream $s(t)$:

- The mean of $s(t)$ will be denoted as $s_{P,F,M}(t) = \langle s(t) \rangle_{P,F,M}$. The subscript P corresponds to the Poisson noise due to fluctuations relating to photo-detection; F corresponds to fluctuations in the source field, which is assumed to be described by the Gaussian statistics; while the subscript M corresponds to the refractive index fluctuation in the random media.
- The covariance of the data stream $s(t)$ is then defined as

$$K_s(t_1, t_2) = \langle s(t_1)s(t_2) \rangle_{P,F,M} - \langle s(t_1) \rangle_{P,F,M} \langle s(t_2) \rangle_{P,F,M}. \quad (5.65)$$

The properties of the OCT data depend heavily on the demodulation schemes. In this analysis, only the mixer scheme (see Chapter 4) is discussed. One important feature resulting from this demodulation scheme is that the mean of the demodulated OCT data is zero, i.e., $\langle s(t) \rangle_{P,F,M} = 0$ (see Appendix A). Using eq. (5.61), the covariance function for the OCT system takes on the form,

$$K_s(t_1, t_2) = \langle K_s^P(t_1, t_2) | F, M \rangle_{F,M} + \langle K_{s_P}^F(t_1, t_2) | M \rangle_M + K_{s_{P,F}}^M(t_1, t_2). \quad (5.66)$$

Similar to eqs. ((5.62), (5.63), and (5.64)), the terms at the right hand side of eq. (5.66) can be written as

$$\langle K_s^P(t_1, t_2) | F, M \rangle_{F, M} = \langle \langle (s(t_1) - s_P(t_1))(s(t_2) - s_P(t_2)) \rangle_P \rangle_{F, M}, \quad (5.67)$$

$$\langle K_{s_P}^F(t_1, t_2) | M \rangle_M = \langle \langle (s_P(t_1) - s_{P,F}(t_1))(s_P(t_2) - s_{P,F}(t_2)) \rangle_F \rangle_M, \quad (5.68)$$

and

$$K_{s_{P,F}}^M(t_1, t_2) = \langle s_{P,F}(t_1)s_{P,F}(t_2) \rangle_M. \quad (5.69)$$

In writing down eq. (5.69), we have used the fact that $\langle s(t) \rangle_{P,F,M} = 0$.

In eq. (5.67), $K_s^P(t_1, t_2)$ corresponds to the covariance between the data with respect to the photo-detection noise (or imaging noise), conditioning on a particular realization of the source field and the sample. Since the photo-detection noise is assumed to be Poisson, $K_s^P(t_1, t_2)$ will reflect the statistics of Poisson random variables (such as statistical independence between different observation times). In eq. (5.68), $K_{s_P}^F(t_1, t_2)$ is the covariance between the averaged data s_P with respect to the source fluctuation, which is assumed to obey Gaussian statistics. In eq. (5.69), $K_{s_{P,F}}^M(t_1, t_2)$ is the covariance of the averaged data $s_{P,F}$ with respect to sample randomness. Since the randomness from the source and the imaging process has been averaged out, $s_{P,F}$ can be considered as the data that would be generated by an ideal source with no imaging noise. Therefore, $K_{s_{P,F}}^M(t_1, t_2)$ reflects solely the randomness due to fluctuations in the sample refractive index and corresponds to the scattering noise, with the refractive index fluctuation being the cause of the grainy structures in the images.

As mentioned in the section of Optical Coherence, the time scale of the source fluctuation is described by its coherence time τ_c , which is in the range of 10^{-15} s. On the other hand, the time scale for the photo-detection is determined by the data acquisition electronics. As described in §4.2.4 (Data acquisition: OCT electronics), the slowest component in the data acquisition chain is the band-pass filter with a

response time in the range of $100\mu s$. Any electronic filter acts as an integrator. As the integration time scale of the filter is much larger than the coherence time of the broadband source, the source fluctuation will basically be averaged out during the integration. Therefore, when compared to the shot noise contribution to the overall covariance function of the OCT data stream, the source fluctuation becomes insignificant and can be ignored for mathematical simplicity. This assertion can also be proved by performing an order of magnitude analysis as shown in a previous publication [87]. Then eq. (5.66) can be approximated as

$$\begin{aligned} K_s(t_1, t_2) &\approx \langle K_s^P(t_1, t_2)|F, M \rangle_{F,M} + K_{s_{P,F}}^M(t_1, t_2) \\ &\equiv K_{shot}(t_1, t_2) + K_{scat}(t_1, t_2). \end{aligned} \quad (5.70)$$

The first term $K_{shot}(t_1, t_2)$ is a short-hand notation for $\langle K_s^P(t_1, t_2)|F, M \rangle_{F,M}$:

$$\begin{aligned} K_{shot}(t_1, t_2) &= \langle K_s^P(t_1, t_2)|F, M \rangle_{F,M} \\ &= \langle \langle (s(t_1) - s_P(t_1))(s(t_2) - s_P(t_2)) \rangle_P \rangle_{F,M}, \end{aligned} \quad (5.71)$$

and it will be referred to as the shot noise contribution since $K_s^P(t_1, t_2)$ is the covariance of the demodulated data with respect to the shot noise conditioned on particular realizations of the source and the random medium. Similarly, $K_{scat}(t_1, t_2)$ is the short-hand notation of the term $K_{s_{P,F}}^M(t_1, t_2)$:

$$K_{scat}(t_1, t_2) = K_{s_{P,F}}^M(t_1, t_2) = \langle s_{P,F}(t_1)s_{P,F}(t_2) \rangle_M, \quad (5.72)$$

and it will be referred to as the scattering noise contribution. But it should be clear that each term ($K_{shot}(t_1, t_2)$ and $K_{scat}(t_1, t_2)$) actually encompasses all the randomness in the system. The terminologies proposed are just for the convenience of discussion.

Shot Noise Contribution

As shown in eq. (5.71), the shot noise contribution to the covariance function of the demodulated OCT data is:

$$K_{shot}(t_1, t_2) = \langle K_s^P(t_1, t_2)|F, M \rangle_{F,M}, \quad (5.73)$$

where $K_s^P(t_1, t_2)$ is the covariance function of the demodulated data with respect to a fixed realization of the source (F) and the random medium (M). For a particular realization of the source and the medium, the demodulated data are a filtered Poisson process. Using eqs. (4.94 and 4.90), the conditional mean of the demodulated data can be written as:

$$s_{P|F,M}(t) = \frac{1}{h\nu_0} \int dt' P(x)|_{F,M}(t') H_{Meyer}(t, t'), \quad (5.74)$$

where $P(x)|_{F,M}$ corresponds to the optical power for a particular realization of the source and the random medium. Using eq. (5.8), the covariance function of this filtered Poisson process can be written as:

$$K_s^P(t_1, t_2)|F, M = \frac{1}{h\nu_0} \int dx H_{Meyer}(t_1, x) P(x)|_{F,M} H_{Meyer}(t_2, x). \quad (5.75)$$

Plugging eq. (5.75) into eq. (5.73), the shot noise contribution to the covariance function of the demodulated data can be written as

$$K_{shot}(t_1, t_2) = \frac{1}{h\nu_0} \int dx H_{Meyer}(t_1, x) \langle P(x) \rangle_{F,M} H_{Meyer}(t_2, x). \quad (5.76)$$

As shown in eq. (4.63), the optical power $P(t)$ consists of two terms: the DC term ($P_{DC}(t)$) and the interferometric term ($P_{int}(t)$). Since the interferometric term $P_{int}(t)$ is linear in the scattering potential (see eqs. (4.68) and (4.69)), and the scattering potential ($\mathcal{V}(\mathbf{r})$) is a zero-mean random field (see eq. (5.22)), then $\langle P_{int}(x) \rangle_{F,M} = 0$. Therefore, the shot noise contribution from the interferometric term is zero and eq. (5.71) can be written as

$$K_{shot}(t_1, t_2) = \frac{1}{h\nu_0} \int dx H_{Meyer}(t_1, x) \langle P_{DC}(x) \rangle_{F,M} H_{Meyer}(t_2, x). \quad (5.77)$$

Using eq. (4.95), the product of $H_{Meyer}(t_1, x)H_{Meyer}(t_2, x)$ can be written as

$$\begin{aligned} & H_{Meyer}(t_1, x)H_{Meyer}(t_2, x) \\ &= (\zeta e)^2 \frac{1}{2} (\cos[2\omega_m x] + 1) \psi_{Meyer}(t_1, x) \psi_{Meyer}(t_2, x). \end{aligned} \quad (5.78)$$

Since $\langle P_{DC}(x) \rangle_{F,M}$ is a slowly varying function in time, when it is multiplied with $H_{Meyer}(t_1, x)H_{Meyer}^*(t_2, x)$ and integrated over x , the fast oscillating term involving $\cos[2\omega_m x]$ will be washed out. Therefore $K_{shot}(t_1, t_2)$ can be written as

$$K_{shot}(t_1, t_2) \approx \frac{(\zeta e)^2}{h\nu_0} \frac{1}{2} \int dx \langle P_{DC}(x) \rangle_{F,M} \psi_{Meyer}(t_1, x) \psi_{Meyer}(t_2, x). \quad (5.79)$$

Since

$$\langle P_{DC}(x) \rangle_{F,M} \approx const \equiv \langle P_{DC} \rangle_{F,M}, \quad (5.80)$$

then eq. (5.79) can be written as

$$K_{shot}(t_1, t_2) \approx \frac{(\zeta e)^2}{h\nu_0} \frac{1}{2} \langle P_{DC} \rangle_{F,M} \int dx \psi_{Meyer}(t_1, x) \psi_{Meyer}(t_2, x). \quad (5.81)$$

For $t_1 = t_2$,

$$K_{shot}(t, t) \approx \frac{(\zeta e)^2}{h\nu_0} \frac{1}{2} \langle P_{DC} \rangle_{F,M} \int dx \psi_{Meyer}^2(t, x). \quad (5.82)$$

For $t_1 \neq t_2$, the value of $K_{shot}(t_1, t_2)$ will depend on the overlap between the two wavelets $\psi_{Meyer}(t_1, x)$ and $\psi_{Meyer}(t_2, x)$. In this analysis, it is assumed that, as $t_1 \neq t_2$, $|t_1 - t_2| > \tau_b$, and the overlap between the two Meyer wavelet scaling functions will be non-significant. Therefore

$$K_{shot}(t_1, t_2) \approx 0, \quad \text{as } t_1 \neq t_2. \quad (5.83)$$

Scattering Noise Contribution

The noise contribution from the scattering process to the covariance function is (see eq. (5.72))

$$K_{scat}(t_1, t_2) = K_{s_{P,F}}^M(t_1, t_2) = \langle s_{P,F}(t_1) s_{P,F}(t_2) \rangle_M. \quad (5.84)$$

Using eq. (4.94), $s_{P,F}(t)$ can be written as

$$\begin{aligned} s_{P,F}(t) &= \int dt' \langle \Phi(t') \rangle_F H_{Meyer}(t, t') \\ &= \int dt' \langle \frac{1}{h\nu_0} P(t') \rangle_F H_{Meyer}(t, t'). \end{aligned} \quad (5.85)$$

Again, as shown in eq. (4.63), the optical power $P(t')$ can be written as

$$P(t') = P_{DC}(t') + P_{int}(t').$$

Since $\langle P_{DC}(t') \rangle_F$ is a slowly varying function in time, when it is multiplied with the fast oscillation ($\cos[2\omega_m x]$) in the response function $H_{Meyer}(t, t')$, and integrated over the response time of the data acquisition electronics, the result will be approximately zero, ie.,

$$\int dt' \langle P_{DC}(t') \rangle_F H_{Meyer}(t, t') \approx 0.$$

Then eq. (5.85) can be written as

$$s_{P,F}(t) = \frac{1}{h\nu_0} \int dt' \langle P_{int}(t') \rangle_F H_{Meyer}(t, t'). \quad (5.86)$$

Using eq. (4.68) for $P_{int}(t')$, then eq. (5.86) can be written as

$$s_{P,F}(t) = \frac{1}{h\nu_0} \int dt' \langle P_{rs}(t') + P_{rs}^*(t') \rangle_F H_{Meyer}(t, t'). \quad (5.87)$$

Plugging eq. (5.87) into eq. (5.84), then the scattering noise can be written as

$$\begin{aligned} K_{scat}(t_1, t_2) &= \left(\frac{1}{h\nu_0}\right)^2 \int dx_1 \int dx_2 H_{Meyer}(t_1, x_1) H_{Meyer}(t_2, x_2) \\ &< P_{rs,F}(x_1) P_{rs,F}(x_2) + P_{rs,F}(x_1) P_{rs,F}^*(x_2) + C.C. \rangle_M, \end{aligned} \quad (5.88)$$

where $P_{rs,F}(x) = \langle P_{rs}(x) \rangle_F$. In the following sections, we will derive an expression for $P_{rs,F}(t)$ using the expressions for the reference and sample beams presented in chapter 4. Then, the two time correlation function $\langle P_{rs,F}(t_1) P_{rs,F}^*(t_2) \rangle_M$ will be evaluated.

Complex Interferometric Optical Power As shown in eq. (4.70), the complex interferometric optical power can be written as

$$\begin{aligned} P_{rs,F}(t) &= \int_{\infty} d\boldsymbol{\rho} \int d\mathbf{r}_d \langle T(t'_{s,\mathcal{P}}) T^*(t'_{r,\mathcal{P}}) \rangle_F \\ &\mathcal{U}_{s,\mathcal{P}}(\boldsymbol{\rho}, \mathbf{r}_d; t) \mathcal{V}(\mathbf{r}_d + \boldsymbol{\rho}_b) U_{r,\mathcal{P}}^*(\boldsymbol{\rho}, t). \end{aligned} \quad (5.89)$$

The temporal correlation function can be written as (see eq. (4.26))

$$\langle T(t'_{s,\mathcal{P}})T^*(t'_{r,\mathcal{P}}) \rangle_F = |\gamma(t'_{s,\mathcal{P}} - t'_{r,\mathcal{P}})| = \exp[-(\frac{\pi\Delta\nu}{2\sqrt{\ln 2}})^2(t'_{s,\mathcal{P}} - t'_{r,\mathcal{P}})^2], \quad (5.90)$$

with

$$|t'_{s,\mathcal{P}} - t'_{r,\mathcal{P}}| = \left| 2\frac{v_a t}{c} - 2\frac{\bar{n}z_d}{c} \right|,$$

the time delay between the reference and sample arm. Then eq. (5.90) can be written as

$$\langle T(t'_{s,\mathcal{P}})T^*(t'_{r,\mathcal{P}}) \rangle_F = |\gamma(t'_{s,\mathcal{P}} - t'_{r,\mathcal{P}})| = \exp[-\frac{1}{\sigma^2}(\frac{v_a t}{\bar{n}} - z_d)^2], \quad (5.91)$$

with

$$\sigma = \frac{\sqrt{\ln 2}c}{\bar{n}\pi\Delta\nu} = \frac{1}{\bar{n}\sqrt{2\pi}}l_c. \quad (5.92)$$

Using eq. (4.51) for the expression of $\mathcal{U}_{s,\mathcal{P}}(\boldsymbol{\rho}, \mathbf{r}_d; t)$, eq. (5.89) can be written as

$$\begin{aligned} P_{rs,F}(t) &= -\frac{1}{4\pi f_1} \exp(ik_0 l_2) \\ &\int d\mathbf{r}_d |\gamma(t'_{s,\mathcal{P}} - t'_{r,\mathcal{P}})| \exp(ik_0 n z_d) \exp(-\mu_s z_d) U_s(\mathbf{r}_d, t) \mathcal{V}(\mathbf{r}_d + \boldsymbol{\rho}_b) \\ &\int_{\infty} d\boldsymbol{\rho} t_{l1}(\boldsymbol{\rho}) \exp(ik_0(\frac{|\boldsymbol{\rho}|^2}{2l_2} - \frac{\boldsymbol{\rho} \cdot \boldsymbol{\rho}_d}{l_2})) U_{r,\mathcal{P}}^*(\boldsymbol{\rho}, t). \end{aligned} \quad (5.93)$$

Replacing the function $t_{l1}(\boldsymbol{\rho})$ by eq. (4.44), and $U_{r,\mathcal{P}}(\boldsymbol{\rho}, t)$ by eq. (4.56), the integral $\int d\boldsymbol{\rho} t_{l1}(\boldsymbol{\rho}) \exp(ik_0(\frac{|\boldsymbol{\rho}|^2}{2l_2} - \frac{\boldsymbol{\rho} \cdot \boldsymbol{\rho}_d}{l_2})) U_{r,\mathcal{P}}^*(\boldsymbol{\rho}, t)$ in eq. (5.93) can be written as

$$\begin{aligned} &\int d\boldsymbol{\rho} t_{l1}(\boldsymbol{\rho}) \exp(ik_0(\frac{|\boldsymbol{\rho}|^2}{2l_2} - \frac{\boldsymbol{\rho} \cdot \boldsymbol{\rho}_d}{l_2})) U_{r,\mathcal{P}}^*(\boldsymbol{\rho}, t) \\ &= (\alpha_r \mathcal{A}_0)^* \frac{w_0}{w(l_r)} \exp(-ik_0 f_1 - ik_0 l_{r0} + i(\omega' t + \phi(l_r))) \int d\boldsymbol{\rho} \text{cyl}(\frac{\boldsymbol{\rho}}{2a_1}) \\ &\exp(-ik_0 \frac{\boldsymbol{\rho} \cdot \boldsymbol{\rho}_d}{l_2}) \exp(-\frac{\rho^2}{w^2(l_r)}) \exp(-i\frac{k_0 \rho^2}{2R(l_r)}), \end{aligned} \quad (5.94)$$

where l_{r0} is given by eq. (4.59), and ω' is given by eq. (4.57). Assuming that the reference beam is collimated throughout the propagation, we will replace $w(l_r)$ in eq. (5.94) by w_0 , where w_0 is the beam width of the reference beam. Also, under the assumption of a collimated beam, we will approximate $\frac{1}{R(l_r)} \approx 0$. Then the quadratic

phase $\exp(-i\frac{k_0\rho^2}{2R(l_r)})$ in eq. (5.94) is simplified to be one. If we further assume that the radius of the focusing lens aperture is larger than the beam waist of the reference beam: $w_0 < a_1$, then the beam width is the equivalent limiting aperture and we will simply let the lens aperture function $cyl(\frac{\rho}{2a_1})$ equal to one in the integral. Then eq. (5.94) can be written as

$$\begin{aligned} & \int d\boldsymbol{\rho} t_{l_1}(\boldsymbol{\rho}) \exp(ik_0(\frac{|\boldsymbol{\rho}|^2}{2l_2} - \frac{\boldsymbol{\rho} \cdot \boldsymbol{\rho}_d}{l_2})) U_{r,\mathcal{P}}^*(\boldsymbol{\rho}, t) \\ & \approx (\alpha_r \mathcal{A}_0)^* \exp(-ik_0 f_1 - ik_0 l_{r0} + i(\omega' t + \phi(l_r))) \\ & \int d\boldsymbol{\rho} \exp(-ik_0 \frac{\boldsymbol{\rho} \cdot \boldsymbol{\rho}_d}{l_2}) \exp(-\frac{\rho^2}{w_0^2}). \end{aligned} \quad (5.95)$$

The integral in eq. (5.95) can be evaluated as

$$\begin{aligned} & \int d\boldsymbol{\rho} \exp(-ik_0 \frac{\boldsymbol{\rho} \cdot \boldsymbol{\rho}_d}{l_2}) \exp(-\frac{\rho^2}{w_0^2}) \\ & \approx \pi w_0^2 \exp(-\pi^2 w_0^2 \frac{\rho_d^2}{(\lambda_0 f_1)^2}) = \pi w_0^2 \exp(-\frac{\rho_d^2}{w_{0s}^2}), \end{aligned} \quad (5.96)$$

where we have use the relationship:

$$w_{0s} = \frac{\lambda_0 f_1}{\pi w_0}, \quad (5.97)$$

with w_{0s} the beam waist of the sample beam at the focal plane. Using the result in eq. (5.96), eq. (5.94) can be written as

$$\begin{aligned} & \int d\boldsymbol{\rho} t_{l_1}(\boldsymbol{\rho}) \exp(ik_0(\frac{|\boldsymbol{\rho}|^2}{2l_2} - \frac{\boldsymbol{\rho} \cdot \boldsymbol{\rho}_d}{l_2})) U_{r,\mathcal{P}}^*(\boldsymbol{\rho}, t) \\ & = (\alpha_r \mathcal{A}_0)^* \exp(-ik_0 f_1 - ik_0 l_{r0} + i(\omega' t + \phi(l_r))) \pi w_0^2 \exp(-\frac{\rho_d^2}{w_{0s}^2}). \end{aligned} \quad (5.98)$$

Substituting eq. (5.98) into eq. (5.93), then $P_{rs,F}(t)$ can be written as

$$\begin{aligned} P_{rs,F}(t) & = -\frac{1}{4\pi f_1} (\alpha_r \mathcal{A}_0)^* \pi w_0^2 \exp(-ik_0 l_{r0}) \exp(+i\omega' t + i\phi(l_r)) \\ & \int d\mathbf{r}_d |\gamma(t'_{s,\mathcal{P}} - t'_{r,\mathcal{P}})| \exp(ik_0 n z_d) \exp(-\mu_s z_d) \exp(-\frac{\rho_d^2}{w_{0s}^2}) \\ & U_s(\mathbf{r}_d, t) \mathcal{V}(\mathbf{r}_d + \boldsymbol{\rho}_b), \end{aligned} \quad (5.99)$$

where $U_s(\mathbf{r}_d, t)$ is a Gaussian beam as shown in eq. (4.37):

$$\begin{aligned}
U_s(\mathbf{r}_d, t) = & \alpha_s \mathcal{A}_s \frac{w_{0s}}{w_s(l_d, t)} \exp\left(-\frac{\rho_d^2}{w_s^2(l_d, t)}\right) \exp[i(k_0(l_0 + l_1 + l_2) - \omega_0 t)] \\
& \exp(ikz_d) \exp\left[i\left(\frac{k\rho_d^2}{2R_s(l_d, t)} - \phi(l_d, t)\right)\right], \tag{5.100}
\end{aligned}$$

In OCT imaging, due to the coherent gating effect, only a thin slab of width l_c (correlation length of the source) centered around the scanning depth will contribute to the interferometric optical power. As discussed in chapter 4, with dynamic focusing, this scanning depth coincides with the focal plane of the focusing lens. In other words, only a thin slab centered around the focal plane will contribute to the interferometric optical power. In this analysis, it is assumed that the Rayleigh length of the sample beam (z_{0s}) is larger than the source correlation length (l_c). Therefore, inside the contributing layer, the sample beam can be assumed to possess a constant beam width ($w(l_d, t) = w_{0s}$) and a flat wavefront ($\frac{1}{R(l_d, t)} = 0$). Then eq. (5.100) can be simplified as

$$\begin{aligned}
U_s(\mathbf{r}_d, t) = & \alpha_s \mathcal{A}_s \exp\left(-\frac{\rho_d^2}{w_{0s}^2}\right) \exp[i(k_0(l_0 + l_1 + l_2) - \omega_0 t)] \\
& \exp(ikz_d) \exp[-i\phi(l_d, t)]. \tag{5.101}
\end{aligned}$$

Using eqs. (5.91) for the degree of temporal coherence, and 5.101), eq. (5.99) can be rewritten as

$$\begin{aligned}
P_{rs,F}(t) = & -\frac{1}{4\pi f_1} (\alpha_r \mathcal{A}_0)^* \alpha_s \mathcal{A}_s \pi w_0^2 \exp(-ik_0 f_1) \exp(-i\omega_D t + i\phi(l_r)) \\
& \int d\mathbf{r}_d \exp\left[-\frac{1}{\sigma^2} \left(\frac{v_a t}{n} - z_d\right)^2\right] \exp(i2k_0 \bar{n} z_d - i\phi(l_d, t)) \\
& \exp(-\mu_s z_d) \mathcal{V}(\mathbf{r}_d + \boldsymbol{\rho}_b) \exp\left(-\frac{2\rho_d^2}{w_{0s}^2}\right), \tag{5.102}
\end{aligned}$$

where ω_D is the change in the angular frequency of the reference beam due to Doppler effect (see eq. (4.58)). As shown in §4.2.4 (Data Acquisition), when there is no external modulation, ω_D equals to the modulation angular frequency of the OCT system (ω_m).

Second Moments of $P_{rs,F}(t)$ Using eq. (5.102), the term $\langle P_{rs,F}(t_1)P_{rs,F}^*(t_2) \rangle_M$ can be written as

$$\begin{aligned}
& \langle P_{rs,F}(t_1)P_{rs,F}^*(t_2) \rangle_M \\
&= \left(\frac{1}{2\pi f_1} P_0 |\alpha_r^* \alpha_s| \frac{w_0}{w_{0s}}\right)^2 \exp(-i\omega_D(t_1 - t_2)) \exp(+i\phi(l_{r1}) - i\phi(l_{r2})) \\
&\quad \int d\mathbf{r}_{d1} \int d\mathbf{r}_{d2} \exp(-\mu_s(z_{d1} + z_{d2})) \exp(i(2k_0\bar{n}(z_{d1} - z_{d2}) - (\phi_{s1} - \phi_{s2}))) \\
&\quad \exp[-\frac{1}{\sigma^2}(\frac{v_a t_1}{\bar{n}} - z_{d1})^2] \exp[-\frac{1}{\sigma^2}(\frac{v_a t_2}{\bar{n}} - z_{d2})^2] \\
&\quad \exp(-\frac{2}{w_{0s}^2}(\rho_{d1}^2 + \rho_{d2}^2)) K_{\mathcal{V}}(\mathbf{r}_{d1} + \boldsymbol{\rho}_{b1}, \mathbf{r}_{d2} + \boldsymbol{\rho}_{b2}), \tag{5.103}
\end{aligned}$$

where

$$K_{\mathcal{V}}(\mathbf{r}_{d1} + \boldsymbol{\rho}_{b1}, \mathbf{r}_{d2} + \boldsymbol{\rho}_{b2}) = \langle \mathcal{V}(\mathbf{r}_{d2} + \boldsymbol{\rho}_{b2}) \mathcal{V}(\mathbf{r}_{d1} + \boldsymbol{\rho}_{b1}) \rangle_M, \tag{5.104}$$

the correlation of the scattering potential. In eq. (5.103), we have used eq. (4.38) to replace the field amplitudes (\mathcal{A}_s and \mathcal{A}_0) by the optical power of the source (P_0). Assuming that $\phi(l_{r1}) \approx \phi(l_{r2})$, then eq. (5.103) can be written as

$$\begin{aligned}
& \langle P_{rs,F}(t_1)P_{rs,F}^*(t_2) \rangle_M \\
&= \left(\frac{1}{2\pi f_1} P_0 |\alpha_r^* \alpha_s| \frac{w_0}{w_{0s}}\right)^2 \exp(-i\omega_D(t_1 - t_2)) \\
&\quad \int d\mathbf{r}_{d1} \int d\mathbf{r}_{d2} \exp(-\mu_s(z_{d1} + z_{d2})) \\
&\quad \exp[-\frac{1}{\sigma^2}(\frac{v_a t_1}{\bar{n}} - z_{d1})^2] \exp[-\frac{1}{\sigma^2}(\frac{v_a t_2}{\bar{n}} - z_{d2})^2] \\
&\quad \exp(i(2k_0\bar{n}(z_{d1} - z_{d2}) - (\phi_{s1} - \phi_{s2}))) \\
&\quad \exp(-\frac{2}{w_{0s}^2}(\rho_{d1}^2 + \rho_{d2}^2)) K_{\mathcal{V}}(\mathbf{r}_{d1} + \boldsymbol{\rho}_{b1}, \mathbf{r}_{d2} + \boldsymbol{\rho}_{b2}), \tag{5.105}
\end{aligned}$$

Similarly, $\langle P_{rs,F}(t_1)P_{rs,F}(t_2) \rangle_M$ can be written as

$$\begin{aligned}
& \langle P_{rs,F}(t_1)P_{rs,F}(t_2) \rangle_M \\
&= \left(\frac{1}{2\pi f_1} P_0 \alpha_r^* \alpha_s \frac{w_0}{w_{0s}} \right)^2 \exp(-i2k_0 f_1) \exp(-i\omega_D(t_1 + t_2)) \\
& \quad \int d\mathbf{r}_{d1} \int d\mathbf{r}_{d2} \exp(-\mu_s(z_{d1} + z_{d2})) \\
& \quad \exp\left[-\frac{1}{\sigma^2} \left(\frac{v_a t_1}{\bar{n}} - z_{d1} \right)^2\right] \exp\left[-\frac{1}{\sigma^2} \left(\frac{v_a t_2}{\bar{n}} - z_{d2} \right)^2\right] \\
& \quad \exp(i(2k_0 \bar{n}(z_{d1} + z_{d2}) - (\phi_{s1} + \phi_{s2}))) \\
& \quad \exp\left(-\frac{2}{w_{0s}^2} (\rho_{d1}^2 + \rho_{d2}^2)\right) K_V(\mathbf{r}_{d1} + \boldsymbol{\rho}_{b1}, \mathbf{r}_{d2} + \boldsymbol{\rho}_{b2}). \tag{5.106}
\end{aligned}$$

Up to this point, we have developed the tools needed to assess the performance of an OCT modality in a detection task. In chapter 2, we derived an expression for a quadratic observer utilizing the covariance of a random field. In chapter 3, we presented different approximations for the study of stochastic field. Especially, we have introduced the concept of "First order multiple scattering approximation" that was applied in chapter 4 for the analysis of the backscattered field from the sample. In chapter 4, we adopted a system approach and derived an expression of the demodulated OCT data stream. In this chapter, we discussed the different sources of randomness in the OCT imaging modality, and the contribution of each source to the covariance function of the OCT data stream. In chapter 6, we will use the tools developed to analyze the performance of an OCT imaging modality in detecting abnormalities.

Chapter 6

TISSUE OPTICS AND NANOPARTICLE AIDED OCT IMAGING

Tissue optics studies light and tissue interaction, including the absorption, scattering, reflection and transmission of light through a biological tissue. It is a field of growing interest for its role in biomedical diagnostics and light dosimetry in photo-therapy. In the following sections, we will first give an overview of the bulk optical parameters used for the description of biological tissues. Then we will introduce the idea of using nanoparticle as a contrast agent in OCT imaging. Finally, we will present the result of a numerical study of the performance of OCT in detecting an abnormality in biological tissue using nanoparticles as contrast agents.

6.1 Optical Properties of Biological Tissues

With its high resolution, high sensitivity, non-invasiveness, optical methods have become important diagnostic and measurement tools for biotechnology and basic research in life science in the last decade. One of the biggest concerns in utilizing radiation to a biological system is the acceptable dosage of radiation to which a patient can be exposed without causing any harm. Therefore, there is an interest in developing more accurate theoretical predictive models on light-tissue interactions such as absorption, reflection and transmission of light by tissue, as well as fluence rates inside a tissue. The accuracy of such models depends greatly on the parameters used to describe the optical properties of tissues in the models. These parameters include the absorption and scattering coefficients, and the scattering anisotropy factor of a tissue. To obtain these parameters, observable quantities such as the reflection and transmission by a particular biological tissue will first be collected. Then the

measurements are analyzed and converted into the desired parameters according to light transport theory (e.g., diffusion theory, an approximation to radiative transport theory). Variations in measurement techniques as well as assumptions in the analysis of the measurements will highly affect the outcome of the resulting parameters. Therefore, it is a complex process to obtain optical parameters for different tissue types and more effort is needed before more accurate predictive models for tissue-light interactions can be developed.

In the following sections, we will give an introduction to the basic parameters that describe the optical properties of a biological tissue.

6.1.1 Absorption

Absorption of a sample is described by the absorption coefficient

$$\mu_a = \rho_a \sigma_a, \quad (6.1)$$

where ρ_a is the density of the entity constituting the sample, and σ_a the absorption cross section. We have assumed a single constituent for the sample in eq. (6.1). In biological tissue, however, there will be different constituents such as cells and intracellular materials. Then the total absorption will be the summation of all the different constituents. In the case where the geometrical area A of the entity in the sample is well defined (for example, spheres), the absorption cross section can be written as

$$\sigma_a = Q_a A \quad (6.2)$$

where Q_a is the absorption efficiency, which can be calculated by Mie theory for simple geometrical shape (for example, spheres) of the entity.

Absorption in tissue is dominated by protein and DNA in the ultra-violet range, by water in the infrared range, and by hemoglobin and melanin in the visible range. Absorption of light in biological tissues is significantly lower for the NIR (Near Infrared)

range, which is between 800nm and 1300nm and is called the diagnostic and therapeutic window. Within this window, absorption by biological tissues is negligible when compared to the effect of scattering. For example, the absorption coefficient for female breast tissue is $0.099 \pm 0.028 \text{ cm}^{-1}$ (at 980nm), while the scattering coefficient is $11.7 \pm 2.6 \text{ cm}^{-1}$ [88].

6.1.2 Scattering

Optical propagation in biological materials is dominated by scattering because of the inhomogeneities in biological tissue. The strength of the scattering is described the scattering coefficient

$$\mu_s = \rho_s \sigma_s, \quad (6.3)$$

where ρ_s is the density of the particles causing scatterings in the tissue, and σ_s the scattering cross section:

$$\sigma_s = Q_s A \quad (6.4)$$

Similar to the discussion for absorption, Q_s is the scattering efficiency, which can be calculated using Mie theory for simple geometrical shape, and A is the geometrical area of the particle. There are different types of scattering: elastic and inelastic scattering. Examples of elastic scattering include Rayleigh and Mie scattering, in which the photon energy does not change. Rayleigh scattering accounts for scattering caused by particles smaller than a wavelength of the incident radiation, and gives rise to an isotropic scattering pattern. Mie scattering corresponds to scattering caused by particles that are larger than a wavelength, and the scattering pattern is anisotropic. Raman scattering is an example of inelastic scattering, in which molecular vibration or rotation is excited due to the light-media interaction, and the scattered photon will have a wavelength different from the incident photon.

The total attenuation in the biological tissue is described by the total attenuation

coefficient μ_t , which is the sum of the scattering and absorption coefficients:

$$\mu_t = \mu_s + \mu_a. \quad (6.5)$$

For a single particle, the ratio between the scattering and total attenuation coefficient is defined as the albedo of the particle:

$$W_0 = \frac{\mu_s}{\mu_s + \mu_a}. \quad (6.6)$$

6.1.3 Anisotropy and Reduced Scattering Coefficient

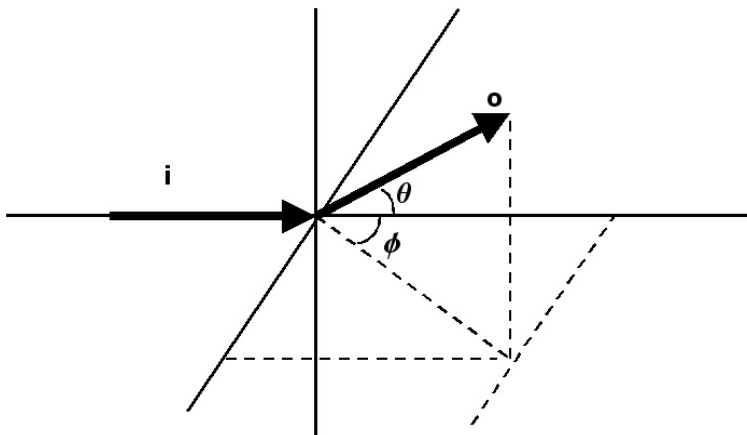


FIGURE 6.1. Geometry of the incident and scattered directions.

In a biological tissue, scattering is mostly in the forward direction, instead of being isotropic. An anisotropy parameter g is devised to describe this property. Let θ be the angle between the incident (\hat{i}) and scattered direction (\hat{o}) (see figure 6.1). The anisotropy parameter g is defined as the mean of $\cos \theta$

$$\begin{aligned} g &= \langle \hat{i} \cdot \hat{o} \rangle \\ &= \int_{4\pi} \cos \theta p(\hat{i}, \hat{o}) d\Omega, \end{aligned} \quad (6.7)$$

where $p(\hat{i} \cdot \hat{o})$ is the phase function that describes the angular distribution for a single scattering event, and

$$\int_{4\pi} p(\hat{i}, \hat{o}) d\Omega = 1. \quad (6.8)$$

Therefore, in essence, the phase function is the probability density function for scattering from direction \hat{i} to \hat{o} . For totally forward scattering, $g = 1$; totally backward scattering, $g = -1$; and $g = 0$ for isotropic scattering. The value of g ranges between 0.7 – 0.95 for most biological tissue.

In many cases, the exact scattering properties of the particles are unknown. Therefore, the phase function $p(\hat{i}, \hat{o})$, which contains the information of the angular distribution of the scattering events, is usually described in a heuristic way by a parametrized function. The Henyey-Greenstein function, which was first used in astrophysics to model the forward Mie scattering, is a widely used phase function:

$$p_{GH}(\theta) = \frac{1}{4\pi} \frac{1 - g^2}{(1 + g - 2g \cos \theta)^{3/2}}. \quad (6.9)$$

Different phase function exists. For example, in [89], Van Gemert et al. proposed a different phase function to describe a situation where a strongly forward scattering coexists with an isotropic scattering term :

$$p(\theta) \propto [2g\delta(1 - \cos \theta) + (1 - g)], \quad (6.10)$$

where the first term corresponds to the strongly forward peaked scattering and the second term the isotropic scattering. Eqs. (6.9 and 6.10) are identical in their first two moments.

Using the anisotropy parameter g , a reduced scattering coefficient can be defined as

$$\mu'_s = \mu_s(1 - g), \quad (6.11)$$

which is used to describe light propagation in diffusive scattering media (such as biological tissue). In a strongly forward scattering media (i.e. $g \approx 1$), the amount

of radiation energy can be transported through the media is larger than that of a media with the same scattering coefficient but scattering in a more isotropic manner (i.e. $g \approx 0$), since in the latter case more energy will be scattered in directions other than the forward direction. The inverse of μ'_s corresponds to the effective mean free path between the artificial isotropic scattering events in an intrinsically anisotropic environment. In the diffusive approximation of radiative transport theory, one can equivalently replace an anisotropic media with scattering coefficient μ_s and anisotropic parameter $g \neq 0$ by an isotropic scattering media with μ'_s and $g = 0$ [90].

6.2 Optical Molecular Imaging and Contrast Agents

Molecular imaging is the detection of a molecularly specific signal, either from a targeted exogenous agent or some endogenous molecule, in a living organism. In molecular imaging, probes known as biomarkers functionalized and designed to target specific cellular and molecular sites are used to enhance the imaging of various molecular or subcellular targets or pathways. Biomarkers interact chemically with the targeted surroundings and thus highlight the area where molecular changes occur. This ability to image with specificity at molecular and cellular level allows physicians to monitor the subtle changes happening in a pre-disease state, and thus opens up the possibilities of early detection and treatment of disease, more efficient pharmaceutical development, and even imaging of gene expression.

Optical imaging, with its high resolution, wavelength sensitivity, non-invasiveness and reduced health hazard to biological cells compared to ionizing radiation, is gaining a lot of interest in biomedical imaging. While the use of a contrast agent in nuclear imaging is routine, such use in optical biomedical imaging is still in its infancy. In recent years, optical probes such as bioluminescent and fluorescent agents have been developed to enhance contrast of the signatures of disease or abnormalities in tissues based on the detection of fluorescent light emission. However, such fluo-

rescent based contrast agents will not be applicable to coherent imaging modalities such as OCT or reflectance confocal microscopy, which obtain images through scattering or absorption of light in tissues. Therefore, there is a heightened interest in developing nonfluorescent and nonbioluminescent molecular imaging probes that will benefit coherent optical molecular imaging modalities.

6.2.1 Contrast Agents for OCT

OCT forms its image by detecting elastically scattered light which maintains the coherence of the incident light. Therefore, contrast agents for OCT must be materials that can alter the fundamental optical properties such as the scattering coefficient of the tissue. Such scattering probes function by introducing a local change of the index of refraction in the tissue. To achieve high scattering efficiency, most of the scattering probes consist of metals or other materials with an index significantly different from the tissue. Currently, there are two types of scattering probes used in OCT imaging: micro-spheres and nanoparticles.

Protein-based micro-spheres usually have a dimension between 2 to 5 microns. Their sizes prohibit them from being used in cell imaging. However, the relatively large size enables them to be used as a drug delivery vehicle by encapsulating drugs that can be delivered to specific sites [91]. On the other hand, with a submicron size ($\sim 100nm$), nanoparticle are a possible candidate as contrast agent for cell imaging. Lin et al. [92] have analyzed the optical properties of a class of coreshell nanoparticles with gold nanoshells and dielectric cores as contrast agents for early cancer detection. They studied a series of gold nanoshells of different core and shell sizes that are fabricated to scatter and/or absorb light with cross sections often several times larger than the geometric cross section. Sokolov et al. demonstrated the detection of precancerous cells using confocal reflectance imaging with gold nanoparticles [93].

As mentioned in the introduction (chapter 1) of this dissertation, it is important

to demonstrate the ability of contrast agents in improving clinical diagnosis. In the following sections, we will use the statistical tools developed in the previous chapters to analyze the ability of a contrast-agent-aided OCT modality in detecting abnormalities in biological tissues. We will also address the question of the required concentrations for the contrast agents to achieve a certain level of detectability.

6.3 Detection of an Abnormality in Biological Tissue Using Contrast Agent

6.3.1 Detection Task: Statement of the Hypothesis

We will consider a situation in which nanoparticles are injected into the host tissue for detection of an abnormality in the tissue. There are two possibilities:

1. If there is no abnormality, the nanoparticles will distribute uniformly within the host tissue. We will refer to this as the signal absent state (H_0).
2. If there is an abnormality, the nanoparticles will be drawn to the abnormal site and the local distribution of the nanoparticles will be denser. We will refer to this as the signal present state (H_1).

Mathematically, these two hypothesis can be represented as followings:

$$H_0 \text{ (signal absent) : } \quad \Upsilon_{NP,0}(\mathbf{r}) = D_0, \quad (6.12)$$

and

$$H_1 \text{ (signal present) : } \quad \Upsilon_{NP,1}(\mathbf{r}) = \Upsilon_{NP,0}(\mathbf{r}) + \delta\Upsilon_{NP}(\mathbf{r}). \quad (6.13)$$

In eq. (6.12), the function $\Upsilon_{NP,0}$ describes the number density of the nanoparticles for hypothesis H_0 . For the signal absent state, $\Upsilon_{NP,0}$ is a constant (D_0). In eq. (6.13), $\Upsilon_{NP,1}(\mathbf{r})$ describes the number density of the nanoparticles for hypothesis H_1 . The function $\delta\Upsilon_{NP}(\mathbf{r})$ describes the spatial change in the number density of the

nanoparticles due to the presence of the abnormality. We will further assume that the function $\delta\Upsilon_{NP}(\mathbf{r})$ has the form of a localized Gaussian function:

$$\delta\Upsilon_{NP}(\mathbf{r}) = \eta D_0 \exp\left[-\frac{|\boldsymbol{\rho} - \boldsymbol{\rho}_c|^2}{\sigma_\rho^2}\right] \exp\left[-\frac{|z - z_c|^2}{\sigma_z^2}\right], \quad (6.14)$$

where η is the fractional change in the number density at the abnormal site. At the center of the abnormality $(z_c, \boldsymbol{\rho}_c)$, the number density of the nanoparticles is increased by an amount of ηD_0 . It trails off with a Gaussian profile as it is further away from the center $(z_c, \boldsymbol{\rho}_c)$. The full-widths of the abnormality are approximately $2\sigma_\rho$ in the radial direction and $2\sigma_z$ in the axial direction. Using eq. (6.14), the signal present hypothesis (H_1 , eq. (6.13)) can be written as

$$H_1 : \quad \Upsilon_{NP,1}(\mathbf{r}) = D_0 + \eta D_0 \exp\left[-\frac{|\boldsymbol{\rho} - \boldsymbol{\rho}_c|^2}{\sigma_\rho^2}\right] \exp\left[-\frac{|z - z_c|^2}{\sigma_z^2}\right]. \quad (6.15)$$

The quantity $\Upsilon_{NP,1}(\mathbf{r})$ as described in eq. (6.15) is deterministic. This means that we are assuming a signal known exactly (SKE) detection task, in which we have all the information for the target/abnormality. We assume that we have knowledge of the location, the shape, and the contrast (described by the fractional change parameter η) of the target/abnormality. SKE detection is simplest in all the possible detection tasks, and it serves as a good starting point for investigations of more complex tasks that may involve uncertainties in locations or shapes, etc..

6.3.2 Scattering Potential Description of the Nanoparticle Contrast Agents

In this section, we will use the concepts developed in §5.2.2 (Stochastic Object Model) to describe the scattering potential of the nanoparticles, and derive an expression for the covariance function of the corresponding scattering potential.

As shown in eq. (5.30), the permittivity field of a random medium can be written as

$$\varepsilon(\mathbf{r}) = \sum_{n=1}^N \xi_n g(\mathbf{r}, \mathbf{r}_n). \quad (6.16)$$

We will describe the nanoparticles as point scatterers, and approximate the lump function $g(\mathbf{r}, \mathbf{r}_n)$ by a shift-invariant infinitesimal Gaussian lump with its width approaching zero:

$$g(\mathbf{r}, \mathbf{r}_n) = \exp(-\pi \frac{|\mathbf{r} - \mathbf{r}_n|^2}{\sigma_g^2}) \longrightarrow \sigma_g^3 \delta(\mathbf{r} - \mathbf{r}_n),$$

where $\sigma_g \rightarrow 0$. Then eq. (6.16) can be written as

$$\varepsilon(\mathbf{r}) = \sum_{n=1}^N \xi'_n \delta(\mathbf{r} - \mathbf{r}_n),$$

where $\xi'_n = \sigma_g^3 \xi_n$ is assumed to be finite. Under this point scatterer approximation, the first and second moments of the permittivity field, when conditioned on a particular realization of the probability density function $W_g(\vec{r})$ describing the spatial distribution of the nanoparticles, can be written as (see eqs. (5.37 to 5.41)):

$$A_{\varepsilon|W_g}(\mathbf{r}) = \bar{N} \langle \xi' \rangle W_g(\mathbf{r}), \quad (6.17)$$

and

$$\begin{aligned} B_{\varepsilon|W_g}(\mathbf{r}_1, \mathbf{r}_2) \\ = \bar{N} \langle \xi'^2 \rangle W_g(\mathbf{r}_1) \delta_g(\mathbf{r}_1 - \mathbf{r}_2) + \bar{N}^2 \langle \xi' \rangle^2 W_g(\mathbf{r}_1) W_g(\mathbf{r}_2). \end{aligned} \quad (6.18)$$

Then, using eqs. (5.36, 6.17, and 6.18), the covariance of the permittivity field for the nanoparticles can be written as

$$\begin{aligned} K_{\varepsilon}(\mathbf{r}_1, \mathbf{r}_2) &= \langle \xi'^2 \rangle \langle \bar{N} W_g(\mathbf{r}_1) \rangle_{W_g} \delta(\mathbf{r}_1 - \mathbf{r}_2) + \langle \xi' \rangle^2 \langle \bar{N}^2 W_g(\mathbf{r}_1) W_g(\mathbf{r}_2) \rangle_{W_g} \\ &\quad - \langle \xi' \rangle^2 \langle \bar{N} W_g(\mathbf{r}_1) \rangle_{W_g} \langle \bar{N} W_g(\mathbf{r}_2) \rangle_{W_g}. \end{aligned} \quad (6.19)$$

Using eq. (5.33) to rewrite $\bar{N} W_g(\mathbf{r})$ as $\Upsilon_{NP}(\mathbf{r})$, eq. (6.19) can be written as

$$K_{\varepsilon}(\mathbf{r}_1, \mathbf{r}_2) = \langle \xi'^2 \rangle \langle \Upsilon_{NP}(\mathbf{r}_1) \rangle_{\Upsilon} \delta(\mathbf{r}_1 - \mathbf{r}_2) + K_{\Upsilon}(\mathbf{r}_1, \mathbf{r}_2), \quad (6.20)$$

where

$$\begin{aligned} K_{\Upsilon}(\mathbf{r}_1, \mathbf{r}_2) &= \langle \xi' \rangle^2 \langle \Upsilon_{NP}(\mathbf{r}_1) \Upsilon_{NP}(\mathbf{r}_2) \rangle_{\Upsilon} \\ &\quad - \langle \xi' \rangle^2 \langle \Upsilon_{NP}(\mathbf{r}_1) \rangle_{\Upsilon} \langle \Upsilon_{NP}(\mathbf{r}_2) \rangle_{\Upsilon}. \end{aligned} \quad (6.21)$$

For signal-known-exactly detection task, the number density function of the nanoparticles $\Upsilon_{NP}(\mathbf{r})$ is deterministic. Therefore, $K_{\Upsilon}(\mathbf{r}_1, \mathbf{r}_2) = 0$ and eq. (6.20) reduces to

$$K_{\varepsilon}(\mathbf{r}_1, \mathbf{r}_2) = \langle \xi'^2 \rangle \Upsilon_{NP}(\mathbf{r}_1) \delta(\mathbf{r}_1 - \mathbf{r}_2). \quad (6.22)$$

Backscattering and Attenuation Coefficients for Point Scatterers

The per unit volume backscattering coefficient for a random medium can be written as (see eq. (5.56))

$$\sigma_b = k^4 \frac{1}{4\pi} \frac{1}{n^4} \mathcal{F}\{K_{\varepsilon}(\mathbf{r}_-)\}|_{k_s=2k_0}. \quad (6.23)$$

As shown in eq. (6.22), for the point scatterer model, $K_{\varepsilon}(\mathbf{r}_1, \mathbf{r}_2)$ is delta correlated. For a uniform number density function, $\Upsilon(\mathbf{r}) = D$, then

$$\mathcal{F}\{K_{\varepsilon}(\mathbf{r}_-)\} = \langle \xi'^2 \rangle D, \quad (6.24)$$

and the per unit volume backscattering cross section in eq. (6.23) can be written as

$$\sigma_b = k_0^4 \frac{1}{4\pi} \langle \xi'^2 \rangle D. \quad (6.25)$$

Using eq. (5.55), the per unit volume differential cross section $\sigma(\widehat{o}, \widehat{i})$ can be written as

$$\sigma(\widehat{o}, \widehat{i}) = \frac{1}{4\pi} \sigma_b = k_0^4 \left(\frac{1}{4\pi} \right)^2 \langle \xi'^2 \rangle D, \quad (6.26)$$

which is constant over all the possible angles. Then, using eq. (5.57), it can be shown that

$$\mu_s = \sigma_b. \quad (6.27)$$

In the next few sections, we will derive the covariance function of the OCT data under the point scatterer model.

6.3.3 Covariance Function of the OCT Data for the Detection Task

As shown in Chapter 5, the covariance function of the demodulated OCT data can be broken down into the contributions from the shot noise term and the scattering

noise term (see eq. (5.70)):

$$K_s(t_1, t_2) = K_{shot}(t_1, t_2) + K_{scat}(t_1, t_2).$$

We will first evaluate the shot noise contribution, then the scattering noise contribution to the covariance in the coming sections.

Shot Noise Contribution

As shown in eq. (5.79), the shot noise contribution can be written as

$$K_{shot}(t_1, t_2) = \frac{(\zeta e)^2}{h\nu_0} \frac{1}{2} \int dx \langle P_{DC}(x) \rangle_{F,M} \psi_{Meyer}(t_1, x) \psi_{Meyer}(t_2, x). \quad (6.28)$$

Using eq. (4.64), $\langle P_{DC}(t) \rangle_{F,M}$ can be written as

$$\langle P_{DC}(t) \rangle_{F,M} = \langle P_r(t) \rangle_{F,M} + \langle P_s(t) \rangle_{F,M}, \quad (6.29)$$

where $P_r(t)$ and $P_s(t)$ represent the optical power in the reference and sample beam respectively, and can be written as (see eqs. (4.66 and 4.67))

$$\langle P_r(t) \rangle_{F,M} = |\alpha_r|^2 P_0, \quad (6.30)$$

and

$$\begin{aligned} \langle P_s(t) \rangle_{F,M} &= \int d\boldsymbol{\rho} \int d\mathbf{r}_{d1} \int d\mathbf{r}_{d2} \mathcal{U}_{s,\mathcal{P}}(\boldsymbol{\rho}, \mathbf{r}_{d1}; t) \mathcal{U}_{s,\mathcal{P}}^*(\boldsymbol{\rho}, \mathbf{r}_{d2}; t) \\ \langle T(t'_{s,\mathcal{P}1}) T^*(t'_{s,\mathcal{P}2}) \rangle_F &< \mathcal{V}(\mathbf{r}_{d1} + \boldsymbol{\rho}_{bt}) \mathcal{V}(\mathbf{r}_{d2} + \boldsymbol{\rho}_{bt}) \rangle_M. \end{aligned} \quad (6.31)$$

Using eqs (5.24 and 6.22), $\langle \mathcal{V}(\mathbf{r}_1) \mathcal{V}(\mathbf{r}_2) \rangle_M$ can be written as

$$\langle \mathcal{V}(\mathbf{r}_1) \mathcal{V}(\mathbf{r}_2) \rangle_M = k_0^4 \langle \xi'^2 \rangle \Upsilon_{NP}(\mathbf{r}_1) \delta(\mathbf{r}_1 - \mathbf{r}_2). \quad (6.32)$$

Then eq. (6.31) can be written as

$$\begin{aligned} \langle P_s(t) \rangle_{F,M} &= k_0^4 \langle \xi'^2 \rangle \int d\boldsymbol{\rho} \int d\mathbf{r}_{d1} |\mathcal{U}_{s,\mathcal{P}}(\boldsymbol{\rho}, \mathbf{r}_{d1}; t)|^2 \\ \langle T(t'_{s,\mathcal{P}1}) T^*(t'_{s,\mathcal{P}1}) \rangle_F &< \Upsilon_{NP}(\mathbf{r}_{d1} + \boldsymbol{\rho}_{bt}). \end{aligned} \quad (6.33)$$

Since

$$\langle T(t'_{s,p_1})T^*(t'_{s,p_1}) \rangle_F = 1,$$

eq. (6.33) can be written as

$$\langle P_s(t) \rangle_{F,M} = k_0^4 \langle \xi'^2 \rangle \int d\mathbf{r}_{d1} \Upsilon_{NP}(\mathbf{r}_{d1} + \boldsymbol{\rho}_{bt}) \int d\boldsymbol{\rho} |\mathcal{U}_{s,\mathcal{P}}(\boldsymbol{\rho}, \mathbf{r}_{d1}; t)|^2. \quad (6.34)$$

Using eq. (4.51, 4.44, and 4.37), $|\mathcal{U}_{s,\mathcal{P}}(\boldsymbol{\rho}, \mathbf{r}_{d1}; t)|^2$ can be written as

$$\begin{aligned} |\mathcal{U}_{s,\mathcal{P}}(\boldsymbol{\rho}, \mathbf{r}_{d1}; t)|^2 &= \left(\frac{1}{4\pi f_1} \right)^2 \text{cyl}^2\left(\frac{\boldsymbol{\rho}}{2a_1}\right) \left| \alpha_s \mathcal{A}_s \frac{w_{0s}}{w(l_d, t)} \right|^2 \\ &\quad \exp(-2\mu_s z_{d1}) \exp\left(-\frac{2\rho_d^2}{w_s^2(l_d, t)}\right). \end{aligned} \quad (6.35)$$

Then eq. (6.34) can be written as

$$\begin{aligned} \langle P_s(t) \rangle_{F,M} &= \left(\frac{1}{4\pi f_1} \right)^2 k_0^4 \langle \xi'^2 \rangle |\alpha_s|^2 P_0 \frac{2}{\pi} \int d\boldsymbol{\rho} \text{cyl}\left(\frac{\boldsymbol{\rho}}{2a_1}\right) \\ &\quad \int d\mathbf{r}_{d1} \Upsilon_{NP}(\mathbf{r}_{d1} + \boldsymbol{\rho}_{bt}) \exp(-2\mu_s z_{d1}) \frac{1}{w_s^2(l_d, t)} \exp\left(-\frac{2\rho_d^2}{w_s^2(l_d, t)}\right). \end{aligned} \quad (6.36)$$

Since

$$\int d\boldsymbol{\rho} \text{cyl}\left(\frac{\boldsymbol{\rho}}{2a_1}\right) = \pi a_1^2,$$

eq. (6.36) can be rewritten as

$$\begin{aligned} \langle P_s(t) \rangle_{F,M} &= C_s \int d\mathbf{r}_{d1} \Upsilon(\mathbf{r}_{d1} + \boldsymbol{\rho}_{bt}) \exp(-2\mu_s z_{d1}) \\ &\quad \frac{1}{w^2(l_d, t)} \exp\left(-\frac{2\rho_d^2}{w^2(l_d, t)}\right), \end{aligned} \quad (6.37)$$

where

$$C_s = \frac{1}{8\pi^2} \left(\frac{a_1}{f_1}\right)^2 k_0^4 \langle \xi'^2 \rangle |\alpha_s|^2 P_0. \quad (6.38)$$

Signal Absent For the signal absent state, as shown in eq. (6.12), $\Upsilon_{NP,0}(\mathbf{r}) = D_0$.

Using eq. (6.37), the corresponding optical power can be written as

$$\begin{aligned} \langle P_s(t)|H_0 \rangle_{G,M} &= C_s D_0 \int dz_{d1} \exp(-2\mu_s z_{d1}) \frac{1}{w_s^2(l_d, t)} \\ &\quad \int d\boldsymbol{\rho}_{d1} \exp\left(-\frac{2\rho_d^2}{w_s^2(l_d, t)}\right). \end{aligned} \quad (6.39)$$

Since

$$\int d\boldsymbol{\rho}_{d1} \exp\left(-\frac{2\rho_d^2}{w_s^2(l_d, t)}\right) = \pi \frac{w_s^2(l_d, t)}{2},$$

then $\langle P_s(t)|H_0 \rangle_{G,M}$ can be written as

$$\langle P_s(t)|H_0 \rangle_{G,M} = C_s D_0 \frac{\pi}{2} \int dz_{d1} \exp(-2\mu_s z_{d1}). \quad (6.40)$$

Let d the thickness of the sample, then the last integral can be evaluated as

$$\int dz_{d1} \exp(-2\mu_s z_{d1}) = \frac{1}{2\mu_s} (1 - \exp(-2\mu_s d)).$$

Therefore, eq. (6.40) can be written as

$$\begin{aligned} & \langle P_s(t)|H_0 \rangle_{G,M} \\ &= C_s D_0 \frac{\pi}{2} \frac{1}{2\mu_s} (1 - \exp(-2\mu_s d)). \end{aligned}$$

Using eq. (6.38) for C_s , then $\langle P_s(t)|H_0 \rangle_{G,M}$ can be written as

$$\begin{aligned} & \langle P_s(t)|H_0 \rangle_{G,M} \\ &= \frac{1}{32\pi} |\alpha_s|^2 P_0 \left(\frac{a_1}{f_1}\right)^2 k_0^4 \langle \xi'^2 \rangle D_0 \frac{1}{\mu_s} (1 - \exp(-2\mu_s d)) \\ &= \frac{1}{8} |\alpha_s|^2 P_0 \left(\frac{a_1}{f_1}\right)^2 \sigma_{b0} \frac{1}{\mu_s} (1 - \exp(-2\mu_s d)), \end{aligned} \quad (6.41)$$

where (see eq. (6.25))

$$\sigma_{b0} = k_0^4 \frac{1}{4\pi} \langle \xi'^2 \rangle D_0. \quad (6.42)$$

Using eqs. (6.28, 6.29, 6.30, and 6.41) for the signal absent state, the shot noise contribution to the covariance function can be written as

$$\begin{aligned} K_{shot, H_0}(t, t) &= \frac{\zeta e P_0 \zeta e}{h\nu_0} \frac{1}{2} \int dx \psi_{Meyer}^2(t, x) \{ |\alpha_r|^2 + \\ & \frac{1}{8} |\alpha_s|^2 \left(\frac{a_1}{f_1}\right)^2 \sigma_{b0} \frac{1}{\mu_s} (1 - \exp(-2\mu_s d)) \}. \end{aligned} \quad (6.43)$$

Signal Present As shown in eq. (6.13), the number density of the scatterers for the signal present state can be written as

$$\Upsilon_{NP,1}(\mathbf{r}) = \Upsilon_{NP,0}(\mathbf{r}) + \delta\Upsilon_{NP}(\mathbf{r}).$$

Since the optical power from the sample beam is linear in the scatterer number density (see eq. (6.33)), the optical power of the sample beam for the signal present state can be written as the sum of the contributions from the background (signal absent state, $\langle P_s(t)|H_0 \rangle_{F,M}$) and that from the target/abnormality ($\langle \Delta P_s(t) \rangle_{F,M}$):

$$\langle P_s(t)|H_1 \rangle_{F,M} = \langle P_s(t)|H_0 \rangle_{F,M} + \langle \Delta P_s(t) \rangle_{F,M}. \quad (6.44)$$

The contribution from the target ($\langle \Delta P_s(t) \rangle_{F,M}$) can be evaluated by replacing $\Upsilon_{NP}(\mathbf{r}_{d1} + \boldsymbol{\rho}_{bt})$ by $\delta\Upsilon_{NP}(\mathbf{r}_{d1} + \boldsymbol{\rho}_{bt})$ in eq. (6.37):

$$\begin{aligned} \langle \Delta P_s(t) \rangle_{F,M} &= C_s \int d\mathbf{r}_{d1} \delta\Upsilon_{NP}(\mathbf{r}_{d1} + \boldsymbol{\rho}_{bt}) \exp(-2\mu_s z_{d1}) \\ &\quad \frac{1}{w_s^2(l_d, t)} \exp\left(-\frac{2\rho_d^2}{w_s^2(l_d, t)}\right). \end{aligned} \quad (6.45)$$

Using eq. (6.14) for $\delta\Upsilon_{NP}(\mathbf{r}_{d1} + \boldsymbol{\rho}_{bt})$, eq. (6.45) can be written as

$$\begin{aligned} \langle \Delta P_s(t) \rangle_{F,M} &= C_s \eta D_0 \int dz_{d1} \exp(-2\mu_s z_{d1}) \frac{1}{w_s^2(l_d, t)} \exp\left[-\frac{|z_{d1} - z_c|^2}{\sigma_z^2}\right] \\ &\quad \int d\boldsymbol{\rho}_{d1} \exp\left(-\frac{2\rho_d^2}{w_s^2(l_d, t)}\right) \exp\left[-\frac{|\boldsymbol{\rho}_{d1} + \boldsymbol{\rho}_{b1} - \boldsymbol{\rho}_c|^2}{\sigma_\rho^2}\right]. \end{aligned} \quad (6.46)$$

Assuming that the transverse scan is along the y -direction of the coordinate system at a speed v_l , the displacement of the beam center can be written as $\boldsymbol{\rho}_{b1} = v_l t_1 \hat{y}$.

Then the integral over $\boldsymbol{\rho}_{d1}$ in eq. (6.46) can be evaluated as

$$\begin{aligned} &\int d\boldsymbol{\rho}_{d1} \exp\left[-\frac{2}{w_s^2(z_{d1}, t)} \rho_{d1}^2\right] \exp\left[-\frac{|\boldsymbol{\rho}_{d1} + v_l t_1 \hat{y} - \boldsymbol{\rho}_c|^2}{\sigma_\rho^2}\right] \\ &= \pi \frac{w_s^2(z_{d1}, t) \sigma_\rho^2}{w_s^2(z_{d1}, t) + 2\sigma_\rho^2} \exp\left[-\frac{2}{w_s^2(z_{d1}, t) + 2\sigma_\rho^2} |v_l t_1 \hat{y} - \boldsymbol{\rho}_c|^2\right], \end{aligned}$$

and eq.(6.46) can be written as

$$\langle \Delta P_s(t) \rangle_{F,M} = C_s \eta D_0 \pi \sigma_\rho^2 \Omega_s(\mathbf{r}_c, \sigma_z, \sigma_\rho, z_{0s}, t), \quad (6.47)$$

in which we have introduced the short-hand notation $\Omega_s(\mathbf{r}_c, \sigma_z, \sigma_\rho, z_{0s}, t)$:

$$\begin{aligned} \Omega_s(\mathbf{r}_c, \sigma, z_{0s}, t) &= \int dz_{d1} \exp(-2\mu_s z_{d1}) \exp\left[-\frac{(z_{d1} - z_c)^2}{\sigma_z^2}\right] \\ &\quad \frac{1}{w_s^2(z_{d1}, t) + 2\sigma_\rho^2} \exp\left[-\frac{2}{w_s^2(z_{d1}, t) + 2\sigma_\rho^2} |vt\hat{y} - \boldsymbol{\rho}_c|^2\right]. \end{aligned} \quad (6.48)$$

Using eq. (6.38) and eq. (6.25), eq. (6.47) can be written as

$$\langle \Delta P_s(t) \rangle_{F,M} = \frac{1}{2} |\alpha_s|^2 P_0 \left(\frac{a_1}{f_1}\right)^2 \sigma_{b0} \eta \sigma_\rho^2 \Omega_s(\mathbf{r}_c, \sigma_z, \sigma_\rho, z_{0s}, t), \quad (6.49)$$

Then, by Using eqs. (6.44 and 6.49), the shot noise contribution for the signal present state can be written as

$$\begin{aligned} K_{shot,H_1}(t_1, t_2) &= K_{shot,H_0}(t_1, t_2) + \frac{(\zeta e)^2}{h\nu_0} \frac{1}{2} \\ &\quad \int dx \langle \Delta P_s(x) \rangle_{F,M} \psi_{Meyer}(t_1, x) \psi_{Meyer}(t_2, x) \\ &= K_{shot,H_0}(t_1, t_2) + \frac{|\alpha_s|^2 P_0 \zeta e}{h\nu_0} \frac{1}{4} \left(\frac{a_1}{f_1}\right)^2 \sigma_{b0} \eta \sigma_\rho^2 \\ &\quad \int dx \psi_{Meyer}(t_1, x) \psi_{Meyer}(t_2, x) \Omega_s(\mathbf{r}_c, \sigma_z, \sigma_\rho, z_{0s}, x). \end{aligned} \quad (6.50)$$

Scattering Noise Contribution

As shown in eq. (5.88), the contribution from the scattering process to the covariance matrix is

$$\begin{aligned} K_{scat}(t_1, t_2) &= \left(\frac{1}{h\nu_0}\right)^2 \int dx_1 \int dx_2 H_{Meyer}(t_1, x_1) H_{Meyer}(t_2, x_2) \\ &\quad \langle P_{rs,F}(x_1) P_{rs,F}(x_2) + P_{rs,F}(x_1) P_{rs,F}^*(x_2) + C.C. \rangle_M, \end{aligned} \quad (6.51)$$

where (see eq. (5.105) and eq. (5.106))

$$\begin{aligned}
\langle P_{rs,F}(t_1)P_{rs,F}^*(t_2) \rangle_M &= \left(\frac{1}{2\pi f_1} P_0 |\alpha_r^* \alpha_s| \frac{w_0}{w_{0s}}\right)^2 \exp(-i\omega_D(t_1 - t_2)) \\
&\int d\mathbf{r}_{d1} \int d\mathbf{r}_{d2} \exp(-\mu_s(z_{d1} + z_{d2})) \exp(i(2k_0\bar{n}(z_{d1} - z_{d2}) - (\phi_{s1} - \phi_{s2}))) \\
&\exp\left[-\frac{1}{\sigma^2}\left(\frac{v_a t_1}{\bar{n}} - z_{d1}\right)^2\right] \exp\left[-\frac{1}{\sigma^2}\left(\frac{v_a t_2}{\bar{n}} - z_{d2}\right)^2\right] \\
&\exp\left(-\frac{2}{w_{0s}^2}(\rho_{d1}^2 + \rho_{d2}^2)\right) K_{\mathcal{V}}(\mathbf{r}_{d1} + \boldsymbol{\rho}_{b1}, \mathbf{r}_{d2} + \boldsymbol{\rho}_{b2}), \tag{6.52}
\end{aligned}$$

and

$$\begin{aligned}
\langle P_{rs,F}(t_1)P_{rs,F}(t_2) \rangle_M &= \left(\frac{1}{2\pi f_1} P_0 \alpha_r^* \alpha_s \frac{w_0}{w_{0s}}\right)^2 \exp(-i2k_0 f_1) \exp(-i\omega_D(t_1 + t_2)) \\
&\int d\mathbf{r}_{d1} \int d\mathbf{r}_{d2} \exp(i(2k_0\bar{n}(z_{d1} + z_{d2}) - (\phi_{s1} + \phi_{s2}))) \exp(-\mu_s(z_{d1} + z_{d2})) \\
&\exp\left[-\frac{1}{\sigma^2}\left(\frac{v_a t_1}{\bar{n}} - z_{d1}\right)^2\right] \exp\left[-\frac{1}{\sigma^2}\left(\frac{v_a t_2}{\bar{n}} - z_{d2}\right)^2\right] \\
&\exp\left(-\frac{2}{w_{0s}^2}(\rho_{d1}^2 + \rho_{d2}^2)\right) K_{\mathcal{V}}(\mathbf{r}_{d1} + \boldsymbol{\rho}_{b1}, \mathbf{r}_{d2} + \boldsymbol{\rho}_{b2}). \tag{6.53}
\end{aligned}$$

For the detection task described in the previous section, the covariance function of the scattering potential can be written as (see eqs. (5.24 and 6.22))

$$K_{\mathcal{V}}(\mathbf{r}_{d1} + \boldsymbol{\rho}_{b1}, \mathbf{r}_{d2} + \boldsymbol{\rho}_{b2}) = k_0^4 \langle \xi'^2 \rangle \Upsilon_{NP}(\mathbf{r}_{d1} + \boldsymbol{\rho}_{b1}) \delta(\mathbf{r}_{d1} - \mathbf{r}_{d2} - \Delta\boldsymbol{\rho}_b),$$

where $\Delta\boldsymbol{\rho}_b = \boldsymbol{\rho}_{b2} - \boldsymbol{\rho}_{b1}$, the radial distance between the centers of the sample beam at times t_1 and t_2 . Then eqs. (6.52 and 6.53) can be rewritten as

$$\begin{aligned}
\langle P_{rs,F}(t_1)P_{rs,F}^*(t_2) \rangle_M &= C_{rs} \exp(-i\omega_D(t_1 - t_2)) \\
&\int d\mathbf{r}_{d1} \exp\left[-\frac{1}{\sigma^2}\left(\frac{v_a t_1}{\bar{n}} - z_{d1}\right)^2\right] \exp\left[-\frac{1}{\sigma^2}\left(\frac{v_a t_2}{\bar{n}} - z_{d1}\right)^2\right] \\
&\exp(-2\mu_s z_{d1}) \Upsilon(\mathbf{r}_{d1} + \boldsymbol{\rho}_{b1}) \exp\left(-\frac{2}{w_{0s}^2}(\rho_{d1}^2 + |\boldsymbol{\rho}_{d1} - \Delta\boldsymbol{\rho}_b|^2)\right), \tag{6.54}
\end{aligned}$$

and

$$\begin{aligned}
\langle P_{rs,F}(t_1)P_{rs,F}(t_2) \rangle_M &= C'_{rs} \exp(-i\omega_D(t_1 + t_2)) \int d\mathbf{r}_{d1} \exp(i4k_0\bar{n}z_{d1}) \\
&\exp\left[-\frac{1}{\sigma^2}\left(\frac{v_a t_1}{\bar{n}} - z_{d1}\right)^2\right] \exp\left[-\frac{1}{\sigma^2}\left(\frac{v_a t_2}{\bar{n}} - z_{d1}\right)^2\right] \exp(-2\mu_s z_{d1}) \\
&\exp\left(-\frac{2}{w_{0s}^2}(\rho_{d1}^2 + |\boldsymbol{\rho}_{d1} - \Delta\boldsymbol{\rho}_b|^2)\right) \Upsilon(\mathbf{r}_{d1} + \boldsymbol{\rho}_{b1}), \tag{6.55}
\end{aligned}$$

where

$$C_{rs} = k_0^4 \langle \xi'^2 \rangle \left(\frac{1}{2\pi f_1} P_0 |\alpha_r^* \alpha_s| \frac{w_0}{w_{0s}} \right)^2, \quad (6.56)$$

and

$$C'_{rs} = k_0^4 \langle \xi'^2 \rangle \left(\frac{1}{2\pi f_1} P_0 \alpha_r^* \alpha_s \frac{w_0}{w_{0s}} \right)^2 \exp(-i2k_0 f_1).$$

In eq. (6.55), the term $\exp(i4k_0 \bar{n} z_{d1})$ corresponds to a fast oscillation when compared to the scales defined by σ or w_{0s} . Therefore, the result of the integral will be nearly zero and the contributions from $\langle P_{rs,F}(t_1) P_{rs,F}(t_2) \rangle_M$ (and its complex conjugate) to the covariance function will be ignored. Then eq. (6.51) can be rewritten as

$$\begin{aligned} K_{scat}(t_1, t_2) &= \left(\frac{1}{h\nu_0} \right)^2 \int dx_1 \int dx_2 H_{Meyer}(t_1, x_1) H_{Meyer}(t_2, x_2) \\ &[\langle P_{rs,F}(t_1) P_{rs,F}^*(t_2) \rangle_M + C.C.], \end{aligned} \quad (6.57)$$

with $\langle P_{rs,F}(t_1) P_{rs,F}^*(t_2) \rangle_M$ given by eq. (6.54).

Signal absent For signal absent, the scatterer number density is a constant (see eq. (6.12)):

$$\Upsilon(\mathbf{r}) = \Upsilon_{NP,0}(\mathbf{r}) = D_0.$$

Plugging this into eq. (6.54), the two time correlation for the signal absent state can be written as

$$\begin{aligned} &\langle P_{rs,F}(x_1) P_{rs,F}^*(x_2) | H_0 \rangle_M = C_{rs} D_0 \exp(-i\omega_D(x_1 - x_2)) \\ &\int d\mathbf{r}_{d1} \exp\left[-\frac{1}{\sigma^2} \left(\frac{v_a x_1}{\bar{n}} - z_{d1} \right)^2\right] \exp\left[-\frac{1}{\sigma^2} \left(\frac{v_a x_2}{\bar{n}} - z_{d1} \right)^2\right] \\ &\exp(-2\mu_s z_{d1}) \exp\left(-\frac{2}{w_{0s}^2} (\rho_{d1}^2 + |\boldsymbol{\rho}_{d1} - \Delta\boldsymbol{\rho}_b|^2)\right). \end{aligned} \quad (6.58)$$

Since

$$\begin{aligned} &\exp\left[-\frac{1}{\sigma^2} \left(\frac{v_a x_1}{\bar{n}} - z_{d1} \right)^2\right] \exp\left[-\frac{1}{\sigma^2} \left(\frac{v_a x_2}{\bar{n}} - z_{d1} \right)^2\right] \\ &= \exp\left[-\frac{2}{\sigma^2} \left(z_{d1} - \frac{v_a x_1 + v_a x_2}{2\bar{n}} \right)^2\right] \exp\left[-\frac{1}{2\sigma^2} \left(\frac{v_a x_1 - v_a x_2}{\bar{n}} \right)^2\right], \end{aligned} \quad (6.59)$$

and

$$\int d\boldsymbol{\rho}_{d1} \exp\left(-\frac{2}{w_{0s}^2}(\rho_{d1}^2 + |\boldsymbol{\rho}_{d1} - \Delta\boldsymbol{\rho}_b|^2)\right) = \exp\left(-\frac{|\Delta\boldsymbol{\rho}_b|^2}{w_{0s}^2}\right)\left(\frac{\pi w_{0s}^2}{4}\right),$$

then eq. (6.58) can be written as

$$\begin{aligned} < P_{rs,F}(x_1)P_{rs,F}^*(x_2)|H_0 >_M = C_{rs}D_0 \exp\left(-\frac{|\Delta\boldsymbol{\rho}_b|^2}{w_{0s}^2}\right)\left(\frac{\pi w_{0s}^2}{4}\right) \\ & \exp(-i\omega_D(x_1 - x_2)) \exp\left[-\frac{1}{2\sigma^2}\left(\frac{v_ax_1 - v_ax_2}{\bar{n}}\right)^2\right] \\ & \int dz_{d1} \exp(-2\mu_s z_{d1}) \exp\left[-\frac{2}{\sigma^2}\left(z_{d1} - \frac{v_ax_1 + v_ax_2}{2\bar{n}}\right)^2\right]. \end{aligned} \quad (6.60)$$

Since the attenuation term $\exp(-2\mu_s z_{d1})$ will vary only slightly within the width σ , it is possible to approximate the integral over z_{d1} as

$$\begin{aligned} & \int dz_{d1} \exp(-2\mu_s z_{d1}) \exp\left[-\frac{2}{\sigma^2}\left(z_{d1} - \frac{v_ax_1 + v_ax_2}{2\bar{n}}\right)^2\right] \\ & \approx \exp\left(-2\mu_s \frac{v_ax_1 + v_ax_2}{2\bar{n}}\right) \sqrt{\frac{\pi}{2}}\sigma, \end{aligned}$$

and eq. (6.60) can be written as

$$\begin{aligned} < P_{rs,F}(x_1)P_{rs,F}^*(x_2)|H_0 >_M = C_{rs}D_0 \sqrt{\frac{\pi}{2}}\sigma \left(\frac{\pi w_{0s}^2}{4}\right) \\ & \exp(-i\omega_D(x_1 - x_2)) \exp\left(-2\mu_s \frac{v_ax_1 + v_ax_2}{2\bar{n}}\right) \\ & \exp\left(-\frac{|\Delta\boldsymbol{\rho}_b|^2}{w_{0s}^2}\right) \exp\left[-\frac{1}{2\sigma^2}\left(\frac{v_ax_1 - v_ax_2}{\bar{n}}\right)^2\right]. \end{aligned} \quad (6.61)$$

We will introduce a short-hand notation:

$$\begin{aligned} \Pi_0(t_1, t_2) &= \left(\frac{1}{h\nu_0}\right)^2 \int dx_1 \int dx_2 H_{Meyer}(t_1, x_1) H_{Meyer}(t_2, x_2) \\ &< P_{rs,F}(x_1)P_{rs,F}^*(x_2)|H_0 >_M. \end{aligned} \quad (6.62)$$

Using eq. (6.61), $\Pi_0(t_1, t_2)$ can be written as

$$\begin{aligned} \Pi_0(t_1, t_2) &= \left(\frac{1}{h\nu_0}\right)^2 \exp\left(-\frac{|\Delta\boldsymbol{\rho}_b|^2}{w_{0s}^2}\right) C_{rs}D_0 \sqrt{\frac{\pi}{2}}\sigma \left(\frac{\pi w_{0s}^2}{4}\right) \\ & \int dx_1 \int dx_2 H_{Meyer}(t_1, x_1) H_{Meyer}(t_2, x_2) \exp(i\omega_D(x_2 - x_1)) \\ & \exp\left(-\frac{\mu_s}{\bar{n}}(v_ax_1 + v_ax_2)\right) \exp\left[-\frac{1}{2\sigma^2}\left(\frac{v_ax_1 - v_ax_2}{\bar{n}}\right)^2\right]. \end{aligned} \quad (6.63)$$

Using eq. (4.95), the term $H_{Meyer}(t_1, x_1)H_{Meyer}(t_2, x_2) \exp(i\omega_D(x_2 - x_1))$ can be written as

$$\begin{aligned} & H_{Meyer}(t_1, x_1)H_{Meyer}(t_2, x_2) \exp(i\omega_D(x_2 - x_1)) \\ &= (\zeta e)^2 \cos(\omega_m x_1) \psi_{Meyer}(t_1, x_1) \cos(\omega_m x_2) \psi_{Meyer}(t_2, x_2) \exp(i\omega_D(x_2 - x_1)). \end{aligned}$$

We will rewrite

$$\begin{aligned} & \cos(\omega_m x_1) \exp(-i\omega_D x_1) \cos(\omega_m x_2) \exp(i\omega_D x_2) \\ &= \frac{1}{4}(1 + \exp(-i2\omega_D x_1) + \exp(i2\omega_D x_2) + \exp(i\omega_D(x_2 + x_1))), \quad (6.64) \end{aligned}$$

Since the exponential terms in eq. (6.64) corresponds to rapid oscillations on the scale of σ , only the constant term in eq. (6.64) will have non-trivial contribution to the integral in eq. (6.63), and eq. (6.63) can be written as

$$\begin{aligned} \Pi_0(t_1, t_2) &= \left(\frac{1}{h\nu_0}\right)^2 \exp\left(-\frac{|\Delta\rho_b|^2}{w_{0s}^2}\right) C_{rs} D_0 \sqrt{\frac{\pi}{2}} \sigma\left(\frac{\pi w_{0s}^2}{4}\right) \frac{1}{4} (\zeta e)^2 \\ & \int dx_1 \int dx_2 \psi_{Meyer}(t_1, x_1) \psi_{Meyer}(t_2, x_2) \\ & \exp\left(-\frac{\mu_s}{\bar{n}}(v_a x_1 + v_a x_2)\right) \exp\left[-\frac{1}{2\sigma^2}\left(\frac{v_a x_1 - v_a x_2}{\bar{n}}\right)^2\right]. \end{aligned}$$

Since $\Pi_0(t_1, t_2)$ is real, eq.(6.57) can be written as

$$\begin{aligned} K_{scat, H_0}(t_1, t_2) &= 2\Pi_0(t_1, t_2) \\ &= 2\left(\frac{1}{h\nu_0}\right)^2 \exp\left(-\frac{|\Delta\rho_b|^2}{w_{0s}^2}\right) C_{rs} D_0 \sqrt{\frac{\pi}{2}} \sigma\left(\frac{\pi w_{0s}^2}{4}\right) \frac{1}{4} (\zeta e)^2 \Theta_0(t_1, t_2), \quad (6.65) \end{aligned}$$

where

$$\begin{aligned} \Theta_0(t_1, t_2) &= \int dx_1 \int dx_2 \psi_{Meyer}(t_1, x_1) \psi_{Meyer}(t_2, x_2) \\ & \exp\left(-\frac{\mu_s}{\bar{n}}(v_a x_1 + v_a x_2)\right) \exp\left[-\frac{1}{2\sigma^2}\left(\frac{v_a x_1 - v_a x_2}{\bar{n}}\right)^2\right]. \quad (6.66) \end{aligned}$$

Using eq. (6.56) for C_{rs} , eq. (6.65) can be written as

$$\begin{aligned} & K_{scat,H_0}(t_1, t_2) \\ &= \frac{1}{8} \sqrt{\frac{\pi}{2}} \left(\frac{\zeta e P_0 w_0}{h \nu_0 f_1} |\alpha_r^* \alpha_s| \right)^2 \sigma \sigma_{b0} \exp\left(-\frac{|\Delta \boldsymbol{\rho}_b|^2}{w_{0s}^2}\right) \Theta_0(t_1, t_2). \end{aligned} \quad (6.67)$$

Signal Present For the signal present state, the scatterer number density is written as (see eq. (6.15))

$$\Upsilon_{NP}(\mathbf{r}) = D_0 + \delta \Upsilon_{NP}(\mathbf{r}).$$

As shown in eq. (6.54), the two-time correlation function is linear in $\Upsilon(\mathbf{r})$. Therefore the two-time correlation function for the signal present state can be written as the contribution from the background and the target/abnormality:

$$\begin{aligned} & \langle P_{rs,F}(x_1) P_{rs,F}^*(x_2) | H_1 \rangle_M \\ &= \langle P_{rs,F}(x_1) P_{rs,F}^*(x_2) | H_0 \rangle_M + \langle \Delta P_{rs,F}(x_1) P_{rs,F}^*(x_2) \rangle_M, \end{aligned} \quad (6.68)$$

where

$$\begin{aligned} & \langle \Delta P_{rs,F}(x_1) P_{rs,F}^*(x_2) \rangle_M = C_{rs} \exp(-i\omega_D(x_1 - x_2)) \\ & \int d\mathbf{r}_{d1} \delta \Upsilon(\mathbf{r}_{d1} + \boldsymbol{\rho}_{b1}) \exp\left(-\frac{2}{w_{0s}^2}(\rho_{d1}^2 + |\boldsymbol{\rho}_{d1} - \Delta \boldsymbol{\rho}_b|^2)\right) \exp(-2\mu_s z_{d1}) \\ & \exp\left[-\frac{1}{\sigma^2} \left(\frac{v_a x_1}{\bar{n}} - z_{d1}\right)^2\right] \exp\left[-\frac{1}{\sigma^2} \left(\frac{v_a x_2}{\bar{n}} - z_{d1}\right)^2\right]. \end{aligned} \quad (6.69)$$

Using eq. (6.14) for $\delta \Upsilon(\mathbf{r}_{d1} + \boldsymbol{\rho}_{b1})$ and (6.59), eq. (6.69) can be written as

$$\begin{aligned} & \langle \Delta P_{rs,F}(x_1) P_{rs,F}^*(x_2) \rangle_M \\ &= \eta D_0 C_{rs} \exp(-i\omega_D(x_1 - x_2)) \exp\left[-\frac{1}{2\sigma^2} \left(\frac{v_a x_1 - v_a x_2}{\bar{n}}\right)^2\right] \\ & \int dz_{d1} \exp\left[-\frac{(z_{d1} - z_c^2)}{\sigma_z^2}\right] \exp(-2\mu_s z_{d1}) \exp\left[-\frac{2}{\sigma^2} \left(z_{d1} - \frac{v_a x_1 + v_a x_2}{2\bar{n}}\right)^2\right] \\ & \int d\boldsymbol{\rho}_{d1} \exp\left[-\frac{|\boldsymbol{\rho}_{d1} + \boldsymbol{\rho}_{b1} - \boldsymbol{\rho}_c|^2}{\sigma_\rho^2}\right] \exp\left(-\frac{2}{w_{0s}^2}(\rho_{d1}^2 + |\boldsymbol{\rho}_{d1} - \Delta \boldsymbol{\rho}_b|^2)\right). \end{aligned} \quad (6.70)$$

The first integral in eq. (6.70) can be evaluated as (see Appendix B)

$$\begin{aligned}
& \int dz_{d1} \exp\left[-\frac{(z_{d1} - z_c)^2}{\sigma_z^2}\right] \exp(-2\mu_s z_{d1}) \exp\left[-\frac{2}{\sigma^2}\left(z_{d1} - \frac{v_a x_1 + v_a x_2}{2\bar{n}}\right)^2\right] \\
& \approx \sqrt{\pi} \frac{\sigma_z}{\sqrt{1 + 4\beta_z^2}} \exp\left(-2\mu_s \frac{1}{1 + 4\beta_z^2} \left(z_c + \beta_z^2 \frac{v_a x_1 + v_a x_2}{2\bar{n}}\right)\right) \\
& \exp\left[-\frac{2}{\sigma^2(1 + 4\beta_z^2)} \left(z_c - \frac{v_a x_1 + v_a x_2}{2\bar{n}}\right)^2\right], \tag{6.71}
\end{aligned}$$

where β_z measures the ratio between the target dimension and the system resolution in the axial direction (see Appendix B):

$$\beta_z^2 = \frac{\pi\sigma_z^2}{(l_{cm})^2}, \tag{6.72}$$

where l_{cm} is the corresponding coherence length in the sample:

$$l_{cm} = \frac{l_c}{\bar{n}}, \tag{6.73}$$

which is contracted by a factor of $\frac{1}{\bar{n}}$ due to the fact that light travels slower in the sample.

The second integral in eq. (6.70) can be evaluated as (see Appendix C)

$$\begin{aligned}
& \int d\boldsymbol{\rho}_{d1} \exp\left(-\frac{2}{w_{0s}^2}(\rho_{d1}^2 + |\boldsymbol{\rho}_{d1} - \Delta\boldsymbol{\rho}_b|^2)\right) \exp\left(-\frac{|\boldsymbol{\rho}_{d1} + \boldsymbol{\rho}_{b1} - \boldsymbol{\rho}_c|^2}{\sigma_\rho^2}\right) \\
& = \pi \frac{\sigma_\rho^2}{1 + 8\beta_\rho^2} \exp\left(-\frac{1}{w_{0s}^2} |\Delta\boldsymbol{\rho}_b|^2\right) \exp\left(-\frac{4}{w_{0s}^2(1 + 8\beta_\rho^2)} \left|\boldsymbol{\rho}_c - \frac{\boldsymbol{\rho}_{b1} + \boldsymbol{\rho}_{b2}}{2}\right|^2\right), \tag{6.74}
\end{aligned}$$

where

$$\beta_\rho = \frac{\sigma_\rho}{\sqrt{2}w_{0s}}, \tag{6.75}$$

which is the ratio of the target dimension to the the transverse resolution of an OCT

imaging system. Using eqs. (6.71 and 6.74), eq. (6.70) can be written as

$$\begin{aligned}
& \langle \Delta P_{rs,F}(x_1) P_{rs,F}^*(x_2) \rangle_M \\
&= C_{rs,\Delta} \exp(-i\omega_D(x_1 - x_2)) \exp\left(-\frac{2\mu_s}{1 + 4\beta_z^2} \left(z_c + \beta_z^2 \frac{v_a x_1 + v_a x_2}{2\bar{n}}\right)\right) \\
&\quad \exp\left[-\frac{2}{\sigma^2(1 + 4\beta_z^2)} \left(z_c - \frac{v_a x_1 + v_a x_2}{2\bar{n}}\right)^2\right] \exp\left(-\frac{4}{w_{0s}^2(1 + 8\beta_\rho^2)} \left|\rho_c - \frac{\rho_{b1} + \rho_{b2}}{2}\right|^2\right) \\
&\quad \exp\left(-\frac{1}{w_{0s}^2} |\Delta\rho_b|^2\right) \exp\left[-\frac{1}{2\sigma^2} \left(\frac{v_a x_1 - v_a x_2}{\bar{n}}\right)^2\right], \tag{6.76}
\end{aligned}$$

where

$$C_{rs,\Delta} = C_{rs}\eta D_0 \sqrt{\pi} \frac{\sigma_z}{\sqrt{1 + 4\beta_z^2}} \pi \frac{\sigma_\rho^2}{1 + 8\beta_\rho^2}, \tag{6.77}$$

and C_{rs} is given by eq. (6.56). We will introduce the following short-hand notation:

$$\begin{aligned}
\Delta\Pi(t_1, t_2) &= \left(\frac{1}{h\nu_0}\right)^2 \int dx_1 \int dx_2 \\
&H_{Meyer}(t_1, x_1) H_{Meyer}(t_2, x_2) \langle \Delta P_{rs,F}(x_1) P_{rs,F}^*(x_2) \rangle_M. \tag{6.78}
\end{aligned}$$

Using eq. (6.76), eq. (6.78) can be written as

$$\begin{aligned}
\Delta\Pi(t_1, t_2) &= \left(\frac{1}{h\nu_0}\right)^2 C_{rs,\Delta} \int dx_1 \int dx_2 H_{Meyer}(t_1, x_1) H_{Meyer}(t_2, x_2) \\
&\quad \exp(-i\omega_D(x_1 - x_2)) \exp\left(-\frac{2\mu_s}{1 + 4\beta_z^2} \left(z_c + 4\beta_z^2 \frac{v_a x_1 + v_a x_2}{2\bar{n}}\right)\right) \\
&\quad \exp\left[-\frac{2}{\sigma^2(1 + 4\beta_z^2)} \left(z_c - \frac{v_a x_1 + v_a x_2}{2\bar{n}}\right)^2\right] \exp\left(-\frac{4}{w_{0s}^2(1 + 8\beta_\rho^2)} \left|\rho_c - \frac{\rho_{b1} + \rho_{b2}}{2}\right|^2\right) \\
&\quad \exp\left(-\frac{1}{w_{0s}^2} |\Delta\rho_b|^2\right) \exp\left[-\frac{1}{2\sigma^2} \left(\frac{v_a x_1 - v_a x_2}{\bar{n}}\right)^2\right]. \tag{6.79}
\end{aligned}$$

The quantities ρ_{bi} corresponds to the location of the beam centers at time t_i , which changes relatively slowly in each axial scan. Therefore, the terms $\exp(-\frac{1}{w_{0s}^2} |\Delta\rho_b|^2)$ and $\exp(-\frac{4}{w_{0s}^2(1+8\beta_\rho^2)} \left|\rho_c - \frac{\rho_{b1} + \rho_{b2}}{2}\right|^2)$ are slow varying functions in x_1 and x_2 . It is possible to pull them out of the integrals over x_1 and x_2 , and eq. (6.79) can be

rewritten as

$$\begin{aligned} \Delta\Pi(t_1, t_2) &\equiv \frac{1}{4} \left(\frac{\zeta e}{h\nu_0} \right)^2 C_{rs,\Delta} \exp\left(-\frac{1}{w_{0s}^2} |\Delta\rho_b|^2\right) \\ &\quad \exp\left(-\frac{4}{w_{0s}^2(1+8\beta_\rho^2)} \left| \rho_c - \frac{\rho_{b1} + \rho_{b2}}{2} \right|^2\right) \Theta_\Delta(t_1, t_2), \end{aligned} \quad (6.80)$$

where

$$\begin{aligned} \Theta_\Delta(t_1, t_2) &= \int dx_1 \int dx_2 \psi_{Meyer}(t_1, x_1) \psi_{Meyer}(t_2, x_2) \exp\left(-\frac{2\mu_s}{1+4\beta_z^2} \left(z_c + 4\beta_z^2 \frac{v_a x_1 + v_a x_2}{2\bar{n}}\right)\right) \\ &\quad \exp\left[-\frac{2}{\sigma^2(1+4\beta_z^2)} \left(z_c - \frac{v_a x_1 + v_a x_2}{2\bar{n}}\right)^2\right] \exp\left[-\frac{1}{2\sigma^2} \left(\frac{v_a x_1 - v_a x_2}{\bar{n}}\right)^2\right]. \end{aligned} \quad (6.81)$$

Using eqs. (6.57 and 6.68), the contribution to the covariance matrix due to scattering for the signal present state can be written as

$$\begin{aligned} K_{scat,H1}(t_1, t_2) &= \left(\frac{1}{h\nu_0}\right)^2 \int dx_1 \int dx_2 H_{Meyer}(t_1, x_1) H_{Meyer}(t_2, x_2) \\ &\quad [\langle P_{rs,F}(x_1) P_{rs,F}^*(x_2) | H_0 \rangle_M + \langle \Delta P_{rs,F}(x_1) P_{rs,F}^*(x_2) \rangle_M + C.C.] \\ &= K_{scat,H0}(t_1, t_2) + 2\Delta\Pi(t_1, t_2), \end{aligned} \quad (6.82)$$

where $K_{scat,H0}(t_1, t_2)$ and $\Delta\Pi(t_1, t_2)$ are given by eqs. (6.67 and 6.80) respectively.

6.4 Simulation

We will start this section with a summary of the relevant equations for the calculation of the covariance for the OCT data and the detectability. Then we will list the parameters used for the simulation. We will also explain how to evaluate the change in the scattering coefficient induced by the nanoparticle contrast agent, as well as the number of data points to be considered within the imaging area.

6.4.1 Summary of Equations

As shown in eq. (5.66), the covariance of the OCT data is:

$$K(t_1, t_2) = K_{shot}(t_1, t_2) + K_{scat}(t_1, t_2), \quad (6.83)$$

where $K_{shot}(t_1, t_2)$ is the shot noise contribution and $K_{scat}(t_1, t_2)$ the scattering noise contribution.

Shot Noise Contribution

Signal Absent The contribution from the shot noise for the signal absent state is (see eq. (6.43)):

$$K_{shot,H_0}(t, t) = \frac{\zeta e P_0 \zeta e}{h\nu_0} \frac{1}{2} \int dx \psi_{Meyer}^2(t, x) \{ |\alpha_r|^2 + \frac{1}{8} |\alpha_s|^2 \left(\frac{a_1}{f_1}\right)^2 \sigma_{b0} \frac{1}{\mu_s} (1 - \exp(-2\mu_s d)) \}. \quad (6.84)$$

Signal Present The contribution from the shot noise for the signal present state is (see eq. (6.50)):

$$K_{shot,H_1}(t_1, t_2) = K_{shot,H_0}(t_1, t_2) + \frac{|\alpha_s|^2 P_0 \zeta e}{h\nu_0} \zeta e \frac{1}{4} \left(\frac{a_1}{f_1}\right)^2 \sigma_{b0} \eta \sigma_\rho^2 \int dx \psi_{Meyer}(t_1, x) \psi_{Meyer}(t_2, x) \Omega_s(\mathbf{r}_c, \sigma_z, \sigma_\rho, z_{0s}, x). \quad (6.85)$$

where (see eq. (6.48))

$$\Omega_s(\mathbf{r}_c, \sigma, z_{0s}, t) = \int dz_{d1} \exp(-2\mu_s z_{d1}) \exp\left[-\frac{(z_{d1} - z_c)^2}{\sigma_z^2}\right] \frac{1}{w_s^2(z_{d1}, t) + 2\sigma_\rho^2} \exp\left[-\frac{2}{w_s^2(z_{d1}, t) + 2\sigma_\rho^2} |v_l t \hat{y} - \boldsymbol{\rho}_c|^2\right]. \quad (6.86)$$

Scattering Noise Contribution

Signal Absent The contribution from the scattering noise for the signal absent state is (see eq. (6.67)):

$$K_{scat,H_0}(t_1, t_2) = \frac{1}{8} \sqrt{\frac{\pi}{2}} \left(\frac{\zeta e P_0 w_0}{h\nu_0} \frac{1}{f_1} |\alpha_r^* \alpha_s|\right)^2 \sigma \sigma_{b0} \exp\left(-\frac{\Delta \boldsymbol{\rho}_b^2}{w_{0s}^2}\right) \Theta_0(t_1, t_2), \quad (6.87)$$

where (see eq. (6.66))

$$\begin{aligned} \Theta_0(t_1, t_2) = & \int dx_1 \int dx_2 \psi_{Meyer}(t_1, x_1) \psi_{Meyer}(t_2, x_2) \\ & \exp\left(-\frac{\mu_s}{\bar{n}}(v_a x_1 + v_a x_2)\right) \exp\left[-\frac{1}{2\sigma^2}\left(\frac{v_a x_1 - v_a x_2}{\bar{n}}\right)^2\right]. \end{aligned} \quad (6.88)$$

Signal Present The contribution from the scattering noise for the signal present state is (see eq. (6.82)):

$$K_{scat,H1}(t_1, t_2) = K_{scat,H0}(t_1, t_2) + 2\Delta\Pi(t_1, t_2), \quad (6.89)$$

where (see eq. (6.80))

$$\begin{aligned} \Delta\Pi(t_1, t_2) \equiv & \frac{\sqrt{2\pi}}{2} \left(\frac{\zeta e P_0}{h\nu_0} |\alpha_r^* \alpha_s| \frac{w_0}{f_1}\right)^2 \sigma_{b0} \eta \sigma \frac{\beta_z \beta_\rho^2}{(1 + 8\beta_\rho^2) \sqrt{1 + 4\beta_z^2}} \exp\left(-\frac{1}{w_{0s}^2} |\Delta\boldsymbol{\rho}_b|^2\right) \\ & \exp\left(-\frac{4}{w_{0s}^2 (1 + 8\beta_\rho^2)} \left|\boldsymbol{\rho}_c - \frac{\boldsymbol{\rho}_{b1} + \boldsymbol{\rho}_{b2}}{2}\right|^2\right) \Theta_\Delta(t_1, t_2), \end{aligned} \quad (6.90)$$

with (see eq. (6.81))

$$\begin{aligned} \Theta_\Delta(t_1, t_2) = & \int dx_1 \int dx_2 \psi_{Meyer}(t_1, x_1) \psi_{Meyer}(t_2, x_2) \exp\left(-\frac{2\mu_s}{1 + 4\beta_z^2} \left(z_c + 4\beta_z^2 \frac{v_a x_1 + v_a x_2}{2\bar{n}}\right)\right) \\ & \exp\left[-\frac{2}{\sigma^2 (1 + 4\beta_z^2)} \left(z_c - \frac{v_a x_1 + v_a x_2}{2\bar{n}}\right)^2\right] \exp\left[-\frac{1}{2\sigma^2} \left(\frac{v_a x_1 - v_a x_2}{\bar{n}}\right)^2\right]. \end{aligned} \quad (6.91)$$

Detectability and AUC

The index of detectability is (see eq. (2.16)):

$$d_a^2 = \frac{2[E(\lambda'|H_1) - E(\lambda'|H_0)]^2}{var(\lambda'|H_0) + var(\lambda'|H_1)}, \quad (6.92)$$

where (see eq. (2.19))

$$E(\lambda'|H_0) = tr\{\mathbf{K}_0 \mathbf{K}_1^{-1} - \mathbf{I}\}, \quad (6.93)$$

and (see eq. (2.20))

$$E(\lambda'|H_1) = tr\{\mathbf{I} - \mathbf{K}_1 \mathbf{K}_0^{-1}\}, \quad (6.94)$$

and (see eq. (2.30))

$$var(\lambda'|H_0) = 2tr\{(\mathbf{K}_1^{-1}\mathbf{K}_0 - \mathbf{I})^2\}, \quad (6.95)$$

and (see eq. (2.31))

$$var(\lambda'|H_1) = 2tr\{(\mathbf{I} - \mathbf{K}_0^{-1}\mathbf{K}_1)^2\} \quad (6.96)$$

The AUC (Area Under Curve) can be calculated as (see eq. (2.10))

$$AUC = \frac{1}{2} + \frac{1}{2} \operatorname{erf}\left[\frac{d_a}{2}\right]. \quad (6.97)$$

Important Expressions

Following is a list of equations defining terms used in the calculation of the covariance of the OCT data:

1. Beam width of the sample beam: The beam width of the sample beam in the sample is

$$w^2(z_{d1}, t) = w_{0s}^2 \left(1 + \left(\frac{\Delta_z(z_{d1}, t)}{z_{0s}}\right)^2\right),$$

where

$$\Delta_z(z_{d1}, t) = z_{d1} - \frac{v_a t}{n},$$

and

$$z_{0s} z_0 = \bar{n} f(t)^2 \approx \bar{n} f_1^2,$$

2. Sample size vs system resolution: β_z and β_ρ are the ratio between the target/abnormality size and the system resolution in the axial and transverse direction respectively.

$$\beta_\rho = \frac{\sigma_\rho}{\sqrt{2}w_{0s}},$$

and

$$\beta_z^2 = \frac{\sigma_z^2}{\sigma^2} = \frac{\pi\sigma_z^2}{(l_{cm})^2}.$$

3. Scales relating to the coherence length of the source: σ is a scale relating to the coherence length of the source

$$\sigma = \frac{1}{\sqrt{2\pi}} \frac{l_c}{\bar{n}} \equiv \frac{1}{\sqrt{2\pi}} l_{cm},$$

and l_{cm} is the source coherence length in the sample:

$$l_{cm} = \frac{l_c}{\bar{n}}$$

4. Covariance of permittivity field and scattering cross section for point scatterers:

Under the point scatterer model, the covariance of the permittivity field can be written as

$$K_\varepsilon(\mathbf{r}_1, \mathbf{r}_2) = \langle \xi'^2 \rangle \Upsilon(\mathbf{r}_1) \delta(\mathbf{r}_1 - \mathbf{r}_2).$$

The per unit volume backscattering cross section is

$$\sigma_b = 4\pi\sigma(-\hat{i}, \hat{i}) = k_0^4 \frac{1}{4\pi} \langle \xi'^2 \rangle D_0.$$

6.4.2 List of Parameters Used in the Simulation

The following parameters are used for the simulations:

- $\lambda_0 = 930nm$, central wavelength of the source
- $\Delta\lambda = 80nm$, bandwidth of the broadband source
- $l_c = \sqrt{\frac{2 \log 2}{\pi}} \frac{\lambda_0^2}{\Delta\lambda} = 7.18\mu m$, coherent length of the source in free space
- $P_0 = 4mW$, optical power of the source before splitting
- $W_{s0} = 5\mu m$, half beam waist of sample beam inside the sample
- $|\alpha_r|^2 = 0.5$, fraction of source optical power going into the reference beam
- $|\alpha_s|^2 = 0.5$, fraction of source optical power going into the sample beam
- $NA = 0.28$, numerical aperture of the focusing lens in front of the sample

- $v_a = 25mm/s$, scanning velocity in the axial direction
- $\tau_b = \frac{1}{\Delta_{fb}} = \frac{c}{2v_a} \frac{1}{\Delta\nu} \sqrt{\frac{2\ln 2}{\pi}} = 0.15ms$, response time of band-pass filter in the data acquisition chain
- $\zeta = 1$, quantum efficiency of detector

6.4.3 Optical Properties of the Host Tissue and the Nanoparticle Contrast Agents

In this simulation, the host biological tissue is assumed to be breast tissue, with the following optical properties measured by Garofalakis et. al. at the wavelength of $800nm$ [94]:

1. $n = 1.36$, index of refraction of the breast tissue
2. $\mu_{an} = 9.9m^{-1}$, absorption coefficient for normal breast tissue
3. $\mu_{sn} = 970m^{-1}$, reduced scattering coefficient of normal breast tissue
4. $\mu_{sd} = 1050m^{-1}$, reduced scattering coefficient of diseased breast tissue

On the other hand, we have assumed that the source of the OCT system has a central wavelength of $930nm$, which is different from the wavelength at which Garofalakis et al. performed the measurement. Since we could not find no published data on the optical properties of biological tissue at the wavelength of $930nm$, we used the above values measured at $800nm$ as approximations to the values at $930nm$.

As described in §6.1.3 (Anisotropy and Reduced Scattering Coefficient), an anisotropic biological tissue can be replaced by an isotropic medium described by the corresponding reduced scattering coefficients with $g = 0$. In this simulation, the host tissue is replaced by a mathematical model of point scatterers described by the reduced scattering coefficients given above (properties (3) and (4)) and an anisotropy parameter

$g = 0$. The scattering effect of the host tissue is taken into account by replacing σ_{b0} in eqs. ((6.84), (6.85), (6.87), and (6.90)) by $\sigma_{b,t}$:

$$\sigma_{b,t} = \sigma_{b,NP} + \sigma_{b,h}, \quad (6.98)$$

where $\sigma_{b,NP}$ and $\sigma_{b,h}$ is the per unit volume backscattering cross sections of the nanoparticles and the host tissue, respectively. Similarly, the attenuation coefficient will be replaced by

$$\mu_{s,t} = \mu_{s,NP} + \mu_{s,h}, \quad (6.99)$$

where $\mu_{s,NP}$ and $\mu_{s,h}$ is the attenuation coefficients of the nanoparticles and the host tissue, respectively. We have assumed that absorption is negligible in this analysis.

The scattering coefficient of the nanoparticles are calculated based on the results published in [92] for the R75/115 gold nanoshell. The properties of this nanoshell can be summarized as follows:

1. Geometrical size: Outer radius of the gold shell is $115nm$, and the radius of the inner dielectric core is $75nm$.
2. Index of refraction is $n = 1.4$, which is similar to the index of refraction of the normal breast tissue ($n = 1.36$). Therefore, we will assume the addition of the nanoparticles will not change the refractivity of the host tissue significantly, and use $n = 1.36$ for the analysis.
3. Volume normalized scattering cross section is $C_{sca} \sim 3.25 \times 10^7 m^{-1}$ at the wavelength of $1000nm$, and the volume normalized absorption cross section is $C_{abs} \sim 0.3 \times 10^7 m^{-1}$. The scattering coefficient can be calculated by using the volume of the particle (V_p) and the concentration (ie., number density D) of the particles as

$$\mu_{sca} = C_{sca} V_p D. \quad (6.100)$$

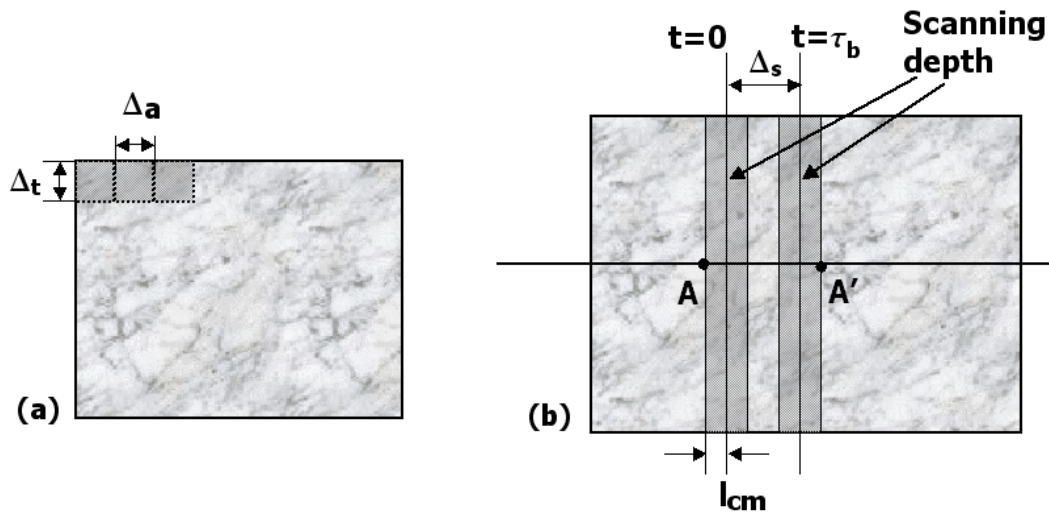


FIGURE 6.2. Illustration of axial and transverse intervals.

Using the R75/115 gold nanoshell as an example, the volume of the nanoparticle can be calculated as $V_p = \frac{4}{3}\pi(115 \times 10^{-9})^3$. If we assume a concentration of $D = 2.5 \times 10^{15} m^{-3}$, which is a concentration that has been used in a nanoparticle aided OCT imaging experiment described in [95], then the scattering coefficient due to the nanoparticle can be calculated as $\mu_{sca} = 517.613 m^{-1}$. By changing the concentration, one can change the scattering property of the biological tissue.

6.4.4 Imaging Area and Number of Data Point

We assume an imaging area of $2mm \times 2mm$. The number of data points within this area is determined by two parameters: the axial interval (Δ_a) and the transverse interval (Δ_t) between the data points. Together, these two parameters determine an imaging cell which will tile the whole imaging area as shown in figure 6.2 (a).

The transverse interval is determined by the transverse resolution of the OCT system, which corresponds to the beam waist of the sample beam inside the biological

tissue (W_{0s}):

$$\Delta_t = 2\sqrt{\log 2}W_{0s}. \quad (6.101)$$

The axial interval is determined by two factors:

1. The coherence length of the source,
2. The distance scanned by the reference mirror within the response time of the band-pass filter.

In OCT, due to the coherence-gating effect, only the slab centered around the scanning depth defined by the reference mirror will contribute to the interferometric term of the OCT data. The width of this slab is determined by the coherence length of the source in the sample, which is contracted to $l_{cm} = \frac{l_c}{n}$ due to the higher refractivity inside the sample. However, since the reference mirror is moving continuously during the data acquisition process, within the response time of the data acquisition process (τ_b , see §4.2.4), the scanning depth has advanced a distance of

$$\Delta_s = \frac{\tau_b v_a}{n} \quad (6.102)$$

inside the sample. Therefore, for each data point, the equivalent width of the contributing slab (AA') is a function of the source coherence length and Δ_s (see figure 6.2 (b)). Therefore, in this analysis, Δ_a is set to be

$$\Delta_a = 2l_{cm} + \Delta_s. \quad (6.103)$$

6.5 Results and Discussion

We first perform a baseline study in which no contrast agent is used. Using the breast tissue described in § 6.4.3 (Optical Properties of the Host Tissue and the Nanoparticle Contrast Agents), the two hypotheses can be stated as:

1. Signal absent: In the signal absent state, we are imaging a piece of normal tissue without contrast agent. The scattering coefficient as well as the per volume backscattering cross section of the tissue therefore is described by the optical properties of the normal tissue. Using eq. (6.99), with $\mu_{s,NP} = 0$, the scattering coefficient can be written as

$$\mu_{s,t} = \mu_{s,h} = 970m^{-1}. \quad (6.104)$$

We have used the reduced scattering coefficient of the normal breast tissue stated in § 6.4.3 for $\mu_{s,h}$.

2. Signal present: In the signal present state, the abnormality will be described by using the optical property of the diseased breast tissue. As stated in § 6.4.3, the reduced scattering coefficient of the diseased tissue increased from $\mu_{sn} = 970m^{-1}$ to $\mu_{sd} = 1050m^{-1}$, which corresponds to a fractional change of $\sim 8.2\%$:

$$\eta = \frac{\mu_{sd} - \mu_{sn}}{\mu_{sn}} = 0.082. \quad (6.105)$$

We will use this number for the fractional change parameter η in eqs. ((6.85) and (6.90)) to evaluate the contributions from the shot noise and the scattering noise for the signal present state. Even though the fractional change parameter was first derived in the context of change in the number density of the contrast agents (see § 6.1.3, Detection Task: Statement of the Hypothesis). It can be extended to describe the fractional change of the scattering coefficient due to the fact that the scattering coefficient of a random medium is linear in the number density of the particles (see eq. (6.3)).

Figure 6.3 is the result of the baseline study of the detectability for abnormalities of different sizes. It is assumed that the abnormality is at the center of the sample being imaged.

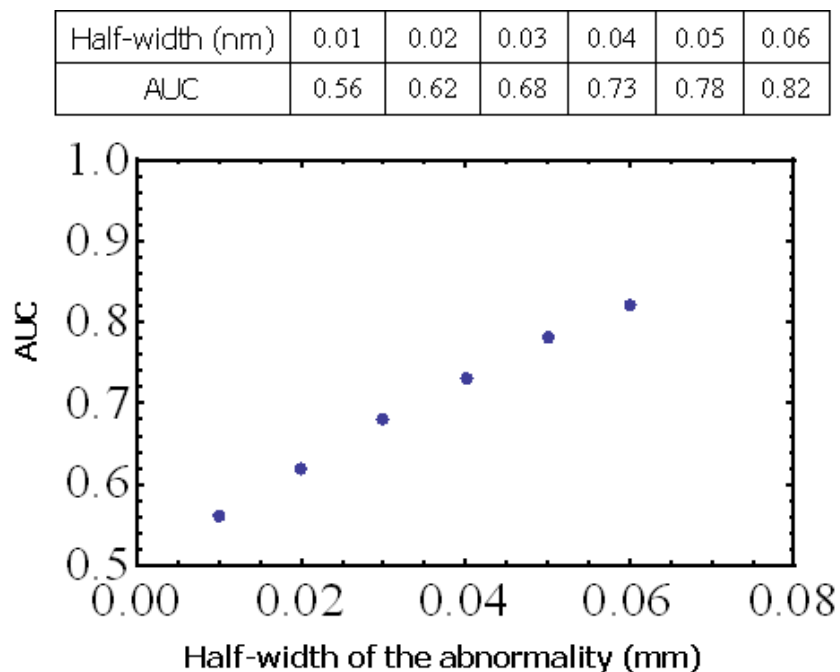


FIGURE 6.3. Baseline study of detectability for abnormalities of different sizes.

It is shown in this baseline study that for abnormalities with half-width smaller than 0.07mm, the AUC values (<0.85) is inferior for diagnostic purpose. The next step is to study the effect of contrast agents in improving the detection of such small abnormalities, which is of interest for early detection of diseases. We study the AUC of abnormalities with half-width of 0.01mm, 0.02mm, 0.04mm with respect to different concentration of contrast agent (D) and different fractional change parameters (η). We use $AUC=0.85$ as a benchmark for the desired AUC value in a clinical diagnosis in the following discussion.

Figure 6.4 shows the AUC values of an abnormality with half-width of 0.01mm. Without contrast agent, the AUC value for this abnormality is 0.56, as shown in the baseline study. By adding contrast agents, the AUC values are increased. We have shown two different sets of data: the round circles correspond to a data set with fractional change of 30% in the scattering property at the site of abnormality, while

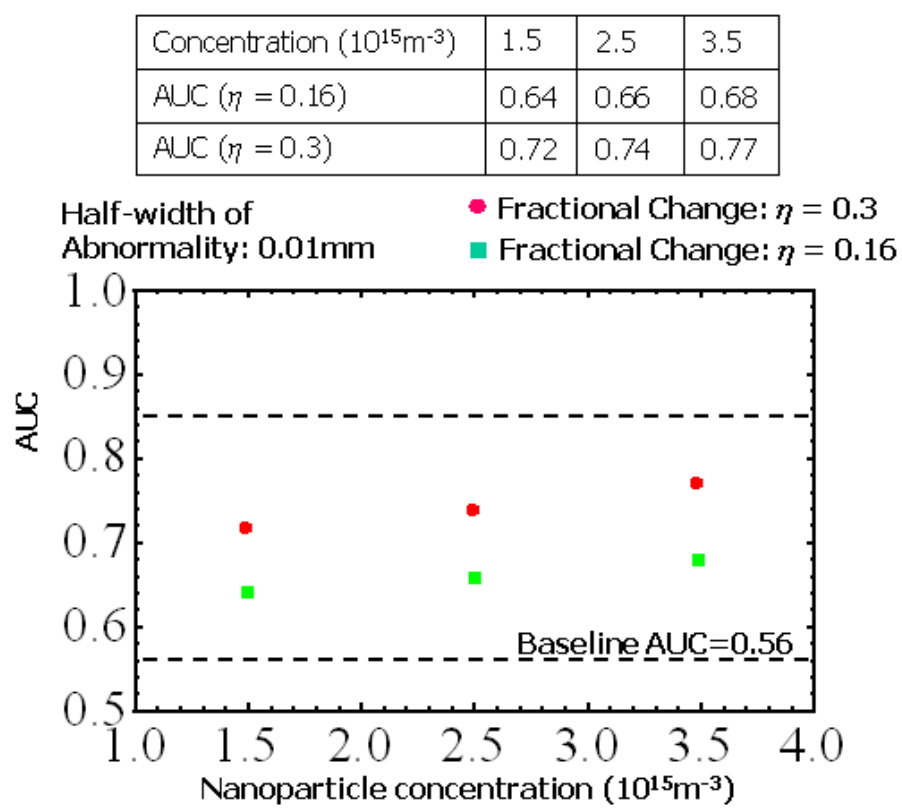


FIGURE 6.4. Detectability study for an abnormality with half-width of 0.01mm.

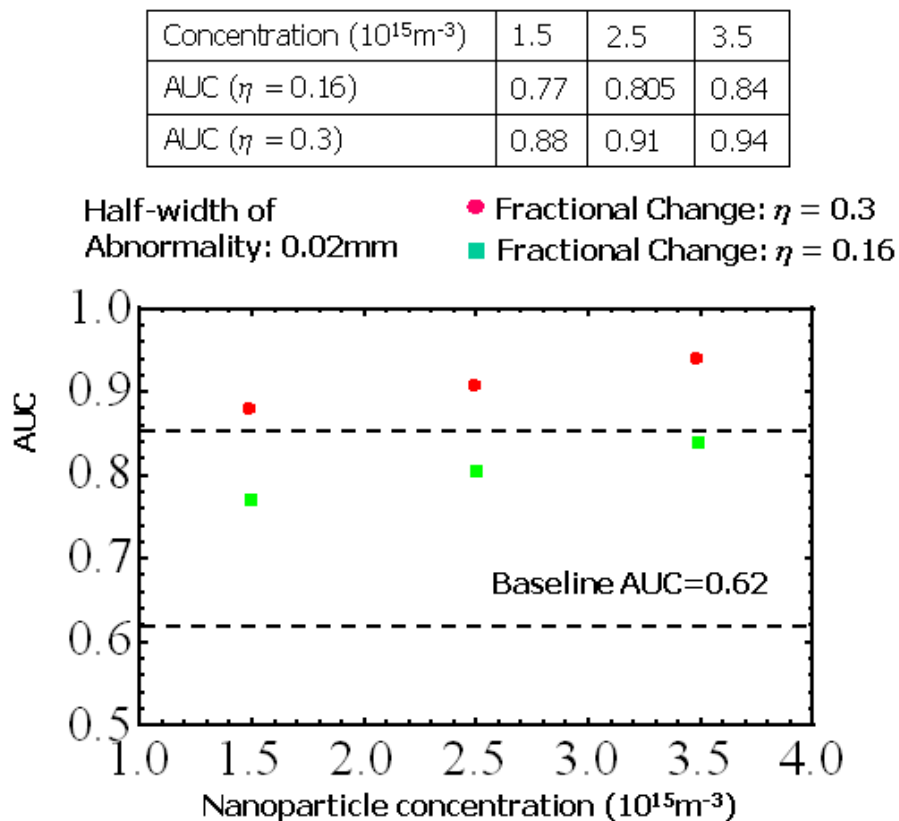


FIGURE 6.5. Detectability study for an abnormality with half-width of 0.02mm.

the squares correspond to a data set with fractional change of 16%. In the context of nanoparticles, the fractional change parameter corresponds to the increment in the number density of the nanoparticles at the site of abnormality. In assuming different fractional change parameters while keeping the concentrations unchanged, we are trying to study the possible improvement brought forth by nanoparticles with better specificity in targeting the abnormality site. For example, by changing the surface properties of the nanoparticles, it is possible to design nanoparticles that will have a higher affinity to the abnormality and thus increase the local fractional change while keeping the background concentration unchanged.

Figure 6.5 is the result of a similar study on an abnormality with half-width of 0.02mm. It is shown that, with the more target specific nanoparticles (ie., larger

Concentration ($10^{15}m^{-3}$)	0.1	0.25	0.5	1	1.5	2.5
AUC ($\eta = 0.16$)	0.875	0.882	0.89	0.91	0.93	0.96
AUC ($\eta = 0.3$)	0.97	0.976	0.98	0.987	0.99	0.99

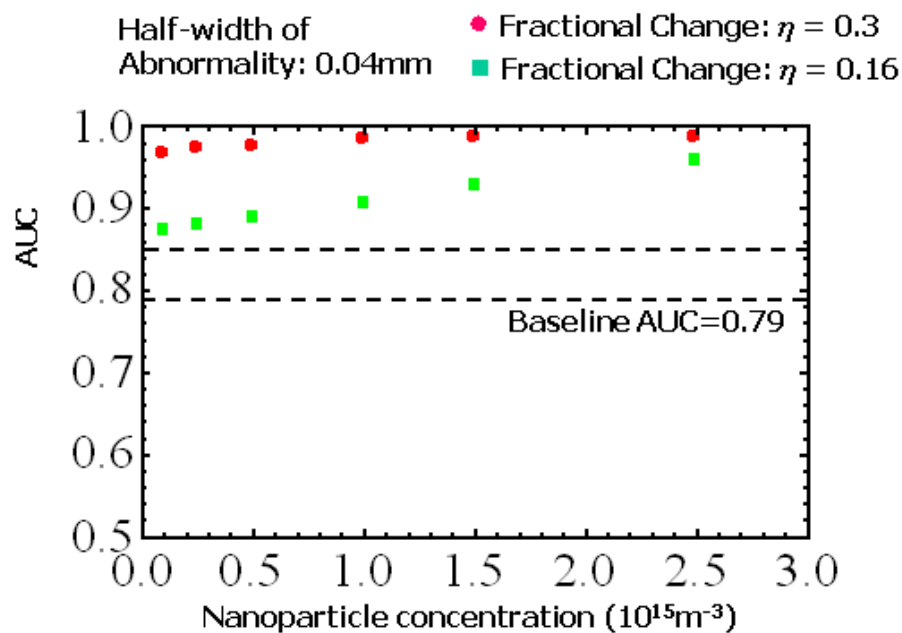


FIGURE 6.6. Detectability study of an abnormality with half-width of 0.04mm.

fractional change, the circles), it only needs a concentration of 1.5×10^{15} to reach an AUC value of 0.85, an AUC value regarded as more desirable for clinical diagnosis purposes. At the same time, for the less target specific nanoparticles (ie., smaller fractional change), it will take a concentration of around $3.5 \times 10^{-15}m^{-3}$ to reach the same AUC. This implies that enhancement in fractional change parameter is more effective in improving the AUC value than by increasing the nanoparticle concentration.

In figure 6.6, we show the result of an abnormality with half-width of 0.04mm. Without contrast agents, the baseline AUC value is 0.79. It is shown in this figure that the detectability of this abnormality is greatly enhanced by the use of the contrast

agents. For the group with fractional change parameter of 0.3, the AUC values all exceed 0.9. For the less target specific group ($\eta = 0.16$), a concentration as small as 0.1×10^{15} can lift the AUC value beyond the benchmark (AUC=0.85).

Chapter 7

SUMMARY AND FUTURE WORK

In this chapter, we will first give a summary of the important findings in this dissertation. Then we will discuss the approximations and simplifications adopted in the current work and possible areas of improvements for future work.

7.1 Summary

There is great interest in promoting the use of contrast agents in optical imaging for better diagnosis of diseases. However, up to recently, there was still no quantitative method existing to assess the ability of contrast agents in improving clinical diagnosis. We proposed to use the method of task-based medical image analysis as a quantitative tool to evaluate the effectiveness of nanoparticles as contrast agents in an OCT imaging modality. The method of task-based medical image analysis was advocated by Barrett et al. to optimize design parameters of imaging modalities (for example, see the discussion in ref [3]). In this dissertation, we expanded the scope of design parameters from the traditional hardware aspect to including the application of contrast agents as a new design parameter. The study presented in this dissertation is the first time that the quantitative method of task-based image analysis is applied to address the important questions on the effectiveness of contrast agents for clinical diagnosis, as well as the required concentration of contrast agents to obtain a meaningful diagnostic judgment.

The task was formulated as the detection of abnormalities in a biological tissue using a quadratic observer. In Chapter 2, we derived the test statistics of the quadratic observer, and an analytical expression of the index of detectability for such a quadratic observer. This result is a new addition to the toolbox for task-based

image analysis as the previous emphasis in our group has been in the study of linear observers. Also, in this dissertation, we presented an analysis of the OCT imaging modality at the system level by integrating demodulation process and the dynamic focusing scheme (see Chapter 4) into the analysis. This is the first time that such a detailed analysis at the system level is performed for an OCT imaging modality.

In Chapter 5, we presented the formulation of the biological tissue as a stochastic field (the scattering potential), and the decomposition of the covariance function of the OCT data into the different components corresponding to the shot noise, field fluctuations, and scattering noise (see § 5.4). In most OCT analysis, the effect of scattering was not addressed sufficiently and the object was often modeled as a stack of homogeneous media, even though it was obvious that scattering had affected the images significantly by causing the grainy features in the images. Also, in some literature, the OCT imaging modality was described as shot noise limited. Such a description actually contradicts the well-known fact that scattering is an dominating factor in biological tissue imaging so much so that the fluctuations caused by scattering may be more severe than shot noise. Our study provides a new platform for a quantitative comparison on the impact of scattering noise to shot noise in OCT imaging.

In Chapter 6, we presented the results on the detectability of abnormalities of different sizes, with or without the presence of the contrast agents. We have shown in §6.5 (Result and Discussion) that the application of nanoparticle contrast agents improved the detectability of small abnormalities which are usually difficult to detect. Also, by using an AUC value of 0.85 as the benchmark for meaningful clinical diagnosis, we were able to obtain quantitative indicators for the required concentrations of contrast agents with respect to the size of the abnormality as well as the target specificity of the contrast agent (the ability of the contrast agent to target the abnormality). We have thus shown the efficacy of the task-based analysis framework in delivering quantitative assessments of the efficiency of contrast agents. We

believe that such an analytical framework will be a valuable tool for researchers to establish guidelines for the use and development of contrast agents more effectively for diagnostic purposes.

7.2 Areas for Future Work

7.2.1 Mathematical Model for Biological Tissue

In this work, we introduced a stochastic model to describe the scattering potential that represents the random medium. This stochastic model was developed on the concept of a spatial Poisson random field, using an arbitrary lump function (see §5.2). In §6.3.2, we further reduced the lump function to a point scatterer described approximately by a delta function. This point scatterer approach can be justified for the nanoparticle since its dimension is smaller than the wavelength of the incident radiation and the coherence length of the source. However, it will not be adequate to describe real biological tissue constituted of structures that may be larger than a wavelength. Sheppard [96] and Xu et al. [97] proposed a fractal model to describe biological tissue based on a continuous refractive index variation as an improvement to the point scatterer biological tissue. Thrane et al. [13] used an atmospheric turbulence model to describe biological tissue for OCT analysis. However, more studies are needed to establish the validity of applying atmospheric turbulence models to biological tissues, since atmospheric turbulence is fundamentally different from the turbid nature of biological tissues. The other aspect of the point scatterers with point-wise correlation is that such model will not be able to explain any long range correlations that appear in an OCT image. A more comprehensive model needs to take into account the optical effect of the larger structures inside the tissue such as back reflection at the cell surfaces. Shapiro et al. has discussed such a model in a study on the detection of a reflecting object in the presence of point scatterers [98].

7.2.2 Stochastic Wave Propagation in Random Media

Inhomogeneities of Different Scales

As discussed in §3.5.2 (Media of Multiscale Fluctuations-Hybrid Model), biological tissue contains inhomogeneities of different scales, and scattering of the electromagnetic field depends strongly on the sizes of the inhomogeneities. Therefore, in order to capture the effects of the inhomogeneities of different scales on the propagating wave, a model such as the hybrid model discussed in §3.5.2 that addresses the forward scattering from larger inhomogeneities and the backscattering from smaller inhomogeneities simultaneously will be a better model to describe wave propagation in biological tissues.

Multiple Scattering

We adopted the first order multiple scattering approximation to model the sample field in this dissertation, based on the argument that multiple scattering will not contribute significantly to the interferometric term due to the coherence-gating effect of the OCT source field. The effect of multiple scattering on the optical power of the interferometric term may be minimized by the coherence-gate of the source field, but its effect on the optical power of the sample beam is less clear. For example, It is known that multiple scatterings will lead to backscattering enhancement for coherent waves in random medium. As shown in chapter 5, the optical power of the sample beam in turn can affect the detectability of the imaging modality since it contributes the covariance function of the demodulated OCT data through the shot noise. Therefore, further investigations are needed to understand in a quantitative way how multiple scattering impact the detectability of a coherent imaging modality such as OCT.

Near Field Effect

In this analysis, we assumed far-field approximation, which is a norm in most ana-

lytical studies of scattering. However, by using a phase screen as an example, Pusey [56] stated that strong intensity fluctuation can arise in the near-field Fresnel region behind the phase screen since the individual inhomogeneities in the phase screen act like lenses that can focus the propagating light shortly behind the screen. This near-field effect may be a very important phenomena to understand for optical imaging in biological tissue. Biological tissues are usually formed of closely packed entities, such as cells, with dimensions larger than the incident wavelength. If we approximate these cells as an ensemble of randomly distributed spheres, then, as a refractive object, each sphere can be considered as a ball lens. The randomness in positions, sizes and shapes of these ball lenses will introduce a strong fluctuation in the radiance of the field inside the sample. Now, consider a particular point scatterer, the scattered field intensity from this scatterer will vary drastically depending on whether the scatterer is inside the local focus of a ‘ball lens’ or not. Therefore, this random focusing effect will introduce a strong fluctuation in the scattered field strength, in the forward or backward direction.

7.2.3 Information Content and Demodulation Schemes

As discussed in §4.2.4, there are different schemes to demodulate the OCT data. In this dissertation, we presented an analysis based on the mixer scheme. There have been discussions on whether the information content carried by the images will be lost due to data processing during demodulation, and whether different demodulation schemes will cause losses to different aspects of the information. For example, a particular demodulation scheme may be better in conserving the long-range correlation in the image, while another scheme may only convey the short-range correlation in the image. This implies that certain demodulation schemes may perform better for certain tasks, and researchers can tailor their demodulation scheme depending on whether they are interested in the long-range or short-range features of the sample.

7.2.4 Different OCT Configurations

We developed the analysis for a time-domain OCT imaging modality. Different configurations of OCT imaging modality have been developed and used to obtain morphological as well as functional imaging of biological systems. It will be of interest to expand the current analysis to other configurations of OCT such as Fourier-domain OCT or Doppler OCT.

Appendix A

MEAN OF DEMODULATED OCT DATA

Using eq. (4.89 4.90 and 4.91), it can be shown that, when averaged over the shot noise, the demodulated OCT data can be written as a linear functional of the instantaneous optical power $P(t)$:

$$s_P(t) = \frac{e\varsigma}{h\nu_0 \tau_b} \int dt' P(t') \cos(\omega_m t') \operatorname{sinc}\left(\frac{1}{\tau_b}(t - t')\right). \quad (\text{A.1})$$

Since

$$P(t) = P_{DC}(t) + P_{int}(t),$$

with $P_{DC}(t)$ a slow varying function. Then

$$\int dt' P_{DC}(t') \cos(\omega_m t') \operatorname{sinc}\left(\frac{1}{\tau_b}(t - t')\right) \approx 0,$$

due to the fast oscillation in $\cos(\omega_m t')$. Therefore, eq. (A.1) can be written as

$$s_P(t) = \frac{e\varsigma}{h\nu_0 \tau_b} \int dt' P_{int}(t') \cos(\omega_m t') \operatorname{sinc}\left(\frac{1}{\tau_b}(t - t')\right),$$

where (see eq. (4.68))

$$P_{int}(t) = P_{rs}(t) + P_{rs}^*(t),$$

with (see eq. (4.69))

$$P_{rs}(t) = \int_{\infty} d\boldsymbol{\rho} \int d\mathbf{r}_d T(t'_{s,\mathcal{P}}) T^*(t'_{r,\mathcal{P}}) \mathcal{U}_{s,\mathcal{P}}(\boldsymbol{\rho}, \mathbf{r}_d; t) \mathcal{V}(\mathbf{r}_d + \boldsymbol{\rho}_b) U_{r,\mathcal{P}}^*(\boldsymbol{\rho}, t).$$

Then

$$\begin{aligned} \langle P_{rs}(t) \rangle_{F,M} &= \int_{\infty} d\boldsymbol{\rho} \int d\mathbf{r}_d \langle T(t'_{s,\mathcal{P}}) T^*(t'_{r,\mathcal{P}}) \rangle_F \\ &\quad \mathcal{U}_{s,\mathcal{P}}(\boldsymbol{\rho}, \mathbf{r}_d; t) \langle \mathcal{V}(\mathbf{r}_d + \boldsymbol{\rho}_b) \rangle_M U_{r,\mathcal{P}}^*(\boldsymbol{\rho}, t). \end{aligned} \quad (\text{A.2})$$

As shown in eq. (5.22),

$$\langle \mathcal{V}(\mathbf{r}) \rangle_M = 0.$$

Therefore, eq. (A.2) can be written as

$$\langle P_{rs}(t) \rangle_{F,M} = 0,$$

and the mean of the demodulated OCT data is

$$\langle s(t) \rangle_{P,F,M} = 0.$$

Appendix B

INTEGRAL IN THE Z-DIRECTION

Consider the integral

$$I_z = \int dz_{d1} \exp\left[-\frac{(z_{d1} - z_c)^2}{\sigma_z^2}\right] \exp(-2\mu_s z_{d1}) \exp\left[-\frac{2}{\sigma^2}\left(z_{d1} - \frac{v_a x_1 + v_a x_2}{2\bar{n}}\right)^2\right]. \quad (\text{B.1})$$

Since

$$\begin{aligned} & \exp\left[-\frac{(z_{d1} - z_c)^2}{\sigma_z^2}\right] \exp\left[-\frac{2}{\sigma^2}\left(z_{d1} - \frac{v_a x_1 + v_a x_2}{2\bar{n}}\right)^2\right] \\ = & \exp\left[-\left(\frac{1}{\sigma_z^2} + \frac{2}{\sigma^2}\right)\left(z_{d1} - \frac{\frac{\sigma^2}{2}z_c + \sigma_z^2 \frac{v_a x_1 + v_a x_2}{2\bar{n}}}{\sigma_s^2}\right)^2\right] \\ & \exp\left[-\frac{1}{\sigma_s^2}\left(z_c - \frac{v_a x_1 + v_a x_2}{2\bar{n}}\right)^2\right], \end{aligned} \quad (\text{B.2})$$

where

$$\sigma_s^2 = \sigma_z^2 + \frac{\sigma^2}{2} = \frac{\sigma^2}{2}\left(\frac{\sigma_z^2}{\sigma^2} + 1\right). \quad (\text{B.3})$$

As shown in eq. (5.92)

$$\sigma = \frac{\sqrt{\ln 2}c}{\bar{n}\pi\Delta\nu} = \frac{1}{\sqrt{2\pi}} \frac{l_c}{\bar{n}} = \frac{1}{\sqrt{2\pi}} l_{cm}. \quad (\text{B.4})$$

where l_c is the coherence length in free space (eq. (4.28)), and $l_{cm} = \frac{l_c}{\bar{n}}$ is the source coherence length inside the sample due to a slow down of light speed in the sample.

We will introduce a dimensionless quantity:

$$\beta_z^2 = \frac{\sigma_z^2}{\sigma^2} = \frac{\pi\sigma_z^2}{(l_{cm})^2}, \quad (\text{B.5})$$

which can be considered as the ratio between the disk area defined by the axial dimension of the target and the axial resolution area. Then eq. (B.3) can be written

as

$$\sigma_s^2 = \sigma_z^2 + \frac{\sigma^2}{2} = \frac{\sigma^2}{2}(4\beta_z^2 + 1), \quad (\text{B.6})$$

and eq. (B.2) can be written as

$$\begin{aligned}
& \exp\left[-\frac{(z_{d1} - z_c)^2}{\sigma_z^2}\right] \exp\left[-\frac{2}{\sigma^2}\left(z_{d1} - \frac{v_a x_1 + v_a x_2}{2\bar{n}}\right)^2\right] \\
= & \exp\left[-\frac{1}{\sigma_z^2}\left(1 + 4\beta_z^2\right)\left(z_{d1} - \frac{(z_c + 4\beta_z^2 \frac{v_a x_1 + v_a x_2}{2\bar{n}})}{(4\beta_z^2 + 1)}\right)^2\right] \\
& \exp\left[-\frac{2}{\sigma^2(4\beta_z^2 + 1)}\left(z_c - \frac{v_a x_1 + v_a x_2}{2\bar{n}}\right)^2\right], \tag{B.7}
\end{aligned}$$

Using this result for eq. (B.1), then we have

$$\begin{aligned}
I_z = & \exp\left[-\frac{2}{\sigma^2(4\beta_z^2 + 1)}\left(z_c - \frac{v_a x_1 + v_a x_2}{2\bar{n}}\right)^2\right] \\
& \int dz_{d1} \exp(-2\mu_s z_{d1}) \exp\left[-\frac{2}{\sigma^2}\left(\frac{1}{4\beta_z^2} + 1\right)\left(z_{d1} - \frac{(z_c + 4\beta_z^2 \frac{v_a x_1 + v_a x_2}{2\bar{n}})}{(4\beta_z^2 + 1)}\right)^2\right]. \tag{B.8}
\end{aligned}$$

We will assume that the attenuation is small such that $\exp(-2\mu_s z_{d1})$ is a slow varying function when compared to the scale $\left(\frac{2}{\sigma^2}\left(\frac{1}{4\beta_z^2} + 1\right)\right)^{-1/2}$ defined by the Gaussian in the integral. Then eq. (B.8) can be written as

$$\begin{aligned}
I_z = & \exp\left[-\frac{2}{\sigma^2(4\beta_z^2 + 1)}\left(z_c - \frac{v_a x_1 + v_a x_2}{2\bar{n}}\right)^2\right] \exp\left(-2\mu_s \frac{(z_c + 4\beta_z^2 \frac{v_a x_1 + v_a x_2}{2\bar{n}})}{(4\beta_z^2 + 1)}\right) \\
& \int dz_{d1} \exp\left[-\frac{2}{\sigma^2}\left(\frac{1}{4\beta_z^2} + 1\right)\left(z_{d1} - \frac{(z_c + 4\beta_z^2 \frac{v_a x_1 + v_a x_2}{2\bar{n}})}{(4\beta_z^2 + 1)}\right)^2\right]. \tag{B.9}
\end{aligned}$$

If one further assumes that boundary effect can be ignored and the range of the integral in for z_{d1} can be extended to $(-\infty, \infty)$, then eq. (B.9) can be written as

$$\begin{aligned}
I_z \approx & \sqrt{\pi} \frac{\sigma_z}{\sqrt{1 + 4\beta_z^2}} \exp\left[-\frac{2}{\sigma^2(4\beta_z^2 + 1)}\left(z_c - \frac{v_a x_1 + v_a x_2}{2\bar{n}}\right)^2\right] \\
& \exp\left(-2\mu_s \frac{(z_c + 4\beta_z^2 \frac{v_a x_1 + v_a x_2}{2\bar{n}})}{(4\beta_z^2 + 1)}\right). \tag{B.10}
\end{aligned}$$

Appendix C

INTEGRAL IN THE TRANSVERSE DIRECTION

In the transverse direction, the product of the two Gaussians can be written as

$$\begin{aligned}
& \exp\left(-\frac{|\boldsymbol{\rho}_{d1} + \boldsymbol{\rho}_{b1} - \boldsymbol{\rho}_c|^2}{\sigma_\rho^2}\right) \exp\left(-\frac{2}{w_{0s}^2}(\rho_{d1}^2 + |\boldsymbol{\rho}_{d1} - \Delta\boldsymbol{\rho}_b|^2)\right) \\
= & \exp\left(-\frac{1}{w_{0s}^2}|\Delta\boldsymbol{\rho}_b|^2\right) \exp\left(-\frac{4}{w_{0s}^2}\left|\boldsymbol{\rho}_{d1} - \frac{\Delta\boldsymbol{\rho}_b}{2}\right|^2\right) \exp\left(-\frac{|\boldsymbol{\rho}_{d1} + \boldsymbol{\rho}_{b1} - \boldsymbol{\rho}_c|^2}{\sigma_\rho^2}\right) \\
= & \exp\left(-\frac{1}{w_{0s}^2}|\Delta\boldsymbol{\rho}_b|^2\right) \exp\left(-\frac{1 + 4\frac{\sigma_\rho^2}{w_{0s}^2}}{\sigma_\rho^2}\left|\boldsymbol{\rho}_{d1} - \frac{\Delta\boldsymbol{\rho}_c + 2\frac{\sigma_\rho^2}{w_{0s}^2}\Delta\boldsymbol{\rho}_b}{1 + 4\frac{\sigma_\rho^2}{w_{0s}^2}}\right|^2\right) \\
& \exp\left(-\frac{4}{w_{0s}^2(1 + 4\frac{\sigma_\rho^2}{w_{0s}^2})}\left|\boldsymbol{\rho}_c - \frac{\boldsymbol{\rho}_{b1} + \boldsymbol{\rho}_{b2}}{2}\right|^2\right), \tag{C.1}
\end{aligned}$$

where $\Delta\boldsymbol{\rho}_c = \boldsymbol{\rho}_c - \boldsymbol{\rho}_{b1}$, with $\boldsymbol{\rho}_c$ the center of the abnormality and $\boldsymbol{\rho}_{b1}$ the center of the beam at t_1 . Let

$$\beta_\rho = \frac{\sigma_\rho}{\sqrt{2}w_{0s}}, \tag{C.2}$$

where $\sqrt{2}w_{0s}$ is the power-equivalent width of the sample beam at the focal plane. β_ρ can be considered as a measure of the ratio between the target dimension and the beam size in the transverse direction. Then eq. (C.1) can be written as

$$\begin{aligned}
& \exp\left(-\frac{|\boldsymbol{\rho}_{d1} + \boldsymbol{\rho}_{b1} - \boldsymbol{\rho}_c|^2}{\sigma_\rho^2}\right) \exp\left(-\frac{2}{w_{0s}^2}(\rho_{d1}^2 + |\boldsymbol{\rho}_{d1} - \Delta\boldsymbol{\rho}_b|^2)\right) \\
= & \exp\left(-\frac{1}{w_{0s}^2}|\Delta\boldsymbol{\rho}_b|^2\right) \exp\left(-\frac{1 + 8\beta_\rho^2}{\sigma_\rho^2}\left|\boldsymbol{\rho}_{d1} - \frac{\Delta\boldsymbol{\rho}_c + 4\beta_\rho^2\Delta\boldsymbol{\rho}_b}{1 + 8\beta_\rho^2}\right|^2\right) \\
& \exp\left(-\frac{4}{w_{0s}^2(1 + 8\beta_\rho^2)}\left|\boldsymbol{\rho}_c - \frac{\boldsymbol{\rho}_{b1} + \boldsymbol{\rho}_{b2}}{2}\right|^2\right), \tag{C.3}
\end{aligned}$$

Then the integral over $\boldsymbol{\rho}_{d1}$ can be written as

$$\begin{aligned}
& \int d\boldsymbol{\rho}_{d1} \exp\left(-\frac{2}{w_s^2}(\rho_{d1}^2 + |\boldsymbol{\rho}_{d1} - \Delta\boldsymbol{\rho}_b|^2)\right) \exp\left(-\frac{|\boldsymbol{\rho}_{d1} + \boldsymbol{\rho}_{b1} - \boldsymbol{\rho}_c|^2}{\sigma_\rho^2}\right) \\
= & \exp\left(-\frac{1}{w_{0s}^2} |\Delta\boldsymbol{\rho}_b|^2\right) \exp\left(-\frac{4}{w_{0s}^2(1+8\beta_\rho^2)} \left|\boldsymbol{\rho}_c - \frac{\boldsymbol{\rho}_{b1} + \boldsymbol{\rho}_{b2}}{2}\right|^2\right) \\
& \int d\boldsymbol{\rho}_{d1} \exp\left(-\frac{1+8\beta_\rho^2}{\sigma_\rho^2} \left|\boldsymbol{\rho}_{d1} - \frac{\Delta\boldsymbol{\rho}_c + 4\beta_\rho^2\Delta\boldsymbol{\rho}_b}{1+8\beta_\rho^2}\right|^2\right) \\
= & \pi \frac{\sigma_\rho^2}{1+8\beta_\rho^2} \exp\left(-\frac{1}{w_{0s}^2} |\Delta\boldsymbol{\rho}_b|^2\right) \\
& \exp\left(-\frac{4}{w_{0s}^2(1+8\beta_\rho^2)} \left|\boldsymbol{\rho}_c - \frac{\boldsymbol{\rho}_{b1} + \boldsymbol{\rho}_{b2}}{2}\right|^2\right). \tag{C.4}
\end{aligned}$$

REFERENCES

- [1] LAZEBNIK, M., MARKS, D. L., POTGIETER, K., GILLETTE, R., and BOPPART, S. A., “Functional optical coherence tomography for detecting neural activity through scattering changes,” *Optics Letters*, vol. 28, p. 1218, 2003.
- [2] BOPPART, S. A., OLDENBURY, A. L., XU, C., and MARKS, D. L., “Optical probes and techniques for molecular contrast enhancement in coherence imaging,” *Jour. of Biomedical Optics*, vol. 10, 2005.
- [3] BARRETT, H. H. and MYERS, K. J., *Foundations of Image Science*. Wiley Series in Pure and Applied Optics, 2004.
- [4] YOUNGQUIST, R. C., CARR, S., and DAVIES, D. E. N., “Optical coherence-domain reflectometry: A new optical evaluation technique,” *Opt. Lett*, vol. 12, pp. 158–160, 1987.
- [5] FERCHER, A. F., MENGEDOHT, K., and WERNER, W., “Eye-length measurement by interferometry with partially coherent-light,” *Opt. Lett*, vol. 13, pp. 186–188, 1988.
- [6] HITZENBERGER, C. K., “Optical measurement of the axial eye length by laser doppler interferometry,” *Inv. Ophthalmol. Vis. Sci*, vol. 32, pp. 616–624, 1991.
- [7] HUANG, D., SWANSON, E. A., LIN, C. P., SCHUMAN, J. S., STINSON, W. G., CHANG, W., HEE, M. R., FLOTTE, T., GREGORY, K., PULIAFITO, C. A., and FUJIMOTO, J. G., “Optical coherence tomography,” *Science*, vol. 254, pp. 1178–1181, 1991.
- [8] DEPEURSINGE, C. *La Tomographie*, pp. 163–218, 2002.
- [9] BORN, M. and WOLF, E., *Principles of Optics*. Cambridge University Press, 1999.
- [10] FERCHER, A. F., DREXLER, W., HITZENBERGER, C. K., and LASSER, T., “Optical coherence tomography-principles and applications,” *Rep. Prog. Phys.*, vol. 66, pp. 239–303, 2003.
- [11] YURA, H. T. *Opt. Acta*, vol. 26, p. 627, 1969.
- [12] SCHMITT, J. M. and KNUTTEL, A. *Journ. Opt. Soc. Am. A*, vol. 14, p. 1231, 1997.
- [13] THRANE, L., YURA, H. T., and ANDERSON, P. E. *Journ. Opt. Soc. Am. A*, vol. 17, p. 484, 2000.
- [14] KRAVTSOV, Y. A., “Propagation of electromagnetic waves through a turbulent atmosphere,” *Rep. Prog. Phys.*, pp. 39–112, 1992.
- [15] MACASKILL, C. *Proc. R. Soc. A*, vol. 386, p. 137, 1983.

- [16] MACASKILL, C. *Proc. R. soc. A*, vol. 386, p. 461.
- [17] FRANKENTHAL, S., WHITMAN, A. M., and BERAN, M. J. *Journ. Opt. Soc. Am. A*, vol. 1, p. 585, 1984.
- [18] WHITMAN, A. M. and BEARN, M. J. *Journ. Opt. Soc. Am. A*, vol. 2, p. 2133, 1985.
- [19] WHITMAN, A. M. and BERAN, M. J. *Journ. Opt. Soc. Am. A*, vol. 5, p. 735, 1988.
- [20] MAZAR, R. and FELSEN, L. B. *Opt. Lett.*, vol. 12, p. 146, 1987.
- [21] MAZAR, R. and FELSEN, L. B. *Journ. Acoust. Soc. Am.*, vol. 81, p. 925.
- [22] MAZAR, R. and FELSEN, L. B. *Journ. Acoust. Soc. Am.*, vol. 82, p. 593, 1987.
- [23] BAYES, T., "An essay towards solving a problem in the doctrine of chances," *Phil. Trans*, vol. 53, pp. 370–418, 1764.
- [24] LEGENDRE, A. M., "Nouvelles of methodes pour la determination ces orbites des cometes," 1806.
- [25] GAUSS, K. F., *Theory of motion of the heavenly bodies moving about the sun in conic sections*.
New York: Dover, 1963.
- [26] FISHER, R. A., "Theory of statistical estimation," *Proc. Cambridge Philos. soc.*, vol. 22, p. 700, 1925.
- [27] NEYMAN, J. and PEARSON, E. S., "On the problem of the most efficient tests of statistical hypotheses," *Phil. Trans. Roy. Soc. London, A*, vol. 231, p. 289, 1933.
- [28] KOLMOGOROFF, A., "Interpolation and extrapolation of stationary random series," *Bulletin Acad. Sci. USSR, Ser. Math.*, vol. 5, 1941.
- [29] WIENER, N., *Extrapolation, Interpolation, and smoothing of stationary time series*.
Tech. Press of M.I.T. and Wiley, New York, 1949.
- [30] GREEN, D. M. and M., S. J., *Signal detection theory and psychophysics*.
New York: John Wiley and Sons Inc., 1966.
- [31] ZWEIG, M. H., C. G., "Receiver-operating characteristic (ROC) plots: a fundamental evaluation tool in clinical medicine," *Clinical chemistry*, vol. 39, p. 561, 2003.
- [32] PEPE, M. S., *The statistical evaluation of medical tests for classification and prediction*.
New York: Oxford, 2003.

- [33] OBUCHOWSKI, N. A., "Receiver operating characteristic curves and their use in radiology," *Radiology*, vol. 229, p. 3, 2003.
- [34] SPACKMAN, K. A., "Signal detection theory: Valuable tools for evaluating inductive learning," in *Proceedings of the Sixth International Workshop on Machine Learning*, p. 160, San Mateo, CA: Morgan Kaufman, 1989.
- [35] EGAN, J. P., *Signal detection theory and ROC analysis, Series in Cognition and Perception*.
Academic Press, New York, 1975.
- [36] SWETS, J. A., DAWES, R. M., and MONAHAN, J., "Better decisions through science," *Scientific American*, vol. 283, p. 82, 2000.
- [37] BARRETT, H. H., MYERS, K. J., and WAGNER, R. F., "Beyond signal-detection theory," *SPIE*, vol. 626, p. 231, 1986.
- [38] BRADLEY, A., "The use of the area under the ROC curve in the evaluation of machine learning algorithms," *Pattern Recogn.*, vol. 30, p. 1145, 1997.
- [39] HANLEY, J. A. and MCNEIL, B. J., "The meaning and use of the area under a receiver operating characteristic (ROC) curve," *Radiology*, vol. 143, p. 29, 1982.
- [40] MANDEL, L., W. E., *Optical coherence and quantum optics*.
New York: Cambridge, 1995.
- [41] EINSTEIN, A. *Ann. Phys.*, vol. 33, p. 1275, 1910.
English translation in Colloid Chemistry, Alexander, J. (ed.), Vol. I, 323-339, Reinhold, New York (1926).
- [42] MANNING, R. M., *Stochastic Electromagnetic Image Propagation and Adaptive Compensation*.
McGraw-Hill, Inc, 1993.
- [43] NIETO-VESPERINAS, M., *Scattering and Diffraction in Physical Optics*.
Wiley, 1991.
- [44] RYTOV, S. M., "Diffraction of light on ultrasonic waves," *Izv. Akad. Nauk SSSR Ser. Fizika*, vol. 2, p. 223259, 1937.
- [45] TATARSKII, V. I., *Wave propagation in random media*.
Heidelberg: Springer Berlin, 1983.
- [46] CHERNOV, L. A., "Method of parabolic equation in the theory of wave propagation in a random medium," *Third Soviet Symp. on diffraction of Waves, Tbilisi, Izd. Manuka*, 1964.
- [47] SOBCHYK, K., *Stochastic wave propagation*.
New York: Elsevier Science Publishing CO., INC, 1984.

- [48] VISHIK, M. I. and FURSIKOV, A. V., *Mathematical problems of statistical hydrodynamics*.
Izd. Nauka, Moscow, 1980.
- [49] DEMANIN, A. N. and KOROLUK, W. S., *Characteristic functionals of a random wave field in inhomogeneous media, in Phys.-Techn. appl. of Boundary Problems*,
Naukova Dumka, Kiev, 1978.
- [50] KOTULSKI, Z. and SOBCZYK, K., "Characteristic functionals of randomly excited physical systems," *Physica A*, vol. 123, p. 261, 1984.
- [51] ISHIMARU, A., *Wave Propagation and Scattering in Random Media*.
IEEE Press, 1997.
- [52] RAYLEIGH, L. *Phil. Mag.*, vol. 41, p. 274, 1871.
- [53] MIE, G. *Ann. Phys.*, vol. 25, p. 377, 1908.
- [54] DEBYE, P. *Ann. Phys.*, vol. 30, p. 755, 1909.
- [55] DYER, S. D., DENNIS, T., STREET, L. K., and ETZEL, S. M., "Spectroscopic phase-dispersion optical coherence tomography measurements of scattering phantoms," *Optics Express*, vol. 14, p. 8138, 2006.
- [56] PUSEY, P. N., "Statistical properties of scattered radiation," in *Photon Correlation Spectroscopy and Velocimetry, NATO ASI Series B: Physics, Vol. 23*, pp. 45–141, New York: Plenum Press, 1977.
- [57] CHANDRASEKHAR, S., *Radiative Transfer*.
London, New York: Oxford Univ. Press, 1960.
- [58] SHUSTER, A., "Radiation through a foggy atmosphere," *The Astrophys. Journal*, vol. 21, p. 1, 1905.
- [59] KOHLER, W. and PAPANICOLAU, G. C., "Power statistics for wave propagation in one dimension and comparison with radiative transport theory," *J. Math. Phys.*, vol. 14, p. 1733, 1973.
- [60] KOHLER, W. and PAPANICOLAU, G. C., "Power statistics for wave propagation in one dimension and comparison with radiative transport theory, II," *J. Math. Phys.*, vol. 15, p. 2186, 1974.
- [61] DIENER, G., "A derivation of the radiation transfer theory for random media," *Physica A*, vol. 106, p. 398, 1981.
- [62] VINOGRADOV, A. G. and KRAVTSOV, Y. A. *Radiophys. Quantum Electron.*, vol. 16, p. 1055, 1973.
- [63] FERCHER, A. F. in *Ophthalmic Interferometry Optics in Medicine, Biology and Environmental Research* (BALLY, G. and KHANNA, S., eds.), (Amsterdam), p. 221, Elsevier, 1990.

- [64] MASTERS, B. R. in *Selected Papers on Optical Low-Coherence Reflectometry and Tomography SPIE Milestone Series Vol. MS165*, (Bellingham), SPIE, 2001.
- [65] MURALI, S., LEE, K. S., and ROLLAND, J., “Invariant resolution dynamic focus OCM based on liquid crystal lens,” *Optics Express*, vol. 24, p. 15854, 2007.
- [66] MURALI, S., LEE, K. S., and ROLLAND, J. P., “Dynamic Focusing Imaging Probe for Optical Coherence Microscopy,” *Proceedings of 20th Annual Lasers and Electro Optics Society Meeting (LEOS)*, 2007.
- [67] MURALI, S., LEE, K. S., and ROLLAND, J. P., “Invariant high resolution optical skin imaging,” *Proceedings of BIOS08 at Photonics West*, 2008.
- [68] WIENER, N. *Acta. Math.*, vol. 55, p. 117, 1930.
- [69] MANDEL, L. *Proc. Phys. Soc.*, vol. 74, p. 233, 1959.
- [70] MANDEL, L., W. E. *Proc. Phys. Soc.*, vol. 80, p. 894, 1962.
- [71] MEHTA, C. L. *Nuovo Cimento*, vol. 28, p. 401, 1963.
- [72] SALEH, B. E. A. and TEICH, M. C., *Fundamentals of Photonics*. Wiley, 1991.
- [73] D. MALACARA, I. RIZO, A. M., “Interferometry and the Doppler Effect,” *Appl. Opt.*, vol. 8, p. 1746, 1969.
- [74] HEE, M., “Optical Coherence Tomography: Theory,” in *Handbook of Optical Coherence Tomography* (BOUMA, B. E., T. G. J., ed.), (New York), Marcel Dekker, 2002.
- [75] AKCAY, A. C., LEE, K. S., FURENLID, L. R., COSTA, M. A., and ROLLAND, J. P., “Compact low-cost detection electronics for optical coherence imaging,” *Optical Engineering Letters*, vol. 45, pp. 070504:1–3, 2006.
- [76] KARIYA, R., MATHINE, D. L., and BARTON, J. K., “Analog CMOS circuit design and characterization for optical coherence tomography signal processing,” *IEEE Transactions on Biomedical Engineering*, vol. 51, p. 2160, 2004.
- [77] GASKILL, J. D., *Linear systems, Fourier transforms, and optics*. New York: Wiley, 1978.
- [78] CHEN, W. K., *The circuits and filters handbook*. Boca Raton: CRC Press : IEEE Press, 1995.
- [79] SIROHI, R. S., *Speckle metrology*. New York: Marcel Dekker, 1993.
- [80] BRIERS, J. D. *Physiol. Meas.*, vol. 22, pp. R35–66, 2001.
- [81] GEORGE, N., CHRISTENSEN, C. R., BENNETT, J. S., and GUENTHER, B. D. *J. Opt. Soc. Am.*, vol. 66, pp. 1282–1290, 1976.

- [82] GOODMAN, J. W. *Proc. IEEE*, vol. 53, pp. 1688–700, 1965.
- [83] GOODMAN, J. W. *J. Opt. Soc. Am.*, vol. 66, pp. 1140–50, 1976.
- [84] TATARSKII, V. I., “Characteristic functional for one class of non-Gaussian random functions,” *Waves in Random Media*, vol. 5, p. 243, 1995.
- [85] SRINIVASAN, S. K., *Stochastic Point processes and Their Applications*. London: Griffin, 1973.
- [86] ROLLAND, J. P. and BARRETT, H. H., “Effect of random background inhomogeneity on observer detection performance,” *J. Opt. Soc. Am. A*, vol. 9, p. 649, 1992.
- [87] ROLLAND, J. P., OŠDANIEL, J., DELEMOS, T., AKCAY, A., LEE, K., CHEONG, K., CLARKSON, E., CHAKRABARTI, R., and FERRIS, R., “Task-based Optimization and Performance Assessment in Optical Coherence Imaging,” *J. Opt. Soc. Am. A*, vol. 22, 2005.
- [88] SPINELLI, L., TORRICELLI, A., PIFFERI, A., TARONI, P., DANESINI, G. M., and CUBEDDU, R., “Bulk optical properties and tissue components in the female breast from multiwavelength time-resolved optical mammography,” *Journal of Biomedical optics*, vol. 9, p. 1139, 2004.
- [89] GEMERT, M. J. C. V., JACQUES, S. L., STERENBORG, H. J. C. M., and STAR, W. M., “Skin Optics,” *IEEE Transaction of Biomedical Engineering*, vol. 36, p. 1146, 1989.
- [90] CHEONG, W. F., PRAHL, A. S., and WELCH, A. J., “A Review of the Optical Properties of Biological Tissues,” *IEEE Journal of Quantum Electronics*, vol. 26, p. 2166, 1990.
- [91] S. A. BOPPART, A. L. OLDENBURG, C. X. D. L. M., “Optical probes and techniques for molecular contrast enhancement in coherence imaging,” *Journal of Biomedical Optics*, vol. 10, p. 041208, 2005.
- [92] LIN, A. W. H., LEWINSKI, N. A., WEST, J. L., HALAS, N. J., and DREZEK, R. A., “Optically tunable nanoparticle contrast agents for early cancer detection: model-based analysis of gold nanoshells,” *Journal of Biomedical Optics*, vol. 10, pp. 064035–1, 2005.
- [93] SOKOLOV, K., FOLLEN, M., AARON, J., PAVLOVA, I., MALPICA, A., LOTAN, R., and KORTUM, R., “Real-time vital optical imaging of precancer using anti-epidermal growth factor receptor antibodies conjugated to gold nanoparticles,” *Cancer Res.*, vol. 63, pp. 1999–2004, 2003.
- [94] GAROFALAKIS, A., ZACHARAKIS, G., FILIPPIDIS, G., SANIDAS, E., TSIFTSIS, D. D., STATHOPOULOS, E., KAFOUSI, M., RIPOLL, J., and PAPAZOGLU, T. G., “Optical characterization of thin female breast biopsies based on the reduced scattering coefficient,” *Phys. Med. Biol.*, vol. 50, p. 2583, 2005.

- [95] LEE, M., NAMMALVAR, V., GOBIN, A., BARTON, J., WEST, J., and DREZEK, R., "Nanoshells as contrast agents for scatter-based optical imaging," *3rd IEEE International Symposium on Biomedical Imaging: Nano to Macro*, p. 371, 2006.
- [96] SHEPPARD, C. J. R., "Fractal model of light scattering in biological tissue and cells," *Opt. Lett.*, vol. 32, p. 142, 2007.
- [97] XU, M. and ALFANO, R. R., "Fractal mechanisms of light scattering in biological tissue and cells," *Opt. Lett.*, vol. 30, p. 3051, 2005.
- [98] SHAPIRO, J. H., CAPRON, B. A., and HARNEY, R. C., "Imaging and target detection with a heterodyne-reception optical radar," *Appl. Opt.*, vol. 20, p. 3292, 1981.